Top-Down and Bottom-Up Strategies to Prepare Nanogap Sensors

for Controlling and Characterizing Single Biomolecules

by

Joshua Sadar

A Dissertation Presented in Partial Fulfillment
of the Requirements for the Degree
Doctor of Philosophy

Approved July 2019 by the
Graduate Supervisory Committee:

Quan Qing, Chair
Stuart Lindsay
Sara Vaiana
Robert Ros

ARIZONA STATE UNIVERSITY

August 2019

ABSTRACT

My research centers on the design and fabrication of biomolecule-sensing devices that combine top-down and bottom-up fabrication processes and leverage the unique advantages of each approach. This allows for the scalable creation of devices with critical dimensions and surface properties that are tailored to target molecules at the nanoscale.

My first project focuses on a new strategy for preparing solid-state nanopore sensors for DNA sequencing. Challenges for existing nanopore approaches include specificity of detection, controllability of translocation, and scalability of fabrication. In a new solid-state pore architecture, top-down fabrication of an initial electrode gap embedded in a sealed nanochannel is followed by feedback-controlled electrochemical deposition of metal to shrink the gap and define the nanopore size. The resulting structure allows for the use of an electric field to control the motion of DNA through the pore and the direct detection of a tunnel current through a DNA molecule.

My second project focuses on top-down fabrication strategies for a fixed nanogap device to explore the electronic conductance of proteins. Here, a metal-insulator-metal junction can be fabricated with top-down fabrication techniques, and the subsequent electrode surfaces can be chemically modified with molecules that bind strongly to a target protein. When proteins bind to molecules on either side of the dielectric gap, a molecular junction is formed with observed conductances on the order of nanosiemens. These devices can be used in applications such as DNA sequencing or to gain insight into fundamental questions such as the mechanism of electron transport in proteins.

i

DEDICATION

I would like to thank my family at large for their support and encouragement over the last six years. In particular, I would like to thank my parents for letting us stay with them while we got on our feet and for their considerable childcare efforts. I would also like to thank my parents-in-law for demonstrating that earning a physics PhD is not incompatible with having a large family!

To Hannah: Thank you for your unflagging support and for convincing me to do this in the first place. Thank you especially for putting in the extra hours taking care of the kids while I was finishing my dissertation writing. I could not have done it without you!

To Isaiah, Jenny, Keziah, Mariam, Sarah, and Anastasia: Thank you for being great kids, and for putting up with frequent long hours. I love you all!

It is the glory of God to conceal a matter,

But the glory of kings is to search out a matter.

Proverbs 25:2

ACKNOWLEDGEMENTS

TABLE OF CONTENTS

LIST OF TABLES

LIST OF FIGURES

1. INTRODUCTION

There is increasing interest in biomolecular devices, particularly at the single-molecule level. Top-down fabrication techniques, developed over decades in the semiconductor industry, are powerful tools for constructing electronic devices at sub-micron scales. Top-down fabrication is frequently defined as a subtractive process, where materials are removed from a substrate in order to produce features of a defined size, shape and location[1-4]. Representative top-down fabrication techniques are photolithography, physical vapor deposition, and wet or dry chemical etching. At the present time however, top-down techniques are less well suited for delivering the critical physical and chemical properties – often involving nanometer- or even Angstrom-level precision – needed to directly interface with single biomolecules. To fill the gap – both figuratively and literally – techniques such as electrochemical deposition and chemical surface modification can be applied to initial structures created by top-down methods. These techniques belong to a larger class known as bottom-up fabrication, where atomic or molecular components are built using chemical synthesis, growth, or self-assembly techniques[1-4]. The combination of top-down and bottom-up fabrication techniques offers a powerful paradigm for the design and construction of new biomolecular sensors In this thesis, I focus on device structures that can be used for DNA sequencing and protein sensing.

A promising candidate for a third-generation DNA sequencer is the nanopore. In a nanopore sensor, the passage of DNA through a nanoscale aperture generates a time-dependent signal that can contain information about local structure, including base

sequence. Nanopore sequencing has the potential for rapid speed, single-base sensitivity, and long read lengths. Considerable work has been done developing nanopore sequencing platforms. To date, the most successful approach has been to use protein pores embedded in lipid membranes, an approach which has produced a commercial nanopore sequencing chip[24]. Nevertheless, limitations intrinsic to biological pores have kept interest strong in developing solid-state pores in inorganic membranes. Overall the major challenges faced by existing fabrication techniques (both biological and solid-state) are specificity of detection, controllability of translocation, reproducibility of fabrication, and scalability of fabrication. A novel approach to fabricating solid-state nanopores is here introduced, based on the initial top-down fabrication of a nanoscale electrode gap embedded in a confined nanofluidic channel. Electrochemical deposition can be used to reversibly tune the dimension of the gap, with final pore dimensions controlled by an impedance-based feedback system. This strategy has the advantage of self-aligning the pore with a pair of electrodes which can generate electric fields that can be used to control the translocation of molecules through the pore.

While DNA contains a vast wealth of biological information, that information is put into practice by a vast array of proteins, molecular machines that carry out life's functions at the sub-cellular level. In recent years, an increasing amount of research has shown that proteins are surprisingly good conductors of electricity. There exist models, primarily based on electron tunneling or hopping, which can partially explain electronic conductance through proteins, but experimental evidence has shown rates of electron transport several orders of magnitude higher than that predicted by theory. Of particular interest, very recent results show the critical role that contacts between metal electrodes

2

and proteins play in measured levels of conductance. Additionally, these results suggest that the conductance of a protein can vary based on its conformation. This would allow for a new way to track protein dynamics. These new results have been achieved primarily using a scanning tunneling microscope (STM), but the adaptation of the experimental approach to a chip-based platform would be able to leverage advantages of scalability and reproducibility. A new architecture of chip design has been proposed that combines the fabrication of precisely-spaced metal-insulator-metal junctions with the chemical modification of electrode surfaces to specifically bind to target proteins. These chips provide a platform for basic research into the fundamental nature of electrical conductance in proteins, as well as the opportunity to apply this knowledge to efforts such as the sequencing of DNA by measuring conductance fluctuations in DNA polymerase.

In this dissertation, Chapter 2 is a literature review of efforts to use nanopore structures in DNA sequencing. Section 2.1 gives a brief historical background to DNA sequencing in general. Section 2.2 provides an outline for understanding nanopore sequencers. The basic architecture of a nanopore structure is discussed, and elementary theory about nanopore measurements is introduced. Finally, a set of criteria for a viable nanopore sensor is introduced as a framework for evaluating the various strategies that have been explored to date. Section 2.3 is dedicated to reviewing efforts to create nanopore sequencers using protein pores embedded in lipid membranes. Major achievements are highlighted, and the field is assessed relative to the criteria introduced in Section 2.1. Section 2.4 is organized in the same fashion as Section 2.3, but its focus is on the development of nanopore structures fabricated from inorganic materials – so-

called solid-state nanopores. Finally, Section 2.5 gives a brief summary of the chapter

and prospects for continued development of nanopore sensors.

Chapter 3 focuses on a new approach to fabricating solid-state nanopores – a

nanofluidic system in which the critical pore dimensions are defined by electrochemical

deposition of metal onto a pair of microelectrodes fabricated by top-down methods.

Section 3.1 places this project in the context of the previous research and describes the

design of the devices in light of the criteria identified in Chapter 2. Section 3.2 is

devoted to the electrochemical deposition process and the feedback controls for tuning

the final gap size. Section 3.3 describes the fabrication process of a representative

device. In Section 3.4, I show data characterizing various aspects of the device at

different stages of the fabrication process. Section 3.5 includes results and analysis of

initial experiments. Section 3.6 is an evaluation of the current state of the project with a

roadmap for completing the development of the platform. In Section 3.7, I look ahead at

some of the areas where this kind of device could produce exciting results and

capabilities in the future. Part of this chapter, particularly in Section 3.2, was previously

published as "Confined Electrochemical Deposition in Sub-15 nm Space for Preparing

Nanogap Electrodes" in ECS Transactions (Sadar et al., 2017)[59] (see appendix for co-

authors' agreement on using published work). Parts of this chapter were also used as

supporting material for US Patent Application 0118090.192-US1 and for a manuscript in

preparation.

Chapter 4 is devoted to an architecture for creating single-protein electronic

junctions combining top-down fabrication of metal-insulator-metal stacks with surface

modification of electrodes that form highly-specific bonds to target proteins. Section 4.1

introduces the topic of electronic conduction by proteins and gives a brief review of relevant literature. Section 4.2 describes the requirements for an effective protein junction chip and highlights key design features of the device. Section 4.3 describes the top-down portion of the fabrication process of a representative chip and also discusses situations where materials or processes were changed to improve device yield. Section 4.4 shows the results of preliminary experiments characterizing the device and fabrication processes. In Section 4.5, results of initial experiments with proteins are presented and discussed. Proteins tested include the phi29 DNA polymerase and IgE anti-DNP antibody. Section 4.6 evaluates progress on this project and offers suggestions for improving identified areas of weakness. Section 4.7 concludes with a look at the future applications of such protein devices once the platform is mature. Parts of this chapter are being used for a manuscript in preparation.

Chapter 5 is an overall conclusion summing up the projects and how the lessons learned in each can be applied to the other.

2. NANOPORE SEQUENCING

2.1 Background

The ability to rapidly and efficiently decode DNA sequences holds great potential for fundamental research and biomedical applications. First- and second-generation sequencing methods are capable of sequencing DNA with high accuracy and have seen significant advances in the last ten years. Even so, there are limitations to current approaches, and there remains an opening for third-generation sequencing techniques that can offer long read lengths with a single-molecule, label-free approach. One such method is nanopore sequencing, in which a DNA molecule passing through a membrane via a nanoscale aperture generates fluctuations in an ion current measured between two chambers. Nanopore sensors can be made either with biologically-derived protein pores or via solid-state fabrication processes. In this review, I will take a look at the history of nanopore sequencing efforts. Starting with protein pores and then proceeding to solid-state pores, I will review the key developments in the field and track the contributions of the most prominent research groups. Special attention will be paid to efforts to address three key challenges in nanopore sequencing: detection specificity, translocation control, and fabrication scalability and reproducibility. For the two primary divisions of the field, I will assess how well the current state of the art has met these challenges and evaluate future prospects. Lastly, I will give a brief introduction to my own research, situating it in the context of the field.

2.1.1 DNA sequencing – a very brief history

It is difficult to overstate the role that DNA plays in biology. From a physical standpoint, DNA is a polymer made of repeating units called nucleotides. Each nucleotide consists of a deoxyribose sugar, a phosphate group, and one of four nitrogen-containing bases – guanine, adenine, thymine, and cytosine. In living cells, DNA exists for most of the time as a double-stranded molecule made of two chains of nucleotides connected with hydrogen bonds. From an informational standpoint, DNA is a data repository. First and foremost, DNA contains the information required for synthesizing the proteins which are the engines of life at the molecular scale. In a process known as transcription, the sequence of bases in a section of DNA is copied to form an RNA molecule – a close molecular cousin substituting ribose for deoxyribose and uracil for thymine. RNA then undergoes translation. A molecular machine called a ribosome reads the RNA bases in groups of three called codons, each of which corresponds to an amino acid. As each codon is read, the ribosome attaches the appropriate amino acid onto a growing chain which will, when finished, become a functioning protein. Understanding the structure and function of proteins is key to understanding life at the molecular level, and each protein's structure and function is ultimately determined (to varying degrees of precision) by its sequence. Understanding DNA sequences can give us critical information about diseases, help us to engineer better crops, and yield insights about the nature of life itself.

Since humans first became aware of the vast treasures locked away by the genetic code, we have poured immense resources into developing the keys needed to read it. While a full treatment of chemical sequencing methods is vastly beyond the scope of this review, there are a few important methods that bear some brief description. One of these,

the first widely-used method for sequencing DNA, is known as chain-termination sequencing[5]. Also known as Sanger sequencing after its inventor, Frederick Sanger, it relies on modified nucleotides that stop a DNA synthesis reaction. The reaction is separated into four parts. Each portion contains copies of the DNA to be sequenced, a DNA primer, a DNA polymerase, a full complement of all four deoxynucleotides, and a set of special dideoxynucleotides corresponding to one of the four bases. A dideoxynucleotide can be incorporated into the newly synthesized DNA, but it prevents any further nucleotides from being added afterward. As long as the concentration of dideoxynucleotides is sufficiently low, there should be a fragment terminated at every position in the template. After the reactions are finished, gel electrophoresis can be used to separate the fragments by length. By matching up the fragment lengths with the identity of the terminator base, the sequence can be determined. Because of the difficulty in resolving single-base length differences as overall fragment length increases, chain termination reads are limited to less than one kilobase (kbp) in length. In order to sequence longer structures such as whole genomes, which can be on the order of Gbp, shorter fragments must be sequenced and then assembled together. This genome assembly is not always straightforward, especially in highly-repetitive areas of a genome. Despite these limitations, the Sanger method was the primary DNA sequencing method used from the 1980s through the mid-2000s and was used to produce the first human genome in 2001 at a cost of $100 million.

In the last decade, there has been a wave of second-generation sequencing methods, many based on the principle of sequencing by synthesis[6]. In this approach, the fragment to be sequenced is amplified, then undergoes a series of synthesis reactions

using deoxynucleotides modified with fluorescent reversible terminator. After each incorporation step, the terminator is stripped and fluoresces at a certain wavelength determined by the identity of the base, and the next dNTP is ready to be incorporated. By examining the sequence of fluorescence signals, once can read the sequence of the nucleotides. Sequencing by synthesis, like other second-generation techniques, is subject to similar restrictions on read length as chain termination sequencing, but it has one major advantage. While costs for chain termination sequencing dropped by a factor of ten within about five years after the initial human genome completion, the technique was still prohibitively expensive for large-scale use. In the last decade-plus, however, second-generation techniques have reduced sequencing costs by another four orders of magnitude such that a human genome can now be completed at a cost of only $1000.

2.1.2   *Toward third-generation sequencing*

Despite the great advances made, there remain opportunities for a third generation of DNA sequencing technologies. Techniques which can offer long read lengths, are label-free, and can work with single molecules rather than clonal colonies are particularly attractive. Increases in read length would greatly simplify the task of genome assembly. Single-molecule and label-free techniques would reduce the reliance on access to chemistry labs for the required preparations. In theory, they would allow for a portable sequencer that could be used for on-site sequencing immediately after sample extraction.

Nanopore sensors are one such candidate for third-generation sequencing. In such a device, the dimension of the pore matches precisely with the target molecule, so that the presence and/or motion of the molecule inside the sensor can generate measurable time-dependent electrical read-out signals containing significant local structural information.

9

This framework can be applied to a wide variety of biomolecules, but DNA sequencing has attracted the greatest amount of interest. Nanopore sequencing has the potential for rapid speed, single-base sensitivity, and long read lengths. The capability of single-molecule level and label-free detection and characterization of DNA and other biomolecules promises a new paradigm in both fundamental studies and biomedical applications. Indeed, devices based on protein nanopores have already begun to show promising results. Difficulties in integrating protein pore devices with additional electronics, however, have led to significant investment into the development of solid-state nanopore devices. However, existing techniques for fabricating solid-state nanopores face great challenges such as the scalability and reproducibility of fabrication, translocation control, and specificity in read-out signals.

In this review, I will examine the history of nanopore sequencing effort. I will look at the contributions of some of the most accomplished research groups, summarize important results, and examine efforts to solve particular challenges. I will also assess the progress of the field as a whole toward the goal of developing a viable third-generation sequencing technology.

2.2   Nanopore Basics

2.2.1   Basic Nanopore Architecture

Before looking at the specific details of each process, it is instructive to take a larger look at the basic architecture of a nanopore sequencing device. At its most basic level, a nanopore device consists of two chambers separated by a membrane in which there is a nanoscale opening. Each chamber is filled with an electrolyte solution, and one

chamber (hereafter known as the *cis* chamber; the other is termed the *trans* chamber) also

contains the DNA to be analyzed. In the most common experimental method, a potential

bias is established between the two chambers such that anions are driven through the pore

from *cis* to *trans*, while cations cross from *trans* to *cis*. The coordinated motion of ions

produces a current that can be measured between the two chambers. DNA, being

negatively charged, is also driven toward the pore. If the pore is narrow enough

(approximately the width of a DNA molecule), the DNA will be forced to uncoil and

traverse the pore single file.

It is instructive to consider the current that is passing through the pore at any

given moment. In the absence of a DNA molecule, the current through a cylindrical pore

of length l and diameter d can be approximated by the following equation:

$$i_{open} \approx (\mu_C + \mu_A) n_{CA} e \left(\frac{4l}{\pi d^2} + \frac{1}{d} \right)^{-1} V_{bias}$$

where μ_C and μ_A are the mobilities of the cation and anion, respectively, n_{CA} is the ion

concentration, e is the elementary charge, and V_{bias} is the potential applied across the

membrane. When a DNA molecule enters the pore, there is a significant change. For

typical electrolyte concentrations (100 mM KCl is a common solution to use in DNA

translocation experiments), the DNA has about 10 times higher charge density than the

surrounding solution [give in elementary charges per nm3] but transits the pore about

1000 times more slowly due to its larger size. In effect, the analyte can be considered as

uncharged, and its presence reduces the effective pore area available for charge transport. The above equation is then altered, like so:

$$i_{occupied} \approx i_{open} \left(1 - \frac{A_{occupied}}{A_{open}} \right)$$

For large values of A_{open}, the overall current is little changed, but when A_{open} is only slightly larger than $A_{occupied}$, the magnitude of the current will drop significantly when DNA is in the pore. Observed over time, this process results in an ionic current in which an open pore value is interrupted by downward spikes as DNA molecules pass through the pore. Furthermore, it has been shown that in the case of DNA, the size of the downward spike (or "resistive pulse", as it is known) is related to the identity of the base passing through the pore.

2.2.2 Criteria for viable nanopore sequencers

In order to produce an effective nanopore sequencing device, three criteria must be met: specificity of detection, translocation control, and fabrication scalability and reproducibility.

First, an effective nanopore sequencer must be able to identify single bases with a high level of accuracy. The intrinsic spatial resolution of a nanopore is determined by the number of nucleotides that contribute to the ion current at any given time. There are two primary geometrical factors that affect this value. The first, and most obvious, is the length of the pore. Any nucleotide which is present in the pore will be contributing to the ion current. This leads to the natural conclusion that thinner pores will give higher spatial

resolution than thicker pores. Work on graphene membranes, which will be discussed later, suggests that it may be possible to engineer atomically-thin pore structures. To obtain single-base resolution, however, it is not sufficient to have a pore thin enough ($\leq$ 3.3 Å) to admit only one nucleotide at a time. The width of the pore also makes a critical contribution. This contribution has two aspects. First, the width of the pore determines the area available for ion transport. The larger the pore, the larger the residual current during DNA translocation. As we have discussed, the ion current is determined by the distribution of the electric field, and significant field strength extends outside the pore to a distance roughly equivalent to the width of the pore. Since the width of the pore is constrained by the width of a ssDNA molecule (~1 nm), several times the length of a nucleotide, it is impossible to get single-base precision with an ion-current readout. In order to achieve the required measurement specificity, therefore, one of two advances need to be made: the development of a new readout mechanism which is capable of single-base resolution, or the implementation of strategies to deconvolute signals with contributions from multiple bases in such a way that the sequence is preserved.

There are two respects in which the ability to control the motion of DNA through the pore is critical to the success of nanopore sequencing techniques. The first relates to the average speed of translocation. Under typical driving potentials (on the order of 100 mV), DNA will translocate at a rate of approximately 10^6 bp/s.[7] Based on the bandwidth of recording electronics, the translocation rate must be decreased to at most 10^3 bp/s in order to achieve single-base temporal resolution. The second consideration requires keeping the translocation rate constant. To give an accurate read, it must be possible to correctly identify repeated bases. This is all the more important considering that there are

only four bases, so repeats are very common. Without taking special measures, though, DNA moves stochastically, resulting in a wide spread of single-nucleotide translocation times.

Lastly, device production needs to be reproducible and scalable. In order to produce reliable and reproducible signals, one must be able to reproducibly fabricate devices with consistent dimensions and surface chemistry. Additionally, fabrication techniques must be efficient enough for device cost to be competitive with existing technologies.

2.3   Protein Nanopores

2.3.1   Introduction

Research on nanopores for DNA sequencing has proceeded along two primary branches characterized by the type of nanopore being used. One avenue has used protein pores extracted from bacteria, while the other uses solid-state pores that are constructed using a variety of semiconductor fabrication techniques. Each approach has its own characteristic strengths and weaknesses, which makes it instructive to consider them separately. In this review, we will consider the basic structure of each type of nanopore sensor and give a brief history of the major advances for that technique. We will examine the current state of the art, evaluating how well the technique has met the essential challenges of effective nanopore sequencing and what areas still need to be improved.

2.3.2   Deamer and Branton – Protein Pore Foundations

The first demonstration of DNA translocating through a protein nanopore was achieved by a team led by David Deamer and Daniel Branton in 1996[7]. They used an α-hemolysin pore from the bacterium *Staphylococcus aureus*, which is a heptameric protein that self-assembles in a lipid bilayer to form a pore with a 2.6-nm diameter. This pore is large enough to admit single-stranded DNA or RNA, but sufficiently small to exclude double-stranded polynucleotides. The group showed that the translocation of polynucleotides through the nanopores produced a blockade current event whose duration was proportional to the length of the DNA or RNA molecule and inversely proportional to the driving voltage. This yields a baseline translocation time of about 1.5 μs/bp. This important proof of principle suggested the possibility of using nanopores to obtain polynucleotide sequences.

Peak	Lifetime (μs)	Blockades/sec
1	92	0.9
2	290	2.3
3	1288	1.5
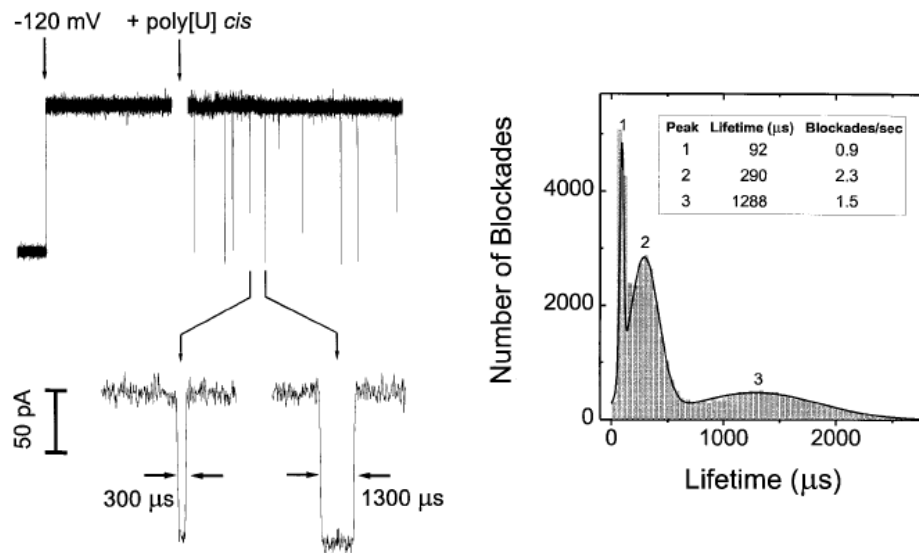
Figure 2.3.1. Translocation Data[7]. Left – This plot shows the features characteristic of ionic current readouts during translocation. A baseline current is interrupted by downward spikes indicating translocation of a single molecule. A close-up

15

of one of the downward spikes reveals a characteristic current blockade amplitude and dwell time. Right – a distribution of dwell times for 210-bp poly[U] shows three distinct populations of events.
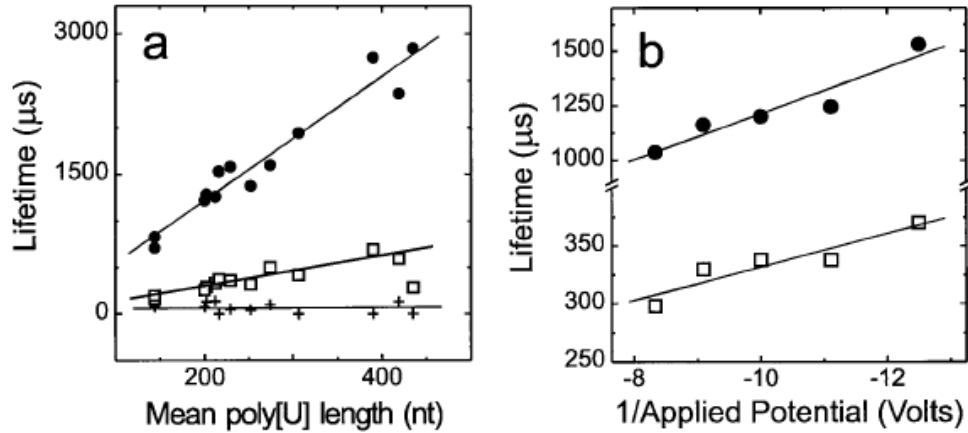
Figure 2.3.2. Translocation Statistics[7]. (a) Dwell times compared to molecule length at driving potential of -120 mV for the three populations of events identified in Figure 2.3.1. (b) Dwell times compared to inverse driving potential for event types 2 and 3 for 215-bp poly[U].

The next step was to show the ability of nanopore sensors to distinguish between different nucleotides. One of the first demonstrations of this capability was done by Branton's group at Harvard in 2000[8]. They showed differing translocation statistics in two situations. The first was discriminating between homopolymers constructed of different bases, comparing the translocation behavior of poly(dA)$_{100}$ and poly(dC)$_{100}$. The two molecules showed differences in average blockade current as well as average dwell time in the pore. The second situation examined involved distinguishing between molecules composed of the same bases in different sequence, namely poly(dA$_{50}$dC$_{50}$) and poly(dAdC)$_{50}$ in one test, and poly(dC$_{50}$dT$_{50}$) and poly(dCdT)$_{50}$ in another. Both experiments in the second set showed differences in the average blockade current and

dwell time values, though there was considerably more overlap than in the homopolymer case. Of particular note is that these experiments showed that more than one feature of the translocation current signal could be used to distinguish between nucleotides.
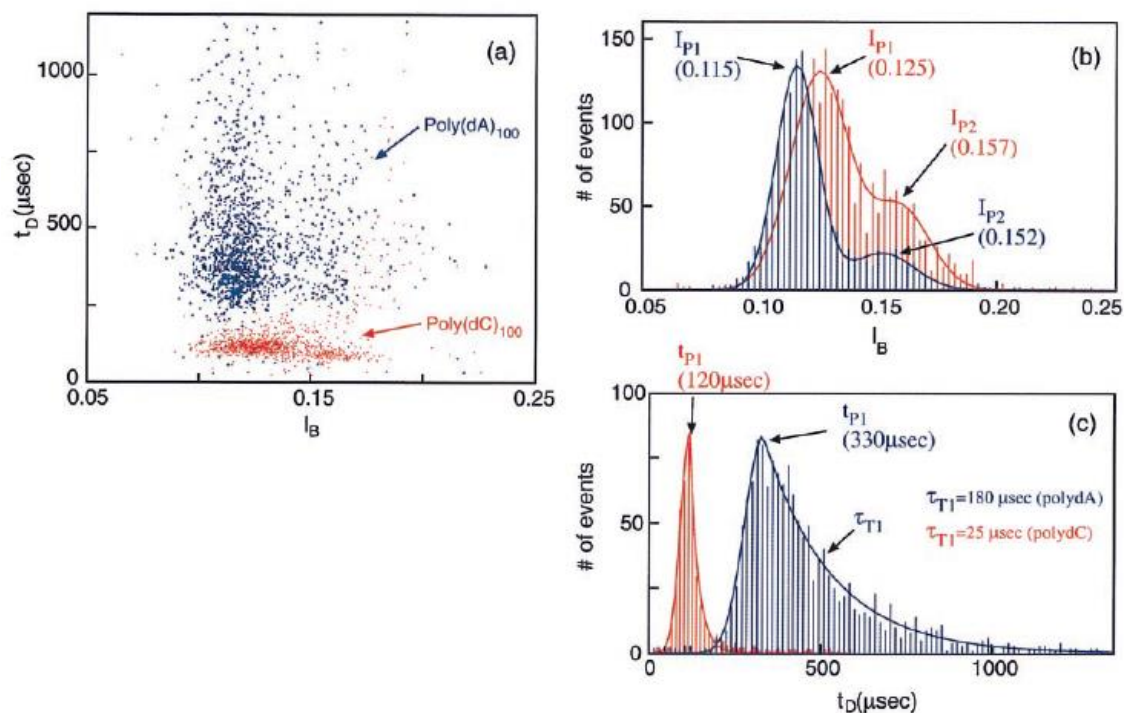
Figure 2.3.3. Distribution of Homopolymer Translocation Events[8]. (a) Scatter plot showing current blockade levels and dwell times for translocation of Poly(dA)$_{100}$ and Poly(dC)$_{100}$ molecules. (b) Histogram of events from (a) arranged by blockade current I_B. (c) Histogram of events from (a) arranged by dwell time t_D.
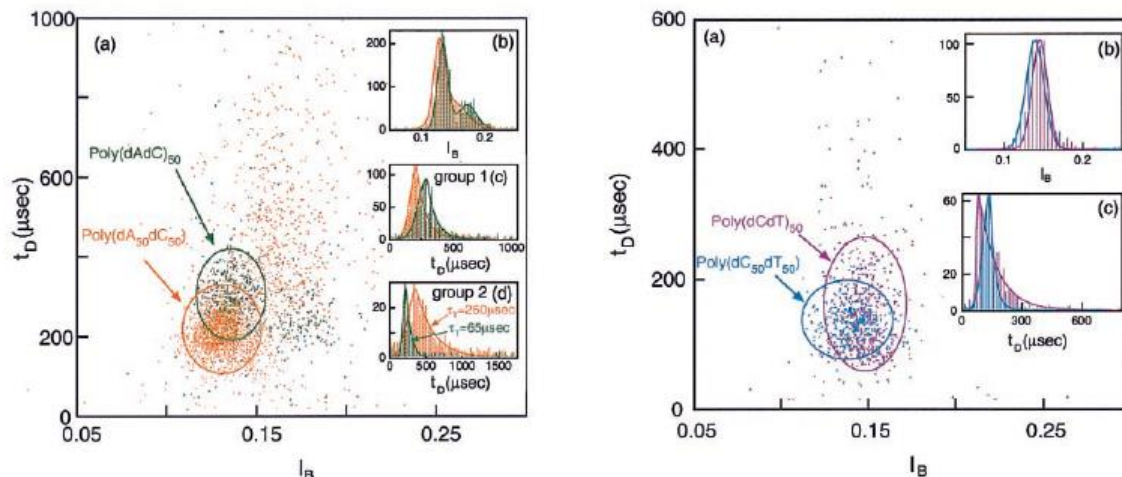
Figure 2.3.4. Distribution of Heteropolymer Translocation Events[8]. Left – Comparison of translocation events for Poly(dAdC)$_{50}$ and Poly(dA)$_{50}$(dC)$_{50}$. Right – Comparison of translocation events for Poly(dCdT)$_{50}$ and Poly(dC)$_{50}$(dT)$_{50}$.

A follow-up study by the same group probed deeper into translocation dynamics in conditions of variable molecule length and driving potential[9]. While average translocation speed and current blockade level were constant for long molecules, significant departures were seen for molecules whose lengths were less than or equal to the length of the nanopore (roughly 5 nm). Additionally, translocation speed was found to depend nonlinearly on the driving voltage. These data were used to estimate the diffusion constant for short DNA molecules as well as the energy penalty for entering the pore.

This foundational research demonstrated the ability to translocate DNA and RNA molecules through protein pores and to distinguish between different nucleobases. It also gave baseline parameters for the behavior of translocation rates and blockade current

signals. The stage was set for serious attempts to pursue advances in spatial and temporal resolution in pursuit of single-base sequencing.

2.3.3   *Mark Akeson – Translocation Slowing*

Another early colleague of Deamer and Branton's, Mark Akeson, began focusing on translocation control by experimenting with enzymatic proteins that interacted with DNA. His most important work came with the development of the phi29 DNA polymerase, which was used to ratchet DNA through the pore at speeds reduced by as much as 10^5 compared to uncontrolled translocation.

One of the most important contributions toward controlling DNA translocation through protein nanopores came from the lab of Mark Akeson, a colleague of David Deamer at UC Santa Cruz. Akeson collaborated with Deamer and Daniel Branton on some of the earliest nanopore studies, identifying secondary structural effects on translocation signals[10] and analyzing hairpin structures with a support vector machine[11].

After this, Akeson began to investigate DNA-protein interactions using nanopores, and published a brief study looking at the how the addition of DNA-binding proteins affects translocation statistics[12]. Such proteins are much too large for translocation, and the addition of a protein such as streptavidin, which will bind strongly to biotinylated DNA, results in a complete blockage of the pore which must be cleared by reversing the driving potential. Exonuclease I, on the other hand, has a weak enough interaction that can be overcome by the driving force. Translocation statistics reveal two populations of events. One set is identical to translocations before adding the exonuclease I and represents unbound DNA. The other set has a slightly higher current blockade level and dwell times that are both longer and more broadly distributed. This

indicates that the binding force of the exonuclease was strong enough to significantly

slow the passage of DNA.
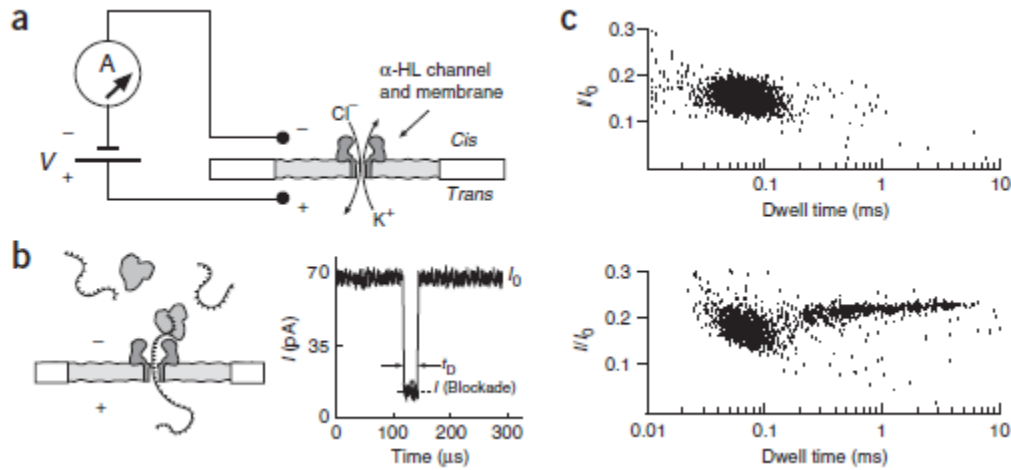
Figure 2.3.5. Translocation of DNA-Exonuclease Complexes[12]. (a) Schematic of measurement setup. (b) Capture and partial translocation of a DNA-exonuclease complex along with a current trace from a translocation event. (c) Current blockade level vs. dwell time for DNA alone (top) and DNA plus exonuclease I (bottom).

The results of this study were used to suggest a new high-throughput

measurement technique, coined "nanopore force spectroscopy" (NFS) for single-

molecule analysis. In addition, they contained the seeds of a powerful idea: using a

protein bound to DNA to control its motion through the pore.

This idea began to bear fruit with Akeson's work on phi29 DNA polymerase, an

enzyme that catalyzes DNA synthesis and binds very strongly to DNA[13,14]. In the

absence of Mg^{2+} ions, phi29 DNAP will bind to DNA but will not begin synthesis. In an

approach very similar to that described earlier for NFS, a bound DNA-phi29 complex is

drawn into a nanopore and blocks the current. Eventually, the binding force is overcome,

and the DNA begins passing through the pore. The difference is that in the case of phi29

DNAP, the translocation time is increased by a factor on the order of 10^4, enough to reach

single-base temporal resolution.
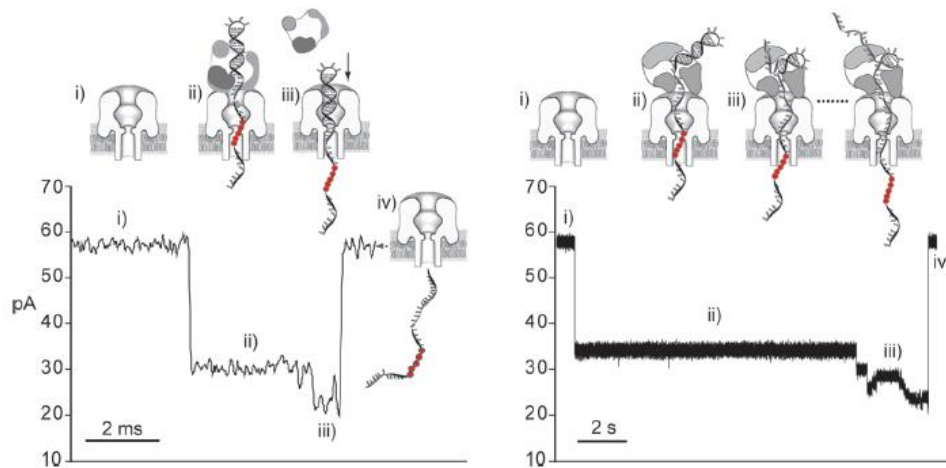
Figure 2.3.6. Translocation of DNA-Enzyme Complexes[13]. Left – Translocation of a KF(exo-)-DNA complex. Prior to the dissociation of KF(exo-), dwell time is increased by a factor of about 10 compared to native DNA translocation. Right – Translocation of a phi29 DNAP-DNA complex. Dwell time is increased by an additional factor of 1000 - 10,000 compared to KF(exo-).

This process was then further refined to allow for two reads of each base[14].

Rather than restricting the activity of the enzyme by Mg^{2+} starvation, a blocking oligomer

was added to prevent synthesis. In the new configuration, the template DNA pulls itself

through the DNAP as it translocates the pore. Eventually, the blocking oligomer is

stripped off, allowing the DNAP to begin synthesis. The processive force is great enough

to overcome the attractive force from the pore, and the DNA is drawn back through.

Because the DNAP's function is to synthesize DNA (and is not merely exerting a

continuous force on the molecule), the motion naturally occurs in single-base steps. This

means that the differential spatial resolution should be at the single-base level
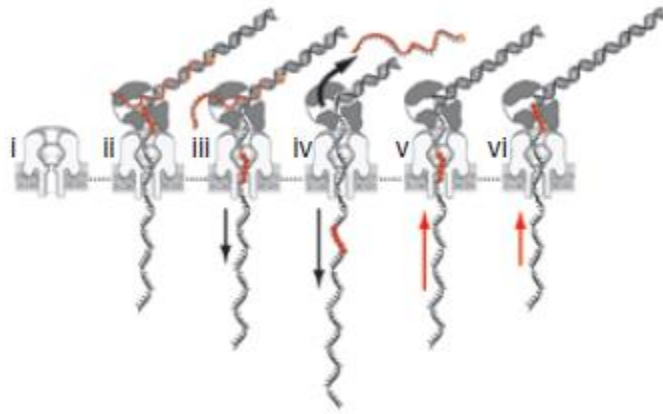
Figure 2.3.7. Bidirectional Ratcheting of DNA Through a Nanopore[14]. (i) Empty
pore. (ii) Capture of DNAP-DNA complex. (iii) Forward translocation of target strand.
(iv) Removal of blocking oligomer. (v) Initiation of synthesis and reverse translocation of
target strand. (vi) Termination of synthesis at abasic residues.

The development of phi29 DNAP as a ratcheting nanopore motor enabled slow

translocation in discrete (albeit stochastic) single-base steps. The time resolution

problem for protein nanopores was solved. Meeting the challenge of spatial resolution

would require additional innovations.

2.3.4   Gundlach and Niederweis – MspA Pores

Improving the spatial resolution of readout signals is an area where the protein

nanopore approach has seen significant success, but also a fundamental limitation.

Perhaps the greatest advantage of protein nanopores is that their geometry is atomically

precise, each pore of a given variety having exactly the same dimensions as every other

pore of that variety. As mentioned earlier, the first protein to be used in nanopore

sequencing was the heptameric α-hemolysin. The critical region of α-hemolysin is a barrel with a width of 26 Å and a length of 52 Å. While the width is reasonably well suited to the task of DNA sequencing, the barrel is much too long for single-base precision. The current signal generated at any given moment will have contributions from every base inside the barrel. With a distance between bases of 3.3 Å, this means that about 16 bases are in the barrel at any given time. If we include the electric field extension due to the pore width, the ionic current signal has contributions from about 25 bases, far too many to get usable sequence information.

Even before Mark Akeson's breakthrough with phi29 DNAP, a major advance was made on this front. A collaboration between the University of Washington and the University of Alabama at Birmingham led by Jens Gundlach and Michael Niederweis developed a nanopore device based on the *Mycobacterium smegmatis* porin A (MspA) structure[15]. MspA was a particularly attractive candidate because of its geometry. The critical region of MspA is a constriction of width 12 Å and length 6 Å, suggesting that an ionic current signal during DNA translocation would contain contributions from only about 5 bases. The main problem with MspA was that it contained negatively-charged amino acids around the constriction, preventing negatively-charged DNA from entering the pore. Gundlach's team was able to successfully engineer a mutant MspA with neutral residues at those sites in order to remove the restriction. They then successfully demonstrated the detection of single-molecule translocation events through the MspA channel.
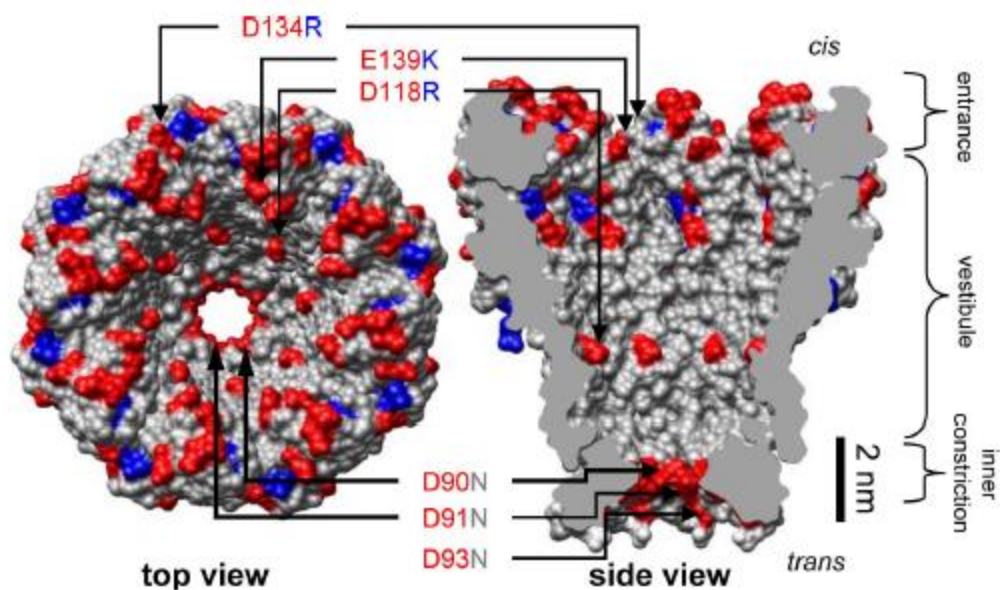
Figure 2.3.8. Structure of MspA[15]. Residues in red are negatively charged, while blue residues are positively charged. Labeled residues were altered by targeted mutation.

After the original development of MspA, the researchers were able to show the ability to distinguish between homopolymers and detect single-base substitutions under certain circumstances[16]. The real breakthrough, though, came when the MspA pore was combined with the phi29 DNAP[17]. With the temporal resolution offered by phi29 DNAP ratcheting and the spatial resolution inherent in the MspA pore, researchers were able to read sequence data with unprecedented accuracy. In particular, being able to map a known sequence to a current readout allowed an estimate of how many bases affected the ionic current signal at any time. A repeating 'CAT' sequence was employed with a substitution of G for T in a single location. A total of four nearby current levels were observed to change, with the greatest change happening at the substitution site.

Figure 2.3.9. Signal Readout from MspA/phi29 Nanopore[17]. (a) Signal trace from repeated 'CAT' sequence with single substitution. (b) Mean current levels from (a). Red shading shows deviation from expected levels, indicating influence of substituted base.

With this result, the goal of single-base nanopore sequencing was within reach. One last ingredient remained.

2.3.5 Hagan Bayley and Oxford Nanopore Technologies

While Deamer and Branton were the first to demonstrate the nanopore concept, Hagan Bayley also authored important early research, including structural studies of α-hemolysin. His work, like Akeson's began to focus on processive enzymes, including a novel but ultimately failed attempt to excise and feed nucleotides one by one into the nanopore. In 2007, he helped to found Oxford Nanopore Technologies, and it was ONT that provided the final ingredient for a viable nanopore sequencing device. Rather than push for higher intrinsic spatial resolution (which was already close to the theoretical limit), they developed an analytical method for deconvoluting the composite signal into its constituent parts. ONT's MinION sequencer was released in 2015, and despite early problems with its accuracy, it has seen continuous improvement and is starting to rival established techniques in composite accuracy (though not yet for single reads).

25

To understand the last step, it is often necessary to go back to the beginning. Shortly after the publishing of Deamer and Branton's first nanopore paper, a crystal structure of α-hemolysin was published[18]. Among the authors was one Hagan Bayley. It was Bayley, in fact, who provided the α-hemolysin for the foundational study. Soon after, Bayley began doing his own research on nanopore sequencing. From the beginning, Bayley used his expertise in protein mutation to engineer novel functions, such as creating a tether on the rim of the pore on which a dangling oligonucleotide can interact with a translocating target strand[19].

Convinced that nanopore sensing was a viable candidate for third-generation DNA sequencing, Bayley cofounded Oxford Nanopore Technologies in 2005 in order to actively develop nanopore-related technologies. In the meantime, he continued his public research. A particularly novel idea was to attach an exonuclease at the pore to sequentially cleave single bases, which would be fed into the nanopore[20]. Due to the small size of the analytes, a special adapter molecule was designed to fit inside the pore to interact with the nucleotide and generate a signal, and in this way the sequence would be inferred. While the original adapter molecule would too readily dissociate from the pore, additional research discovered a method of covalently attaching the adapter to the interior of the pore[21]. Significant gains were made, including achieving identification accuracies of 99.8%[22]. In the end, though, there were insurmountable difficulties involved in ensuring that all of the excised nucleotides were captured by the pore and that their order was correct.

Concurrently, Bayley (and likely Oxford Nanopore as well) was revisiting the question of signal processing. It was long known that an ion current readout would never

give true single-base spatial resolution. Some amount of deconvolution would have to be done. By 2009, Bayley was working on enhancing the effective resolution of a-hemolysin by identifying three "recognition sites" in the channel that were more sensitive than the straight barrel[23]. If the signal contributions from these sites could be isolated, then the relatively fixed lag between when a given base passed one site and then the next could be used to help determine the sequence. Even so, Bayley cautioned, "the ability to obtain a maximum of useful information will depend on finding a practicable way to slow the ssDNA down to such an extent that filtering of the signal can be used effectively to reduce noise levels."

Within a year, Akeson would publish his initial work on the phi29 DNAP, and two years after that, Gundlach and Niederweis would demonstrate its power with the MspA pore. Another two years, and Oxford Nanopore would begin releasing the first MinION devices. At the heart of the MinION a method of deconvoluting the signals generated by their nanopore devices. At any given time, the signal is assumed to have contributions from five bases, referred to as a "5-mer". The overall system is treated as a Hidden Markov Model in which the hidden states (the sequence of 5-mers) produce an observable data set (the current readout). As the DNA translocates the pore, and as the successive 5-mers produce current values, a Viterbi algorithm is then used to infer the DNA sequence most likely to have produced those values.

The MinION got off to a rocky start. Early reviews noted extremely poor accuracy, with only a quarter of reads mapping to reference, and under 10% average identity. Even so, read lengths much longer than first- and second-generation techniques were readily available, fulfilling at least one aspect of the nanopore promise[24]. Within a

year, though, the platform seemed to have improved significantly. New algorithms resulted in significant accuracy improvements, with 99% of reads mapping to reference and 85% average identity being reported[25]. Oxford Nanopore continues to update both its hardware and software, so it is reasonable to expect continued improvement. The MinION has yet to match the high accuracy standards set by first- and second-generation sequencing technologies – at least not for single runs – but it already offers a viable research platform, especially in applications where long read lengths are critical.

2.3.6 Outlook for Protein Pores

With the advent and success of Oxford Nanopore's MinION, protein-based nanopore sequencing has made itself a viable part of the current DNA sequencing landscape. While there is no doubt room for improvement in each of the three challenge areas – detection specificity, translocation control, and fabrication scaling – the existence of a stable company based around a nanopore sequencing platform demonstrates empirically that a critical level of combined success has been met.

2.4   Solid-State Nanopores

2.4.1 Introduction

Even as research on protein nanopores was still in its early stages, work began on the fabrication of solid-state nanopores. There were several reasons for this. Nanopores were thought to be useful platforms for sensing applications that reached well beyond DNA sequencing. with target analytes of a wide variety of sizes. Finding appropriately-sized protein pores is not straightforward and becomes increasingly difficult as the desired size increases. Solid-state techniques, on the other hand, can be adapted to

produce structures of arbitrary size. Solid-state membranes and pores, constructed of dielectrics and metals, are also more durable than protein pores and their attendant lipid membranes. Finally, protein pores are not easily integrated with additional electronics, while the fabrication techniques used to create solid-state pores can also create a wide range of secondary structures that could be used to enhance functionality.

2.4.2   *Jene Golovchenko – Solid-State Nanopore Foundations*

The foundational study in solid-state nanopores came out of Daniel Branton's nanopore group at Harvard, under the direction of Jene Golovchenko[27]. In this study, a bowl-shaped cavity was cut into the back side of a free-standing silicon nitride membrane by reactive ion etching (RIE). The membrane was then exposed to an Ar^+ beam in order to mill away the front-side surface. The intent was to expose the cavity, thereby creating a small pore in the membrane. A single-ion detector would be used to detect the flux of ions through the incipient pore. By keeping track of the transmitted ion flux, which scales with the pore area, one can make pores of consistent size by stopping the ion milling when the desired flux has been reached.
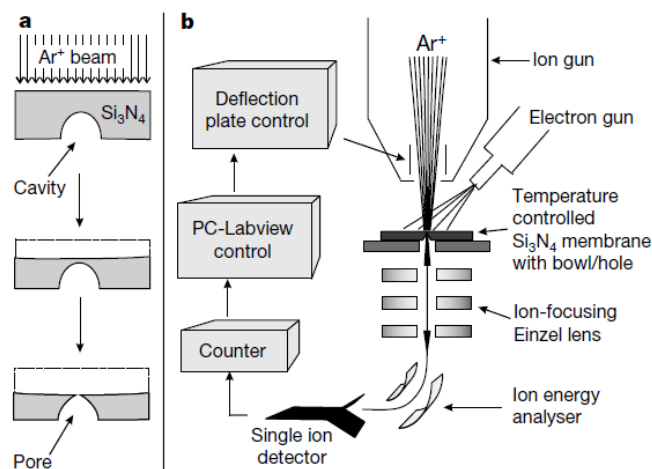
Figure 2.4.1. Nanopore Fabrication by Ion-beam Sputtering[27]. (a) Incident ion beam mills material from a silicon nitride membrane with a cavity in it. Once the top of the cavity is exposed, a pore is formed. (b) Schematic of the argon ion gun and feedback control system.

What the researchers discovered is that a pore was not formed directly on ion-beam exposure. In addition to the removal of material, the ion beam also induced lateral movement of atoms toward the beam. The rates of milling and lateral filling depended on the incident ion flux and temperature. In particular, lower flux and higher temperature resulted in a higher rate of lateral spreading. Having characterized the process, Golovchenko et al developed a new protocol for forming nanopores. Rather than an initial cavity, the membrane had a large (on the order of 50 nm) pore drilled in it using a focused ion beam (FIB) tool. The argon ion-sculpting process was then used to shrink the pore down to the desired size. As a proof of concept, DNA was translocated through these ion-sculpted pores. The first measurements showed 500-bp dsDNA translocating through a 5-nm pore at a rate of 100 bp/ms, and the field of solid-state nanopore sensing was established.
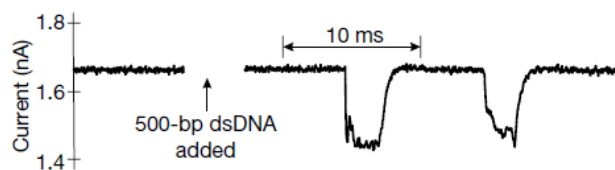

Figure 2.4.2. Translocation of DNA Through Ion-sculpted Pore[27]. 500-bp dsDNA exhibits dwell times of roughly 5 ms when driven through the pore at a 120-mV bias in a solution of 1 M KCl, 10 mM Tris-HCl, 1 mM EDTA at pH 8.0.

This first study was followed shortly by another which was the first to use a solid-state nanopore to observe structural information about single DNA molecules[28]. While most current blockade events had a single characteristic blockade level (ΔI_o) and dwell time (t_o), there was a small cluster of events with blockade level $\Delta I_B = 2\Delta I_o$ and dwell time $t_D = 0.5\ t_o$, and a set of additional events with an intermediate distribution of dwell times and blockade levels. Inspection of the current traces for these intermediate events revealed a quantized structure: each event was composed of discrete portions with instantaneous blockade levels ΔI_o and $2\Delta I_o$. This was interpreted as an indication of DNA passing through the nanopore folded over itself and therefore occupying twice as much area in the pore. The cluster of events at $2\Delta I_o$ represented DNA that was folded neatly in half, while the broader distribution represented molecules where the fold occurred closer to one end. With this model, and assuming that the speed of translocation remains constant, the average blockade level and dwell time for each of the complex events can be related as

$$< \dot{\Delta I_B} > = < \dot{\Delta I_o} > \frac{t_o}{t_d}$$

31
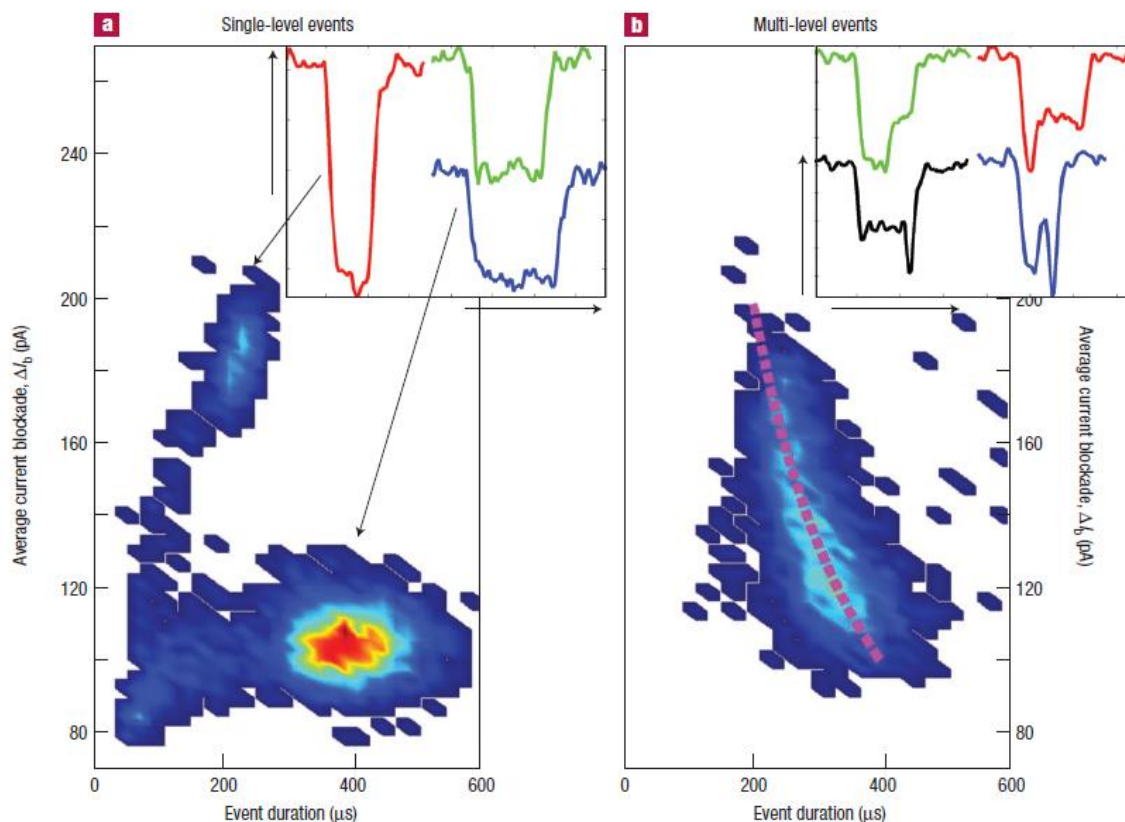
Figure 2.4.3. Blockade Currents and Durations for Translocation Events[28]. (a) Single-level events, with primary and secondary clusters. (b) Multi-level events, with dotted line corresponding to equation above.

Despite the promising start, translocation rates were still high, at 50 bp/ms, and

the authors were already looking beyond simple nanopores to enhanced structures:

> Finally, we mention that a major advantage of a microscope based on solid-state pores lies in the possibility of articulating the nanopores with electrically conducting electrodes. Such electrodes can allow electronic tunnelling and near-field optical studies of translocating molecules that are linearized and confined in a nanopore of the microscope. Applying these new physical local interactions to molecules translocating through nanopores can provide local single molecule spectroscopies not afforded by measurement of ionic current alone, and offer a means of increasing

longitudinal resolution, possibly to the single-base level for DNA, allowing for extremely rapid sequencing of long molecules[28].

2.4.3 *Cees Dekker – Electron Beam Sculpting and Pore Dynamics*

One of the most prolific and significant groups performing solid-state nanopore research is headed by Cees Dekker at Delft University of Technology in the Netherlands. Not long after the introduction of ion-beam sculpting at Harvard, Dekker and colleagues developed a similar technique for shaping pores with single-nanometer precision[29]. They began with silicon membranes with a 40-nm surface layer of thermal silicon oxide into which were wet-etched pores with width up to 200 nm. On exposure to a TEM beam with intensity from 10^5 to 10^7 A m^{-2}, two different effects were observed, depending on the size of the initial pore. For pores with an initial diameter greater than about 80 nm, exposure to the beam caused the pore to expand. Pores with an initial diameter smaller than about 50 nm, on the other hand, began to contract at a rate of about 0.3 nm per minute. This rate allows for fine tuning of the pore size with a precision that is only limited by the instrumental resolution (0.2 nm here) and the surface roughness of the silicon oxide (1 nm).
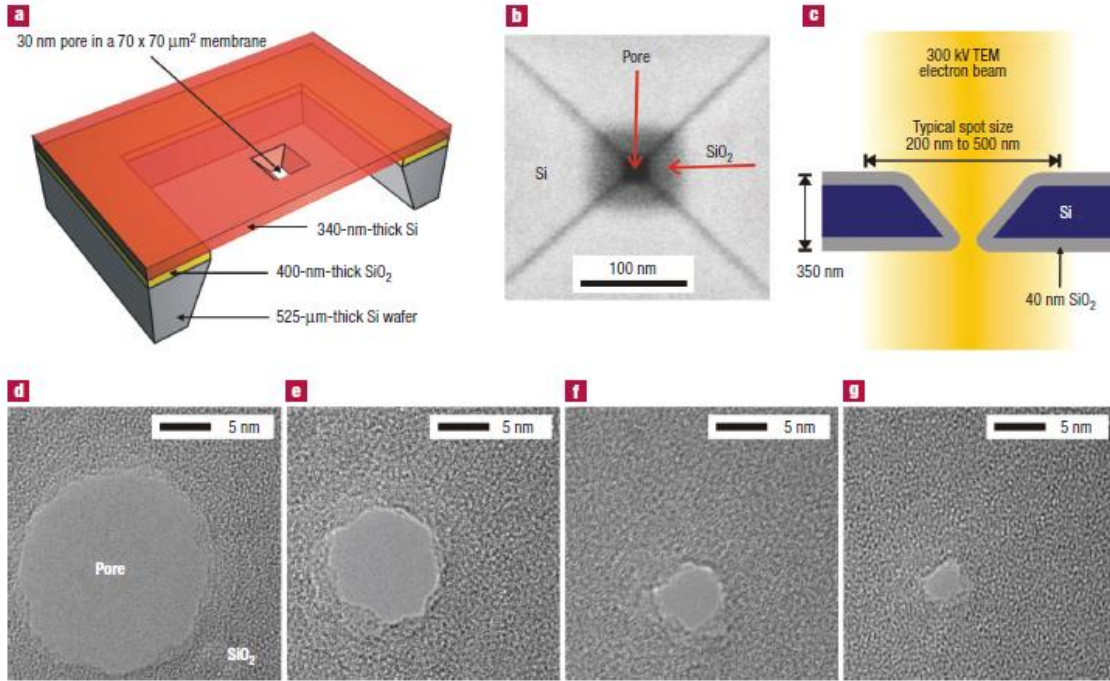
Figure 2.4.4. Fabrication of Silicon Oxide Pores[29]: (a) Cross-section view of device. (b) Top-view SEM of wet-etched pore. (c) Cross-section view of pore inside the TEM. (d)-(g) Sequence of TEM images during the shrinking of a pore down to 3 nm.

The behavior of the pore is explained as a result of surface tension in the silicon oxide that has been fluidized by the electron beam. When compared to an intact sheet of material, a sheet with a cylindrical pore of radius r and thickness h will have a free energy given by

$$\Delta F \; = \; \gamma \Delta F = 2\pi(rh - r^2)$$

where γ is the surface tension and ΔA is the change in surface area. This function has a maximum at $r = h/2$, suggesting that pores with diameter less than the membrane

34

thickness will tend to shrink, while pores with a diameter greater than the membrane thickness will tend to grow. This is in qualitative agreement with the experimental results, in which the membrane thickness was estimated to be 40 nm and the critical diameter between 50 nm and 80 nm.

The surface tension model received additional validation from experiments performed on pores which were initially drilled directly into a 10-nm SiO_2 membrane with a focused electron beam. In this case, the critical diameter between pore expansion and contraction was found to be 10 nm, in agreement with the model.

In addition to developing this widely-used method for fabricating high-precision solid-state pores, the Dekker group has made many contributions to the understanding of solid-state pore dynamics. In 2005, they characterized translocation rates of long dsDNA molecules through solid state pores[30]. They discovered that in contrast to protein pores, where dwell times scale linearly with molecule length, solid-state pores exhibit a different scaling, namely $\tau \sim L_o^{1.27}$. A model is proposed which compares translocation times with the relaxation time of the coiled polymer. By the terms of the model, DNA displays "fast" translocation through solid-state pores, whereas protein pores involve "slow" translocation.

The same year, they proposed a method for sculpting nanoelectrodes with a TEM beam[31]. This process was able to construct electrode tips with a radius of curvature of approximately 2 nm and a separation of roughly one nm. While the immediate application was for sensing nanoparticles, the dimensions suggested use in a hybrid nanopore-nanogap structure.

Other research from the group includes the effect of salt concentrations on translocation signals[32], measuring translocation forces with optical tweezers[33], using nanochannels to electrokinetically concentrate DNA for more efficient capture[34], detecting local protein structures along DNA[35], and slowing DNA translocation by using alternate electrolyte cation[36].

2.4.4   *Amit Meller – Array Fabrication and Parameter Tuning*

Having worked with Daniel Branton's group on some of the most important early research with protein nanopores[8,9], Amit Meller also worked on solid-state pores, investigating several ways to improve fabrication strategies and device performance. In one such study, Meller and colleagues introduced a variation on the TEM-drilling technique pioneered by Dekker[29,37]. That technique, while capable of producing high-precision pores, took a relatively long time (on the order of several minutes) to shape each pore. Having in mind massively parallel sensing techniques such as fluorescent imaging, Meller wanted to develop a pore-forming method that could reliably and quickly produce an array consisting of a large number of pores on a single device chip. The approach was to increase the intensity of the electron beam during the pore sculpting process. This achieved a five-fold reduction in direct fabrication time to about 30 s per pore without significantly sacrificing reproducibility of the pore dimensions. An alternate process using the automated beam deflection capabilities of a STEM was also demonstrated.
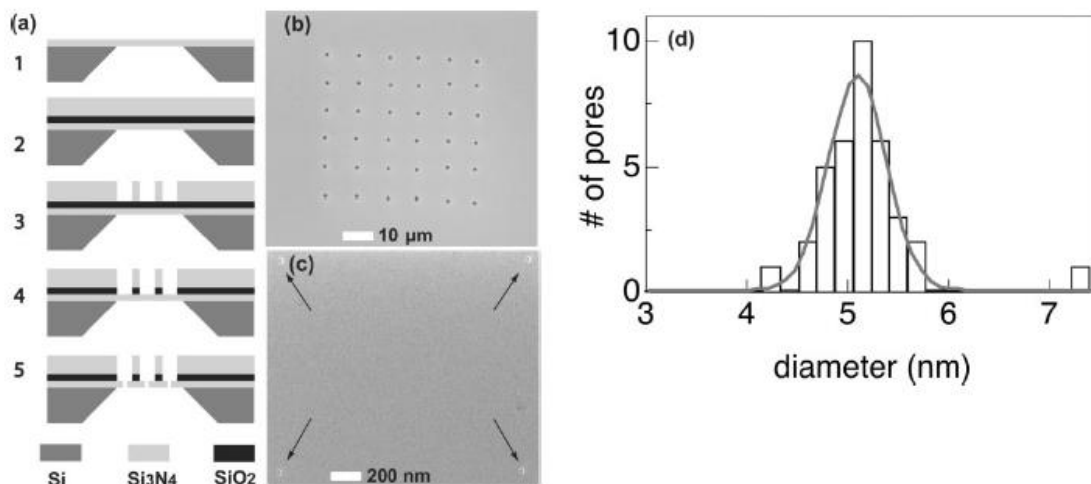
Figure 2.4.5. Nanopore Array Fabrication[37]. (a) Schematic of fabrication process, showing etching of wells prior to TEM drilling. (b) 6 x 6 array of 5-nm pores fabricated in 2-µm wells. (c) 2 x 2 array of 20-nm pores fabricated with STEM. (d) Size distribution of the pores from (b).

Some years later, this research was followed up by the construction of a proof-of principle optical nanopore array[40]. Here, DNA was tagged with fluorescent beacons which were too large to fit through the pore. During translocation, the beacons were sequentially stripped from the DNA, emitting photon bursts which can be recorded in parallel.

In another study, Meller investigated surface interactions between solid-state nanopores and DNA[38]. This very detailed study probed several different phenomena. First, distributions comparing the average fractional current during blockade events with dwell times show two broad classes of events. Events with relatively small reduction in current and short times are interpreted as collision events, where the DNA partially blocks the pore without passing through. The other events, with longer dwell times and greater current reduction, are true translocation events. Significantly, as the pore size

37

increases, the relative population of collision events decreases as a greater fraction of molecules encountering the pore are able to pass through.
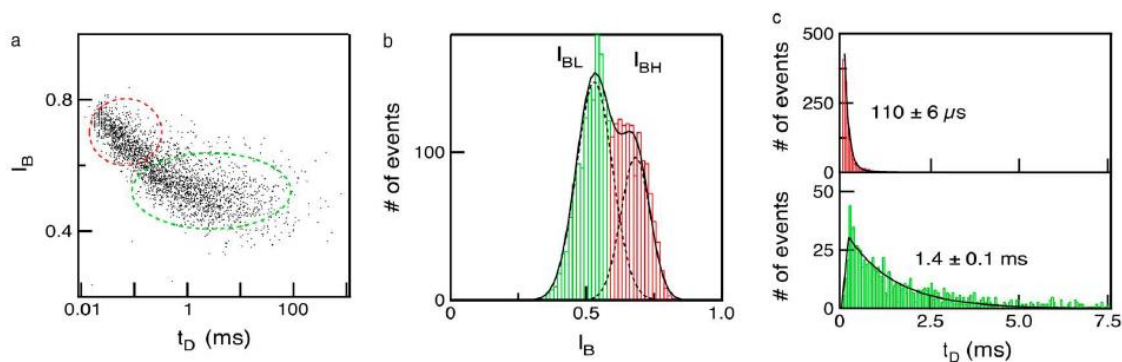

Figure 2.4.6. Event Distributions for 6 kbp dsDNA[38]: (a) Scatter plot of events showing two distinct populations. (b) Histogram for fractional current. (c) Dwell time distribution for each population.

The size of the nanopore also strongly affects translocation times. While collision-event times are mostly unaffected by pore size, translocation times increased by a factor of 100 on reduction of the pore diameter from 8 nm to 4 nm. This change is not explainable based on hydrodynamic drag inside the pore, suggesting increased interactions with the pore surface may be responsible. While Dekker, et al showed dwell times related to DNA length by a power law with an exponent of 1.27, this study indicated two power laws. For molecules from 150 – 3500 bp in length, the exponent is found to be 1.40, while for longer molecules, the exponent is 2.28. Furthermore, translocation times are also increased by decreasing the electrolyte temperature. This slowing effect is several times more than can be accounted for by the increase in fluid viscosity from the reduced temperatures and once again points toward interactions between the DNA and the pore surface.

While smaller pores were shown to have much more favorable kinetics in terms of average dwell times, the tradeoff was a significant decrease in capture rate. As the pore size decreases, an increasing fraction of incident DNA bounces off the pore rather than passing through it. In addition, we see a decrease in the radius at which the electric field is strong enough to direct DNA toward the pore. In an effort to combat this problem, Meller et al investigated the effect of various parameters on the capture rate[39]. Increasing the DNA length resulted in about a 10-fold increase in capture rate between 1 kbp and 10 kbp, but the capture rate remains essentially constant above 10 kbp. Likewise, increasing the driving potential from 200 mV to 500 mV also increased the capture rate about 10-fold, but increasing driving potential comes at the cost of decreasing dwell times. The most interesting result came from establishing a salt gradient across the pore. By increasing the electrolyte concentration in the *trans* chamber, both cations and anions will naturally flow through the pore into the *cis* chamber. The driving potential, however, prevents anions from passing, resulting in a buildup of positive charge on the *cis* side of the pore. This charge accumulation enhances the field near the pore and increases the capture radius for negatively-charged DNA. This results in a capture rate enhancement factor that scales roughly linearly with the concentration ratio C_{trans}/C_{cis}. Interestingly, the salt gradient also has the effect of slowing DNA translocation, as the increased flow of cations from trans to cis increases the electroosmotic drag force on the DNA.
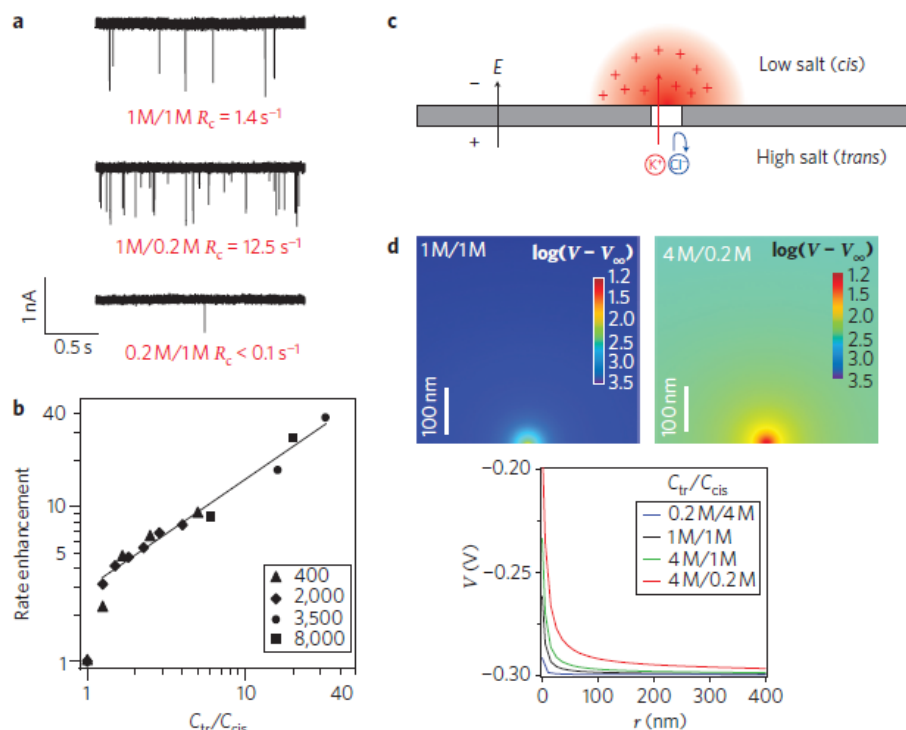
Figure 2.4.7. Effects of Salt Gradient Across Pore[39]. (a) Ion current traces showing enhanced and suppressed capture rates due to higher and lower *trans* salt concentrations, respectively. (b) Relationship between concentration ratio and capture rate enhancement. The enhancement does not depend on DNA length. (c) Schematic of salt gradient across pore showing buildup of cations on *cis* side. (d) Electric potential strength outside *cis* pore for symmetric and asymmetric salt concentrations.

2.4.5   Adam Hall – Fabrication Scalability

Another group addressing issues that have affected solid state nanopore

fabrication is led by Adam Hall from UNC Greensboro. Hall originally worked with

Cees Dekker at Delft University of Technology in the Netherlands, where he did research

on how TEM conditions during pore formation affect the subsequent stability of pores in

aqueous solution[41], as well as working on a hybrid protein/solid-state nanopore with

Dekker and Hagan Bayley[42]. More recently, he has been working on a technique called

helium ion milling that aims to significantly increase fabrication throughput compared to traditional ion sculpting or TEM ablation[43]. While these processes yield high-quality pores, they can only process one device at a time, and processing can take from minutes up to an hour, not including microscope pumping time. At the same time, other techniques that can produce pores rapidly produce pores that are either too big to be directly used for DNA experiments or demonstrate functional limitations for later use[44,45]. What is needed is to be able to produce high-quality pores in a fast, scalable, single-step process.

The tool of choice for this process is the helium ion microscope (HIM), which uses a beam of helium ions rather than electrons or other ion species. HIM uses an atomically-sharp tip to form a beam with a probe size of only 5 A. A pore of < 5-nm diameter can be produced with a single exposure of less than 1 s, with an example chip having an 11 x 11 array of pores produced in approximately one minute, and the chamber design allows for up to 100 samples to be loaded at once with an appropriately-designed sample holder. While these pores do not have the same size precision as traditional ion- or electron-beam nanopores (Hall reports variance of +/- 3nm), the high throughput means that a larger number of devices of a desired size can be made in a given time.
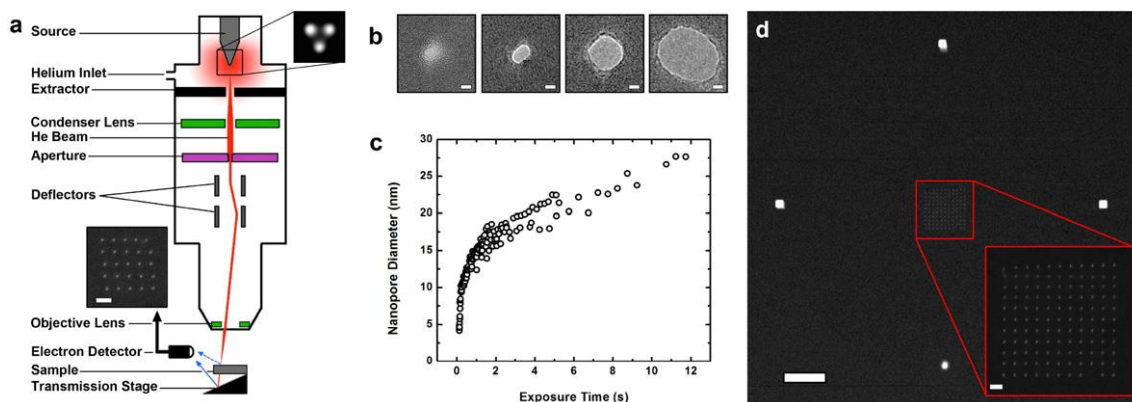
Figure 2.4.8. Helium Ion Microscope Pores[43]. (a) Schematic of helium ion microscope (HIM); (b) Pores of various sizes produced by the HIM, scale bar 5 nm; (c) Distribution of nanopore sizes based on exposure time; (d) 11 x 11 array of 5-nm diameter pores, scale bar 500 nm, inset scale bar 50 nm.

Work on this technique has continued with studies aiming to more accurately

characterize the milling process[46] and permit in-situ measurement of milling thickness[47].

2.4.6 Control Electrodes

After the first studies characterizing the basic behavior of DNA translocating

through solid-state pores, it became increasingly clear that solid-state nanopores by

themselves would not be sufficient for sequencing. In particular, translocation rates

through synthetic nanopores are even higher than those through non-functionalized

protein pores. While we have already seen a number of studies that show slight passive

reduction of translocation speed by such means as adjusting parameters of the electrolyte

solution, none have come close to demonstrating the three to four orders of magnitude

reduction that would be necessary for single-base reading. Active approaches are

required, and one of the most popular ideas has long been to use an additional set of

control and/or sensing electrodes at the pore. Many ideas have been proposed, and a few are here described in somewhat greater detail.

An early strategy for fabricating control electrodes in a solid-state nanopore device was developed by Gustavo Stolovitzky. He introduced the concept of a set of layered electrodes forming a sandwich structure in the membrane[48]. In this design, the membrane consists of dielectric structural layers on either side of an electrode stack. The electrode stack would consist of three thin metal layers separated by dielectric films. By precisely tailoring the thickness of the central layers (the inner metal layer and the two dielectric layers) relative to the nucleotides, Stolovitzky predicted the ability to trap DNA in a potential well and then step it one base at a time through the pore. In particular, the dielectric layers would need to be half-integer multiples of the single-base separation, and the central layer would need to be close to an integer multiple. In this geometry, a potential difference between the outer electrodes and the inner electrode would create an energy well that would trap the DNA. By switching the in-pore potential on and off while holding a constant trans-pore bias, the DNA could be stepped through one base at a time.

Figure 2.4.9. Through-pore Electrode[48]. Top – (a) cross-section of electrode structure showing central electrode potential (V0) and width (W), as well as inter-electrode separation (S). Bottom – (a), (b) force and (c) energy profiles for DNA moving through the pore.

The conceptual introduction was followed by an MD simulation demonstrating

the predicted performance of the ratcheting mechanism[49]. This was followed by

experimental studies related to electrochemical protection of the electrodes[50,51]. Two

44

main challenges were addressed: unwanted redox reactions at the electrodes and generation of hydrogen and oxygen bubbles from water hydrolysis. A number of protective strategies were formulated, including surface coating with a monolayer of hexadecylphosphonic acid and adding glycerin or poly(ethylene glycol) to the solution. To date, no research has been published by this group demonstrating translocation of DNA through the in-pore electrodes, though the architecture may be adopted by other groups.

Marija Drndic tried a method of aligning a transverse electrode gap to a drilled nanopore based on "transmission electron beam ablation lithography" or TEBAL, a technique she had earlier developed for creating metal nanostructures on silicon nitride structures[52,53]. In a TEBAL process, a rough initial metal structure is fabricated using standard lithography and lift-off techniques. After this, a TEM beam can be used to sculpt the metal into nanostructures with sub-nanometer precision. For most metals, the electron beam removes atoms from the surface, but gold is heavy enough that it does not ablate. Rather, gold crystallizes, allowing for sculpting by careful manipulation of the beam around the target area. Examples of TEBAL structures include nanowires, nanochannels, and nanogaps all under 5 nm.
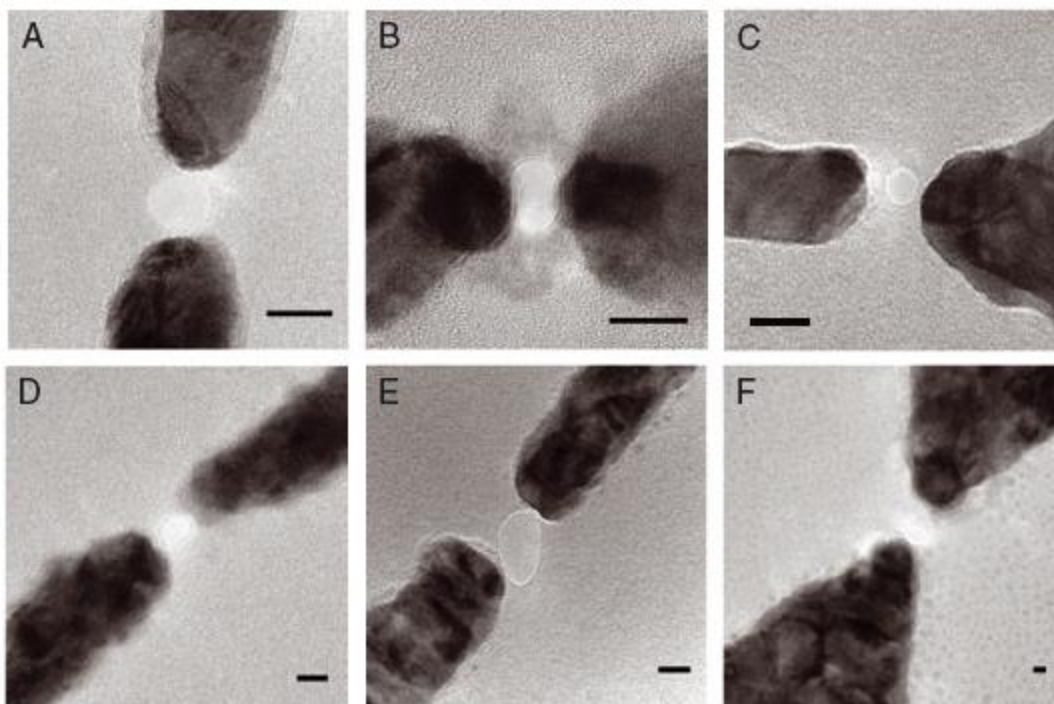
Figure 2.4.10. TEBAL Electrode-Nanopore Devices[53]. (a)-(f) Nanopore-nanoelectrode devices with pore sizes ranging from 2.5 nm to 30 nm. All scale bars 10 nm.

In order to make the nanopore-nanogap devices, a starting electrode gap was fabricated by electron beam lithography. Next, the electrodes were sculpted into the desired shape by TEBAL, and then the nanopore was drilled with the electron beam. Unfortunately, this process suffered from very low yield. Over a period of two years, 300 devices were fabricated. Only 15% of the devices survived the fabrication process, the rest suffering failures due to mechanical shock or electrostatic discharge. Of those that survived, a number failed to capture translocation events via ionic current, a failure that could not be replicated by control chips containing pores but no electrodes. This might suggest some blocking of the pore by the electrodes, possibly either a migration of atoms

46

physically blocking the pore or an accumulation of surface charge repelling DNA from the pore entrance. Of the few chips which both survived fabrication and registered translocation by ionic current, none was able to record a stable and sensible tunneling current.

Joshua Edel used another method of aligning a transverse electrode gap with a drilled nanopore[54]. This technique was performed inside a dual-beam FIB/SEM machine. The starting device contained a 70-nm thick SiN_x membrane over which was aligned a pair of gold electrode tips with a 2-µm gap. Initial pore fabrication followed standard FIB milling techniques, resulting in a 50-nm pore drilled through the membrane. Next, a pair of platinum electrodes with a nanogap separation was fabricated by electron beam induced deposition (EBID). EBID is a process commonly performed in an FIB tool, where it is typically used to provide a protective Pt layer on top of a structure that is about to undergo milling. In the process, a gaseous methylcyclopentadienyl(trimethyl)Pt precursor is introduced to the sample. The application of an electron beam to the surface decomposes the precursor and results in the deposition of Pt metal in an amorphous carbon matrix on the sample. In this way, metal structures can be directly "written" onto a sample. In the experiment as described, a nominal gap separation of 50-60 nm produced an actual gap of about 3 nm due to lateral broadening. By aligning the EBID electrodes with the initial pore, they produce a hybrid pore structure that begins with a relatively large pore but passes through a constriction composed of tunneling electrodes.
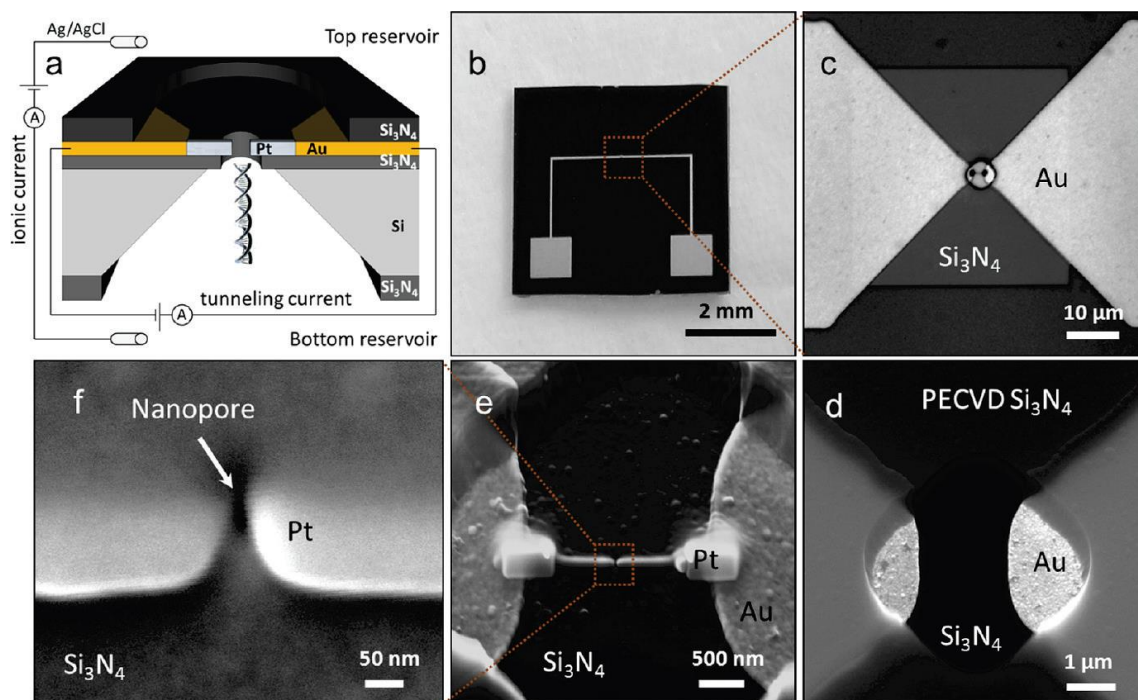
Figure 2.4.11. Nanopore with Transverse Electrodes by EBID Pt Deposition[54]. (a) schematic showing ionic and tunneling circuits, (b) overview of device chip, (c) gold electrodes overlaid on SiN_x membrane, (d) RIE opening in SiN_x passivation layer, (e) Platinum electrodes deposited by EBID on the ends of the Au electrodes, (f) close-up of Pt electrodes showing nanopore.

With this setup, the group was able to simultaneously record the translocation of λ-DNA by both ionic current and tunnel current, though with some significant caveats. The majority of events could only be seen by ionic current, and translocation speeds for these type I events were extremely high at 160 kbp/ms. Another, slower set of events could be detected by both ionic current and tunneling current. These type II events had a mean translocation speed of 10.3 kbp/ms for tunneling signals and 7.7 kbp/ms for ionic signals. Some, but not all, of the type II events were detected by both tunnel current and ionic current.

48

Separate from the task of constructing hybrid nanopore/nanogap structures that can produce tunnel current or other data from direct measurements at the pore is the matter of characterizing and interpreting that data. Much effort on that score has been put forth by Stuart Lindsay and his group at Arizona State University. While most of his published research to date has focused on measurements made with scanning tunneling microscopes (STM) and is therefore not strictly applicable to a review of nanopore techniques, such research has been done with a view toward eventual application in nanopores and is particularly relevant for my research.

The Lindsay group's research is centered around a concept known as recognition tunneling[55]. Rather than obtaining signals from bare electrodes – which are hypersensitive to geometrical conditions – recognition tunneling makes use of electrodes functionalized with so-called "reader molecules". These molecules form hydrogen bonds with the nucleotides as they pass through the pore in order to form a electrode-reader-base-reader-electrode molecular junction. This improves on tunnel-current sensing with bare electrodes in two ways: (1) the signals through the reader junction are much less sensitive to pore geometry than those from bare electrodes[56], and (2) the hydrogen bonds that form the junction hold the nucleotide in a particular orientation, which should narrow the distribution of signals generated by each base. Studies to date have shown that in an STM configuration, reader molecules produce distinguishable signals for each of the four nucleotides and that the distribution of signals using reader molecules is much sharper than those from bare electrodes[57].
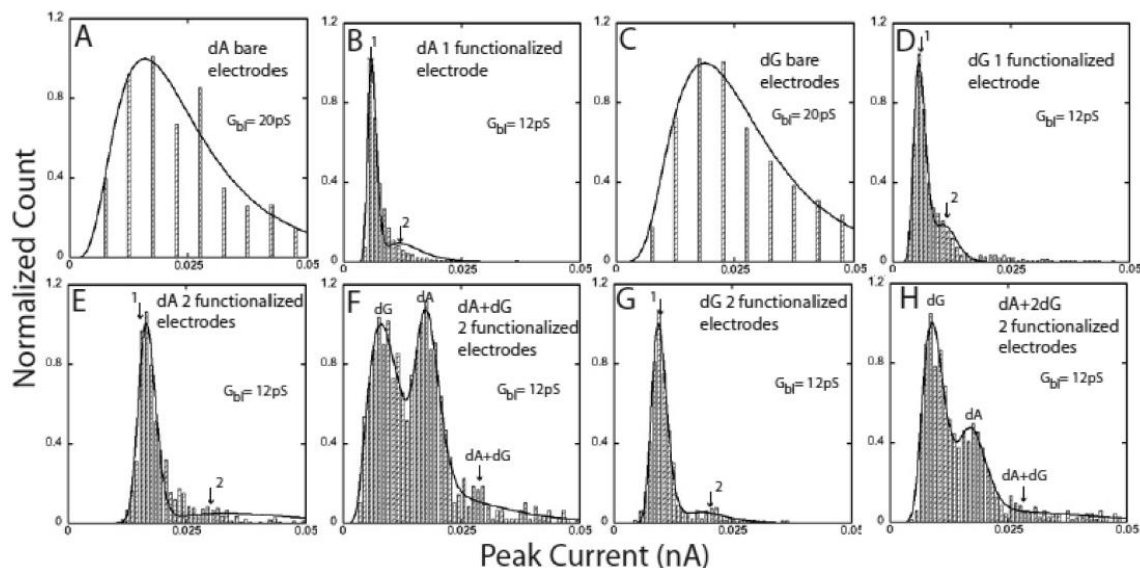
Figure 2.4.12. Effects of Electrode Functionalization[57]. Peak current distributions for various electrode and nucleotide configurations.

No study has yet been published demonstrating recognition tunneling signals from DNA translocating a nanopore. It has, however, been demonstrated that the hydrogen bonding from reader molecules plays a useful role in slowing translocation speed through a nanopore[58]. When a pore is functionalized with reader molecules at the *cis* opening, translocation is slowed by an order of magnitude compared to a non-functionalized pore. This affect appears to be the result of the reader molecule forming hydrogen bonds with the DNA, as pores functionalized with similarly-sized molecules unable to form hydrogen bonds show no slowing effect.

2.4.7   *Outlook for solid-state pores*

The immediate future for solid-state pores does not look as bright as the outlook for protein pores. Relative to protein pores, solid-state pores suffer from lack of reproducibility and fine control over dimensions, poor spatial resolution, and no

demonstrated control over translocation. Even areas where solid-state pores should have an advantage, such as the ability to acquire tunneling signals, have thus far remained just out of reach. Despite the slow progress, the possibilities that would be opened from a successful solid-state nanopore sensor have kept interest in the field alive.

2.5   Conclusions

In summary, both biological and solid-state approaches have made strides toward the realization of nanopore sensors as a viable third-generation DNA sequencing technology. Protein pores have seen the most success to date, but solid-state pores continue to attract research due to the ease of electronic integration and the potential benefits of integrated control electrodes. Significant challenges remain, however, and there is a continued opportunity for new strategies to help overcome those challenges.

3. SOLID-STATE NANOPORE SENSOR

3.1 Device Design

3.1.1 Design of the Nanopore

The first project that I am working on involves a novel approach to constructing a solid-state nanopore sensor. To recap some of the main conclusions from the review of nanopore sensing strategies in Chapter 2, there are several essential challenges that need to be met. The first challenge is specificity of detection. Ideally, we want a signal that has single-base sensitivity. Oxford Nanopore has shown the capability of extracting sequence information from a convoluted signal, but the analysis problem becomes increasingly complicated with every additional base that contributes to the signal. The second challenge is controllability of translocation. Per-base transit speed must be slowed down sufficiently to match the bandwidth of recording electronics. The last challenge is reproducible and scalable fabrication. We must be able to consistently and efficiently produce devices.

The first two conditions mean that control electrodes are a must for a solid-state pore. Single-base resolution is impossible with ion current, and simple solid-state pores have very high transit speeds. Control electrodes allow us to (1) use transverse tunnel current as the primary probe (and let us cross-check with ion current), and (2) apply a local electric field at the pore as a means of slowing down the DNA. But how shall we implement control electrodes? As we have seen, top-down alignment of transverse electrodes to a pore is extremely difficult. The through-pore sandwich structure is self-

aligned, but hard to control the pore diameter through multiple layers and cannot achieve single-base resolution across the gap.

Both approaches are based on an architectural paradigm where the fluid is confined in bulk chambers separated by a thin membrane, but let us instead consider a different model for fluid transport: the microfluidic channel. Micron-scale channels for fluid transport are employed in a wide range of devices, and they are constructed in such a way that flow is generally in the same plane as the device substrate. There are a few ways to make a microfluidic channel. One is to construct a mold which a material such as PDMS is poured onto and allowed to cure. After curing, the PDMS is removed from the mold and bonded to the substrate. The space left by the mold contains the channel. Another method is to directly build the channel walls out of a patternable polymer such as SU-8. A flat slab of PDMS can then be added on top to seal the channel. A third method is to construct a channel using a sacrificial layer. The shape of the channel is created on the substrate out of a solid material, and then mostly sealed, leaving one or more access points. An etching fluid is then introduced which dissolves the sacrificial layer, leaving the fluid channel behind.

Top-down lithography can easily align an electrode pair with a sub-micron gap to a microfluidic channel (more precisely, to a sacrificial layer that will become a microfluidic channel) with sub-micron precision. Since the height of the channel is determined by the thickness of the sacrificial layer, it is easy to constrain it to less than 10 nm. Depending on the type of lithography used, the width of the electrode gap can be reliably fabricated from tens of nanometers to about a micron. After the sacrificial layer is etched, there is now a self-aligned rectangular channel with a height of 10 nm and

width of 1 µm (assuming photolithography is used to fabricate the electrode gap) whose walls are the edges of the two electrodes. Unfortunately, the width of the pore is too great for electron tunneling, and the cross-sectional area too big to obtain structural data from an ion current, if it can detect translocation at all.

The solution to both these problems comes in the form of electrochemistry. Since the side walls of the pore are the electrode tips, they can be held at an electric potential that allows for the reduction of metal ions in the surrounding solution. In this way, the two electrodes can grow toward each other, shrinking the gap until it is small enough to read both a tunnel current across the electrode gap and an ionic current through the nanopore. Electrochemical deposition has previously been used for the controlled closing of a nanogap between two electrodes, but only for electrodes without any confinement in the z-direction. The embedding of the electrodes in a microfluidic channel allows for the creation of a true nanopore.
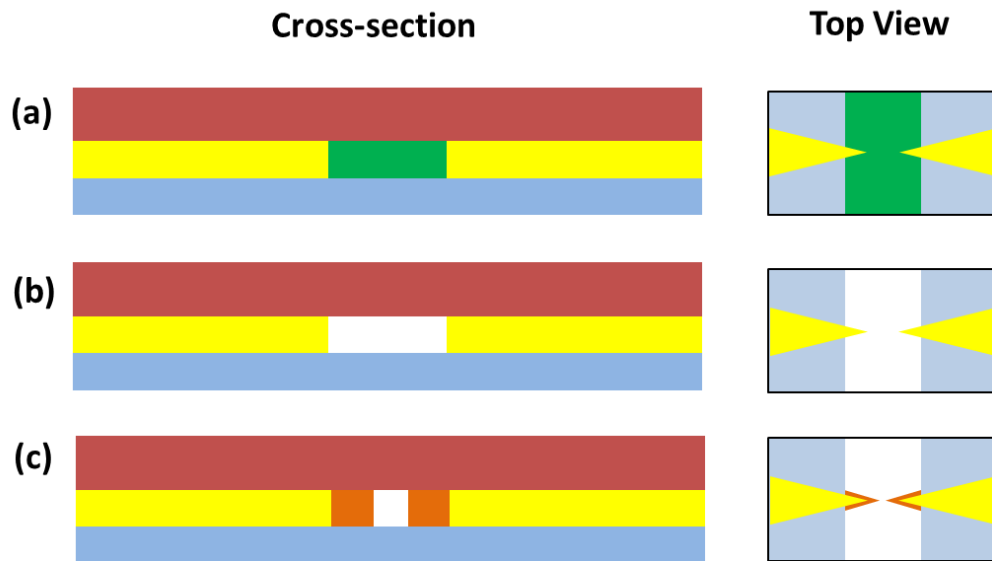
Figure 3.1.1. Nanopore Design. (a) Initial fabrication, including substrate (blue), electrode tips (yellow), sacrificial layer (green), and passivation (red). (b) Etching of sacrificial layer to create nanochannel. Electrode tips form constriction in channel. (c) Electrochemical deposition of additional metal (orange) onto the electrode tips narrows the constriction, forming the nanopore. Dimensions not to scale.

3.1.2 *Design of the fluid system*

Designing the microfluidic system for such a device is not straightforward because it needs to accomplish several tasks. The most critical portion of the fluidic system is the channel leading to the nanopore. This channel need to have a height of less than 10 nm, since the height of the channel determines the height of the nanopore. The surrounding material also needs to be rigid to ensure that the channel does not collapse and cut off analyte molecules from the pore. Finally, the channel needs to be aligned with the electrode gap to sub-micron precision. All of these requirements point toward using a sacrificial layer approach for this channel. Depositing a metal sacrificial layer allows for very small thicknesses and the metal can be precisely aligned with photolithography, whereas aligning a molded PDMS sacrificial layer to better than 10-µm accuracy is extremely difficult. Furthermore, using a sacrificial layer allows the channel to be sealed by depositing a rigid dielectric material on top of the metal. A 10-nm high channel constructed out of PDMS could collapse in the middle and would be unlikely to effectively confine the electrochemically-deposited metal on the electrode tips.
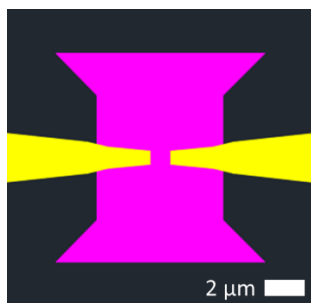
Figure 3.1.2. Dimensions of Central Nanochannel and Electrode Tips. Nanochannel (magenta) is 10 nm tall, 10 µm long, and 6 µm wide. Electrode tips (yellow) are 600 nm wide, and the tip separation is 1 µm.

Another requirement for the fluid system is the need to provide a macroscopic interface to exchange solutions and to measure the ionic current passing through the nanopore. During the course of nanopore preparation and measurement, several different fluids will need to be used: Etchants for removing sacrificial layers, pure water and/or buffers for rinsing the chip, a solution containing metal ions for electrochemical deposition, and a solution containing the analyte molecules. This requirement necessitates a millimeter- to centimeter-length bulk fluid chamber with inlet and outlet ports that can connect to microfluidic tubing. By itself, the length requirement rules out the use of sacrificial layers to construct the bulk chamber, as chemical etching would take a prohibitively long time at typical metal etching rates of 1-10 nm/s. Further, we need to consider the requirement of detecting the ion current. If we establish a bias between electrodes on either side of the pore, we want to ensure that most of the potential drop occurs at the pore itself. Since the resistance of a wire scales with the length divided by the cross-sectional area, we can determine the required cross-sectional area of the chamber to avoid degradation of the current signal. If we estimate the central pore as a cube of side length 10 nm, the geometric contribution to the resistance is 10^{-8} m / (10^{-16}

56

m^2) $= 10^8$ m^{-1}. If we estimate the length of the chamber as 1 cm, we can solve for the cross-sectional area that would produce an equal amount of resistance: 10^8 m^{-1} $= 10^{-2}$ m / A. This gives us A $= 10^{-10}$ m^2, equivalent to a chamber with width and height both equal to 10 µm. In practice the bulk chamber width is 250 µm and its height is 40 µm, reducing the chamber's contribution to the resistance by a factor of 100. In order to build a chamber with such large dimensions, the preferred methods are either PDMS molding or direct construction with SU-8 and flat PDMS. Both methods have been used in this project, but SU-8 and flat PDMS has become the standard method due to better alignment accuracy.

Because of the wide disparity between the dimensions of the central nanochannel and the outer bulk chamber, it was useful to also design an intermediate structure between the two. The intermediate channel also helps to unwind DNA molecules before they reach the nanochannel. This is accomplished by tapering the intermediate channel as it approaches the nanochannel. When a bias is applied across the pore, the tapered shape of the intermediate channel will produce an electric field gradient which will result in an effective stretching force on DNA molecules.
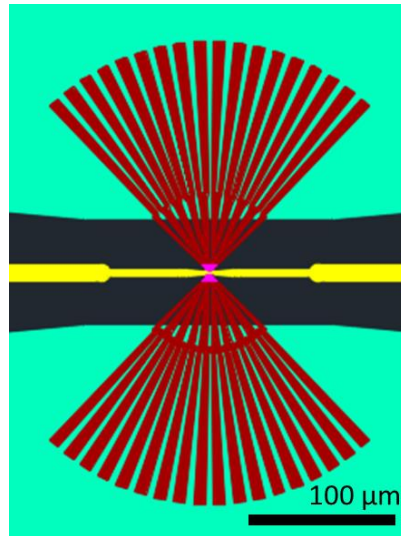
Figure 3.1.3. Intermediate Fluid Channel. The intermediate fluid channel (red) forms an interface between the nanochannel (magenta, at center) and the bulk chambers (cyan) on either side of the nanopore.

3.1.3 *Material Choices*

While the geometry of the device is critical for producing an effective sensor, the materials chosen for each part can play an equally important role. We can first consider the nanogap electrodes. When the inner sacrificial layer is etched to create the nanochannel, the etchant will be in contact with the electrode tips. We therefore want the electrode material to be chemically resistant. This suggests a noble metal such as gold or platinum. In addition to being chemically resistant, gold is also an excellent electrical conductor and the patterned evaporation of gold thin films is very straightforward. All this makes gold an appropriate choice for the initial electrode material. For similar reasons, gold was also chosen as the material for the electrodeposition material.

Next it is instructive to consider the material that is used to seal the nanochannel and passivate the electrode lines. It must be a dielectric, since it will be in contact with the electrodes. It should be resistant to any of the etchants that will be used to remove the

passivation layer. It should seal tightly to the sacrificial layer and electrodes to avoid the formation of leakage paths. It should also be rigid so that it will neither sag into the nanochannel nor be pushed up by the electrodeposited meta, as illustrated in Figure 3.1.4. After testing a few candidate materials, it was decided to use hafnium oxide deposited by atomic layer deposition (ALD). ALD is a variety of chemical vapor deposition which results in high-density conformal films.

Figure 3.1.4. Nanochannel Deformations. If the passivation material is not rigid enough, it can either (a) sag into the nanochannel and disrupt flow or (b) be pushed up by the electrodeposited metal, ruining the pore confinement. Schematics are cross-sections using the same color scheme as Figure 3.1.1 above.

The material for the sacrificial layers also takes some thought. For the inner sacrificial layer, a metal that produces very uniform films and that can be reliably etched was required. While there are many metals that would suffice, chromium was chosen in part because of its etching properties. Chromium is more difficult to etch than metals like magnesium, nickel, or aluminum. Combining a Cr inner sacrificial layer with an outer layer composed of a different metal would allow for the complete removal of the outer sacrificial layer while keeping the inner sacrificial layer intact. This in turn allows for greater control over the conditions in which the central nanochannel and the nanogap electrodes are exposed.

For the outer sacrificial layer, a higher etching rate is desirable due to the relatively large distances that need to be etched. The length of the outer sacrificial layer

from the edge of the macro-channel to the edge of the central channel is about 30 µm. At a rate of 1 nm/s, it would take more than 8 hours to etch completely through. The use of Mg for the outer sacrificial layer was explored due to its observed etching rate of about 100 nm/s in 100 mM HCl, but it was ultimately abandoned because of difficulty in reliably evaporating Mg films and because its high reactivity made it incompatible with the reactive ion etching (RIE) process used to cut through selected portions of the HfO_2 passivation layer.

Finally, material changes in the overall substrate for the devices were made. Initial fabrication was done on silicon wafers coated with silicon oxide, which are a very convenient substrate for top-down fabrication, allowing for the reliable use of techniques such as electron-beam lithography (EBL) and scanning electron microscope (SEM) imaging. Eventually, glass slides were chosen as the substrate of choice for two main reasons. First, moving to an insulating substrate provided more reliable electronic isolation between the two electrodes, especially in cases where AC fields are used. Second, a transparent substrate allows for easy backside optical access to the nanopore. This lets us do experiments with fluorescent markers and allows us to optically monitor the electrochemical deposition process.

3.2   Electrochemical Deposition

3.2.1   Introduction

The key insight in the design of the nanopore sensor is that the size of the electrode gap in the nanochannel can be altered in a bottom-up fashion by carrying out electrochemical reactions in the channel. Electrochemistry describes a branch of

60

chemistry where either (1) the application of an electric current to an electrode in contact

with a solution drives chemical reactions in the solution, or (2) reactions in a solution

result in the flow of electrons into an electrode. In all electrochemical reactions,

electrons are transferred between a bulk conducting electrode and molecules or ions at

the surface of the electrode. When an external potential is used to drive a reaction, the

free energy of the system is altered.   From a kinetics standpoint, this changes the relative

rates for the forward and reverse reactions. From a thermodynamics standpoint, this

changes the equilibrium concentration of the products and reactants. The central

equation of electrochemistry is the Nernst Equation, which states

$$E = E° + \frac{RT}{nF}\ln(\frac{C_o}{C_r})$$

where E is the system potential, R is the ideal gas constant, T is the temperature, n is the

number of electrons participating in the redox reaction, F is the Faraday constant, the

charge in Coulombs of a mole of electrons, C_o is the concentration of oxidized species,

and C_r is the concentration of reduced species. E^o is the potential at which there are equal

concentrations of oxidized and reduced species. E^o is usually defined in relation to a

standard or reference potential, most commonly the Normal Hydrogen Electrode (NHE),

but frequently a silver electrode coated in solid silver chloride (Ag/AgCl). The Nernst

Equation allows us to calculate the effect of a change of potential on a given redox

system.

3.2.2   Cyclic Voltammetry

A key practice in electrochemistry is cyclical voltammetry (CV). The potential of one electrode is swept up and down relative to a known, standard potential while the current through that electrode is measured. As the bias is swept, electrochemically active species in the solution will be alternately oxidized and reduced, resulting in peaks when current is plotted against potential. The location of redox peaks will of course depend on the reactions taking place. For each reaction, there is a different voltage threshold for satisfying the free energy requirements. The best way to characterize a particular reaction in a particular system is to perform a CV scan. In the experiments, one of the most standard CV systems – the ferrocyanide/ferricyanide reaction – was tried first to ensure that the measurement setup was working properly. This system has well known redox peaks, which were successfully replicated in Figure 3.2.1a. From then, the central reaction for the system, the reduction of the gold cyanide complex anion to neutral gold and free cyanide, was characterized. This reaction requires the provision of an electron from the working electrode and results in the deposition of solid gold on the electrode surface, as neutral gold is not soluble in water. Due to diffusion effects, CV scans performed with microelectrodes frequently differ from CV scans on larger electrodes, so the reaction was characterized with both gold wire as the working electrode and using the microelectrodes from the device. Representative scans can be seen in Figure 3.2.1(b-c)
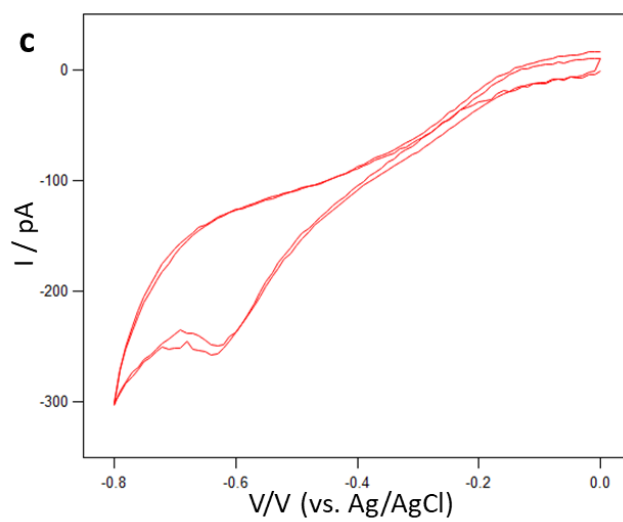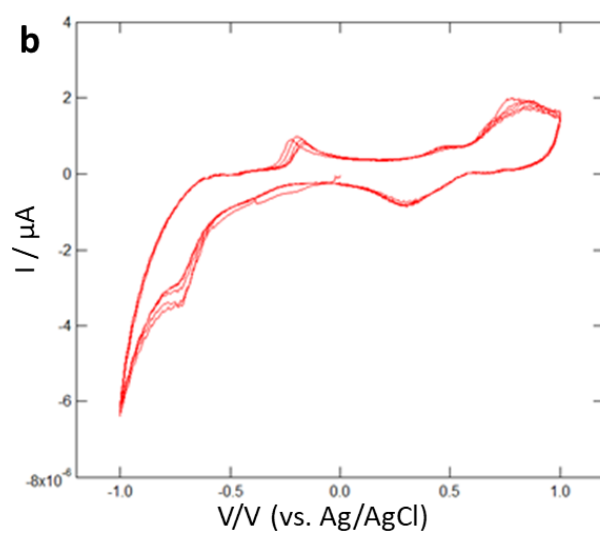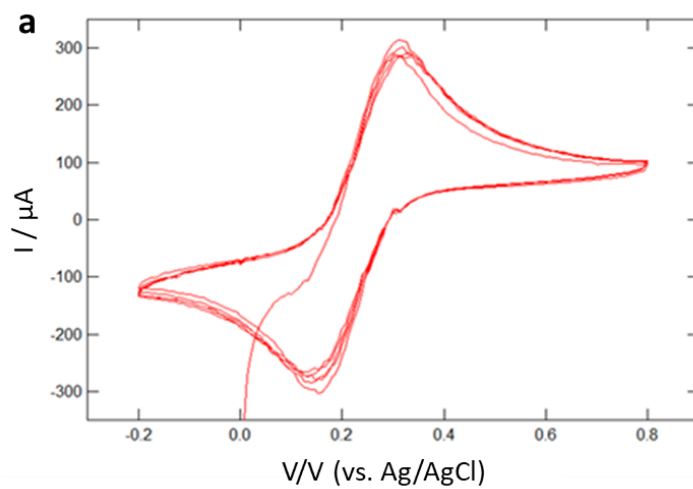
Figure 3.2.1. Cyclic Voltammetry Scans. (a) Scan of ferricyanide / ferrocyanide system. (b) Scan of gold cyanide / gold system with large electrodes. (c) Scan of gold cyanide / gold system with microelectrodes.

3.2.3   Electrochemical Deposition Circuit

To carry out the electrochemical deposition, a Keithley source-measurement unit (SMU) was used. This instrument can source and measure both current and voltage, but it was generally used it as a voltage source for these experiments. The instrument can be run in two-wire mode or four-wire mode. In two-wire mode, a potential difference is established between two terminals, labeled high and low, and the current flowing out of the high terminal is measured. In four-wire mode, the potential is established between an additional two terminals, labeled sense high and sense low. No current flows between sense high and sense low; rather, it flows from high to low as in two-wire mode. The two modes allow us to setup two kinds of electrochemical cells. The first kind is termed a three-electrode electrochemical cell, which is the standard for most electrochemical experiments. The three-electrode cell, as described in the above section, is composed of a working electrode, counter electrode, and reference electrode. The potential of the working electrode is controlled relative to the fixed reference electrode, through which no current should flow. The current is supplied by the counter electrode. For the deposition experiments, the microelectrode working electrode was attached to the low and sense low terminals. An Ag/AgCl reference electrode in 3M KCl was attached to the sense high terminal and a gold wire counter electrode to the high terminal (Figure 3.2.2a) The second kind is called a two-electrode cell, which is a simpler variant composed only of a

working electrode and a counter electrode which can be attached to the high and low

terminals. If a standard reference electrode (such as an NHE or Ag/AgCl) is used as the

counter electrode, one can approximate the behavior of a three-electrode setup, but the

reactions taking place at the counter electrode surface will change its potential. In this

research, a two-electrode cell with a pseudo-reference Ag/AgCl electrode was used for

most deposition activity due to the simpler setup and control of the system. Because of

the small currents being generated on the microelectrode, there is little change to the

surface potential of the pseudo-reference over the course of the experiment. To a rough

approximation, the current passed over the course of a typical deposition will change the

salt concentration around by a factor of only 10^{-8}. This setup can be seen in Figure
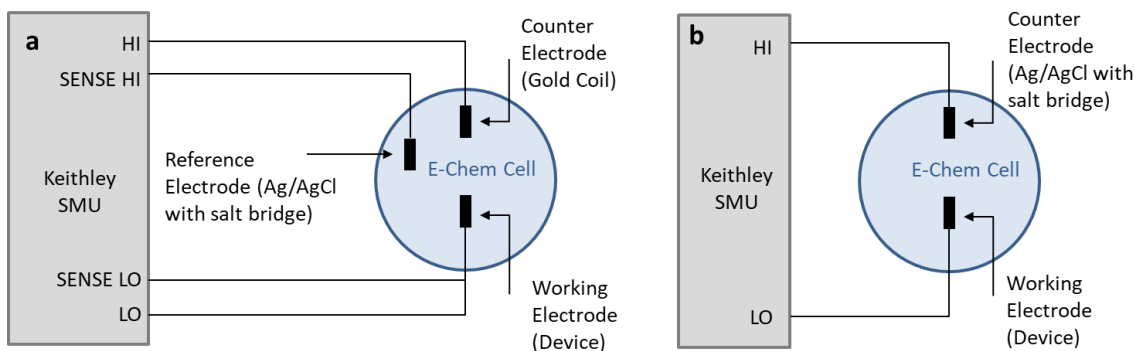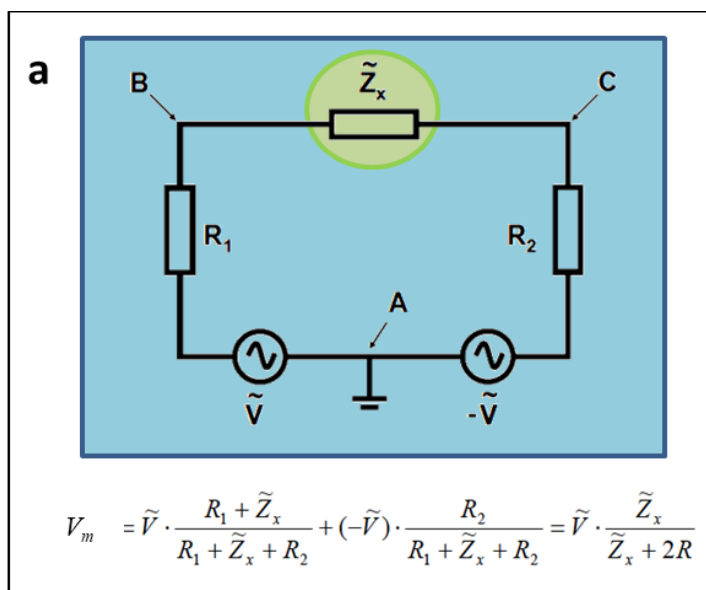
3.2.2b.

Figure 3.2.2. Electrochemical Circuits. (a) Three-electrode circuit. The bias is established between the working electrode and the reference electrode, but no current passes through the reference, which maintains a constant absolute potential. (b) Two-electrode circuit. Current passes through both electrodes, which can polarize the Ag/AgCl electrode if the current is large enough.

3.2.4   Deposition Control

The data from the gold cyanide CV scans allows us to carry out electrochemical deposition of gold in the nanochannel, but the creation of a usable device requires us to control that deposition. To do that, we need to acquire real-time data about the state of the gap between the two electrode tips. If we model the electrodes as wires and the gap as a variable resistor, we can see the beginnings of a measurement scheme. Placing a bias between the electrodes will allow us to determine the resistance between the tips by measuring the current. The resistance is, of course, infinite across the gap initially, but as the gap gets smaller, electron tunneling will eventually produce a current. This direct sensing method has been used in break-junction devices, but the current is detectable only to about 1 nm in gap distance. An improvement can be made if we consider the gap as having a capacitive component as well as a resistive component. If we add an AC component to our probing potential, we can construct a model circuit that allows us to indirectly measure the impedance across the gap. The model circuit is shown in Figure 3.2.3a. In previous work, a monitor circuit of this kind was shown to detect the closing of an unconfined electrode gap at distances of tens of nm. In the monitor circuit, a diagram of which is shown in Figure 3.2.3b, an AC potential of 2 mV is applied to each tip, typically at about 3 kHz, with the two tips 180° out of phase. The AC amplitude is small enough that it does not interfere with the deposition process. The signal is picked up by a lock-in amplifier, an instrument that will pick out signals of a target frequency from a more complex input. In this case, the lock-in removes any DC offset from the electrochemical circuit and reports the amplitude and phase of the AC component only. By comparing the recorded signal to the supplied signal, we can determine the impedance

66

based on the equation in Figure 3.2.3b. Figure 3.2.4 shows a validation of the monitor circuit using known resistors as the circuit load.

If we can deposit gold onto our electrodes, and we can electronically monitor the status of the electrodes in real time, then it is a fairly straightforward (which is not to say easy!) extension to use the monitoring data to control the deposition. Here a computerized feedback system for deposition control has been implemented. Raw impedance data is collected at 20 kHz. Every 200 ms, the program averages the monitor data from the previous cycle and compares it to pre-programmed threshold values. Based on those values, the potential of the electrode tips relative to the reference is altered for the next cycle. This potential can be chosen to be in a reducing regime, an oxidizing regime, or a neutral regime. Because the feedback response rate is limited to 5 Hz, finer control can be implemented by delivering reducing or oxidizing pulses of varying duration over a neutral background potential. The interaction between the electrochemical circuit and the monitor circuit is shown in Figure 3.2.3c.
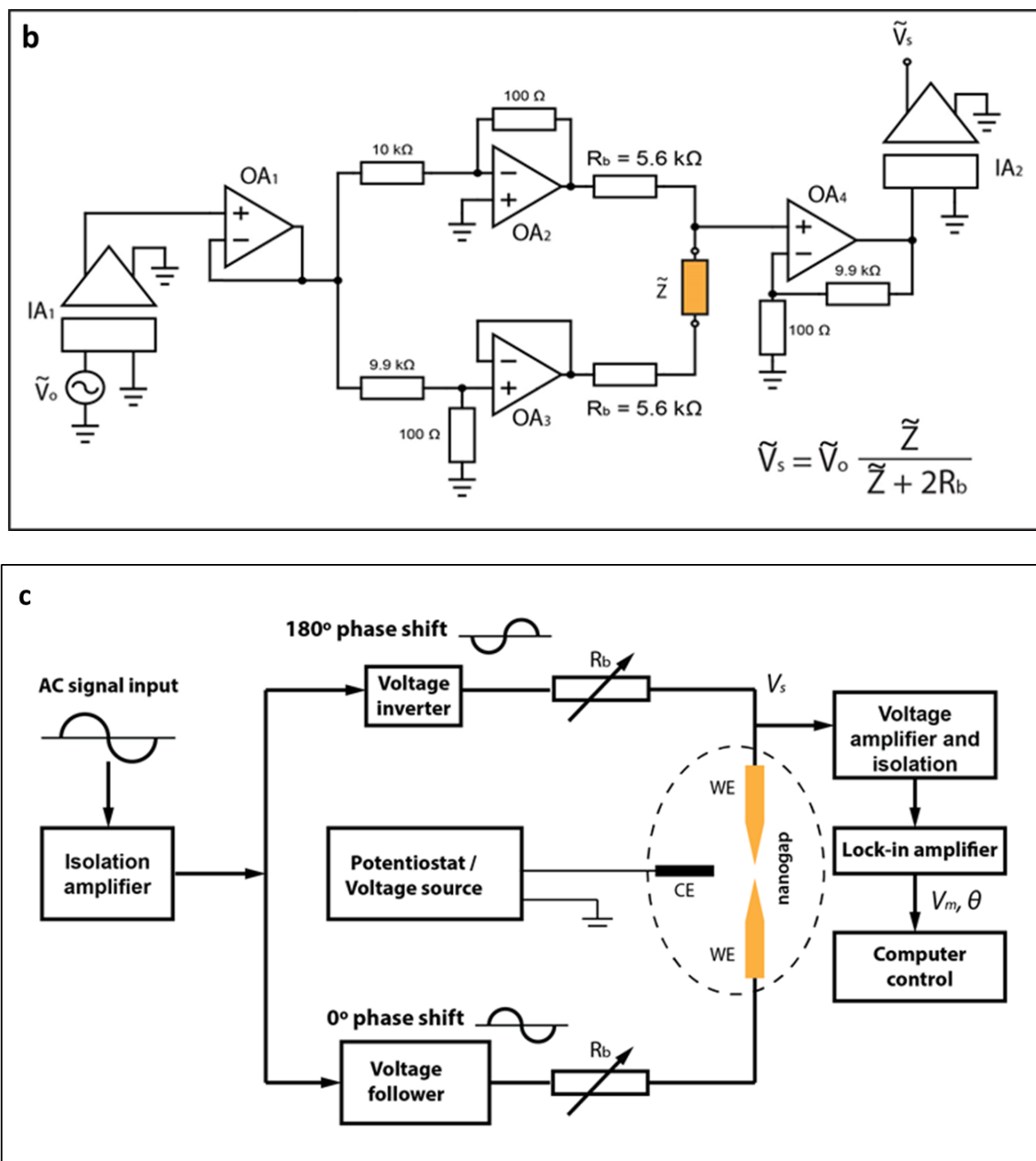

$$V_m = \tilde{V} \cdot \frac{R_1 + \tilde{Z}_x}{R_1 + \tilde{Z}_x + R_2} + (-\tilde{V}) \cdot \frac{R_2}{R_1 + \tilde{Z}_x + R_2} = \tilde{V} \cdot \frac{\tilde{Z}_x}{\tilde{Z}_x + 2R}$$

Figure 3.2.3. Impedance Monitor Circuit. (a) Equivalent AC circuit for impedance measurement. $\tilde{V}$ and $-\tilde{V}$ are 180° phase-shifted AC voltage sources. Z_x is the impedance between the electrode tips. The output voltage V_m is measured between points A and C. Resistors R_1 and R_2 are set equal to each other and can be tuned to optimize the sensitivity of the measurement. (b) Actual circuit used, with isolation and reduction/amplification[59]. (c) Integration between the electrochemical deposition circuit and the monitor circuit. The electrode tips simultaneously take the role of the working electrode in the electrochemical circuit and the unknown impedance in the monitor circuit. A computer program alters the cell potential of the electrochemical circuit based on the impedance value read from the monitor circuit.
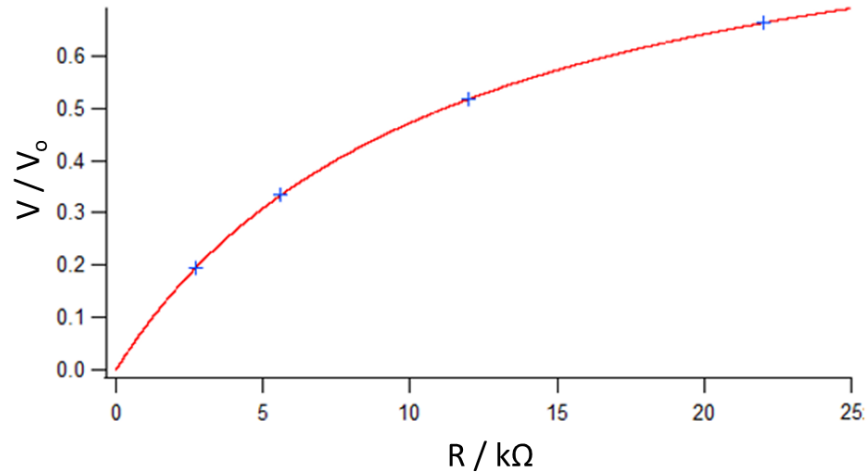
68

Figure 3.2.4. Validation of Impedance Monitor Circuit Using Known Resistors. Crosses represent output values of known resistances, while curve is predicted output.

3.3   Initial Fabrication of Devices

Fabrication of each device begins with the placement of alignment markers (typically Cr/Au 2/30 nm) on a glass substrate coated with 200 nm silicon nitride. Standard semiconductor fabrication processes (photo- or electron-beam lithography, thermal or electron-beam evaporation, and lift-off) are used to create the markers and all subsequent metal layers. In the most representative process, photolithography exposure is performed with a GCA 8500 projection aligner, which allows successive layers to be aligned to the base layer with a positional error of about 700 nm.

After the alignment marks are deposited, an inner sacrificial layer of 10-20 nm Cr is deposited. This layer will define the location and dimensions of the central fluid channel, and it fixes the height of the nanopore.

69

After the inner sacrificial layer is complete, an outer sacrificial layer made of Al metal is constructed in two regions overlapping each end of the inner sacrificial layer. This layer defines a channel of intermediate height between the bulk fluid channel and the central channel around the nanopore. The outer sacrificial layer is typically 100-200 nm thick, allowing for efficient capture of analyte molecules from the bulk channel. In addition, the cross-sectional area tapers to enable an electric field gradient which assists in the unwinding of long analytes. To help prevent collapse of the fluid channel, the outer sacrificial layer is not placed directly on the chip surface. Rather, reactive ion etching (RIE) is used to etch a trench in the chip, with the deposited metal filling up the trench to just past the original surface.

After the outer sacrificial layer is complete, initial gold electrodes are deposited. They overlap with the sides of the inner sacrificial layer and feature an initial electrode gap of 1 μm. Each electrode terminates in a wide contact pad that can be used to connect to external electronics.

Once all of the metal structures have been fabricated, the chip is sealed in a layer of 50-100 nm hafnium oxide deposited by atomic layer deposition (ALD). ALD is a subclass of chemical vapor deposition (CVD) which results in high-density conformal films. The sealing step is critical to ensure that there are no unwanted leakage paths between the *cis* and *trans* fluid channels; the only path should be directly through the central nanochannel/nanopore structure.

After sealing, the fluid channels are constructed. The first step is another RIE etch to cut through the HfO_2 passivation in the regions where the bulk fluid channels overlap with the outer sacrificial layers. This will allow fluid access for the later etching

70

of the sacrificial layers. Next, the walls of the bulk fluid channel are constructed using

25-50 µm SU-8. SU-8 is a photosensitive polymer that cross-links when exposed to UV

light. By using photolithography, SU-8 can be directly patterned into a variety of useful

and highly chemically resistant structures. Here, SU-8 forms the side walls of the bulk

fluid channels and also provides an additional layer of passivation for the nanochannel.

The ceiling of the channels is formed from a flat slab of PDMS, a curable polymer with

wide applications in microfluidic systems. Prior to being attached to the chip, holes are

punched through the PDMS to allow fluid access. At this point, the chip is then attached

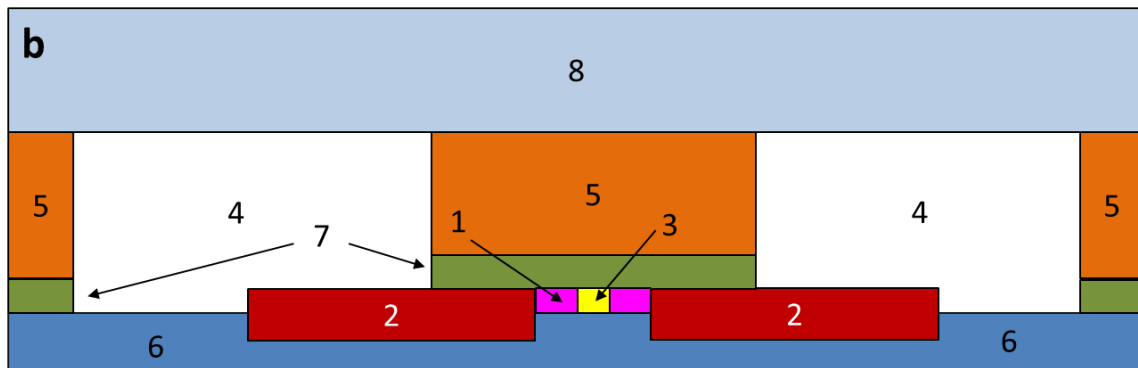to a printed circuit board (PCB) by ultrasonic wire bonding.
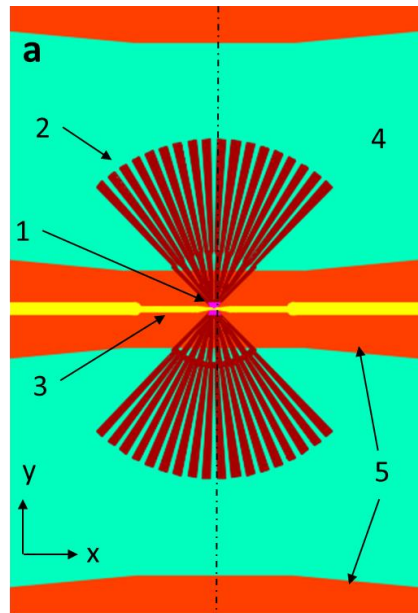
Figure 3.3.1. Complete Initial Device Structure. (a) Top view of structure showing (1) inner sacrificial layer, (2) outer sacrificial layer, (3) electrode tips, (4) bulk fluid chambers, and (5) fluid chamber walls. Dashed line shows cross-section view for (b). (b) Cross-section view of structure showing (1) inner sacrificial layer, (2) outer sacrificial layer, (3) electrode tips, (4) bulk fluid chambers, (5) fluid chamber walls, (6) substrate, (7) passivation, and (8) PDMS chamber ceiling.
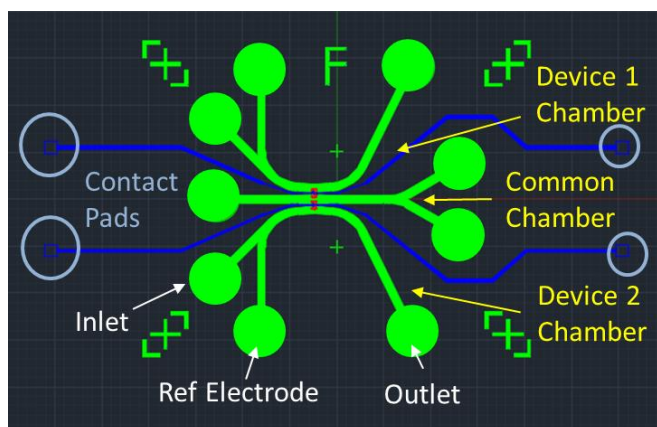

Figure 3.3.2. Layout of Nanopore Chip. Each chip contains two devices. Each device has a dedicated fluid chamber (generally the *cis* chamber for an experiment), which contains inlet and outlet ports for fluid exchange and a third port that can be used to connect a reference electrode. There is also a common chamber (generally the *trans* chamber for an experiment) that connects to both devices. Each device has contact pads for each gate electrode.
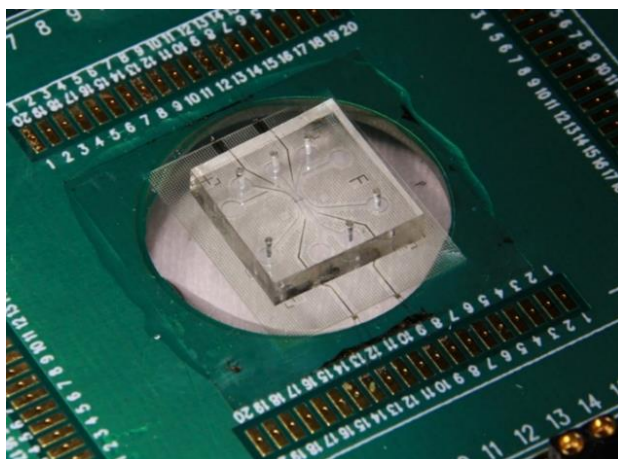
Figure 3.3.3. Nanopore Chip Assembly. This picture shows a chip mounted on a PCB board with the PDMS chamber on top. Access ports can be seen punched into the PDMS. Picture taken by Yuan Wang.

Once the bulk fluid channels are complete, the sacrificial layers can be etched to form the nanochannels. First, the outer sacrificial layers are etched. Aluminum etchant is introduced through the bulk channels where it comes into contact with the surface of the outer sacrificial layer. The metal in the region where the sacrificial layer overlaps the bulk fluid channel is quickly removed, and then the etching must proceed laterally underneath the HfO_2 passivation layer. This process is much more lengthy given the larger distances involved. The etch rate for Al is on the order of 1 nm/s, and the distance from the edge of the bulk channel to the inner sacrificial layer is about 30 µm, so the etch process can take several hours. After the outer sacrificial layer is completely etched, the Al etchant is replaced with pure water, followed by the introduction of Cr etchant to remove the inner sacrificial layer. After the inner sacrificial layer is removed, the nanopore device is ready for final preparation via electrochemical deposition.
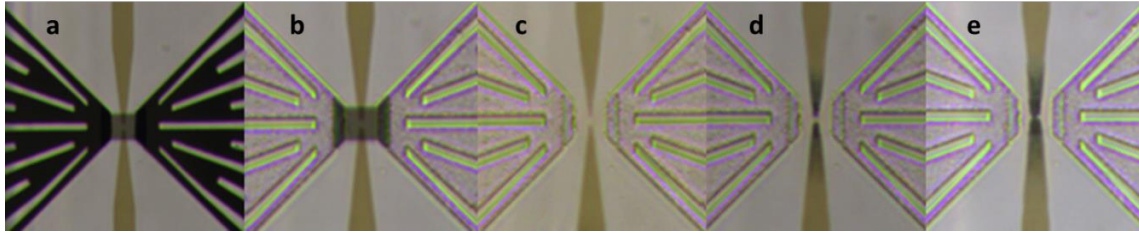
Figure 3.3.4. Sacrificial Layer Etching and Electrochemical Deposition. (a) Device center after initial fabrication. (b) After etching of the outer sacrificial layer. (c) After etching of the inner sacrificial layer. (d) During the electrochemical deposition process. (e) After the completion of electrochemical deposition.

3.4   Device Characterization

Before beginning experiments, a variety of tests were performed to validate both the initial fabrication procedures and the electrochemical deposition. This helps to ensure that the device as fabricated is consistent with the device as designed.

3.4.1   Initial Electrode Fabrication

Because the electrode tips are the foundation of the nanopore structure, considerable effort was spent ensuring that they could be reliably fabricated with the necessary dimensions. Initial fabrication efforts were centered on electron beam lithography (EBL), a direct-writing lithography technique that can create patterns at the sub-100 nm scale. These efforts resulted in sharp, closely-separated electrodes with a tip width of 50 nm and an initial gap of 100 nm. While the dimensions are very good for initial electrodes, a decision was made to switch from EBL to photolithography for the initial electrodes on practical grounds. After moving fabrication from silicon wafers to glass slides, several issues arose. First, using an insulating substrate decreases the resolution of EBL patterns because charging of the substrate distorts the electron beam. The use of a charge dissipation layer can mitigate the effect, but resolution still suffers

74

compared to a conducting substrate. The best tip sharpness and spacing that was

achieved on glass was about twice the dimensions of the same features on silicon, about

100 nm and 200 nm, respectively. Second, the use of an insulating substrate increased

the likelihood of damaging electrostatic discharges between the electrode tips, and

increasing the distance between the tips lowers the risk. Photolithography at ASU can

produce an electrode gap of 1 µm and is a much faster process than EBL, which allows

us to conduct tests and experiments more frequently. In the future, the potential for

sharper tips and smaller initial gaps may make it worth exploring whether EBL can be

effectively re-integrated into the fabrication process. For now, photolithography is able

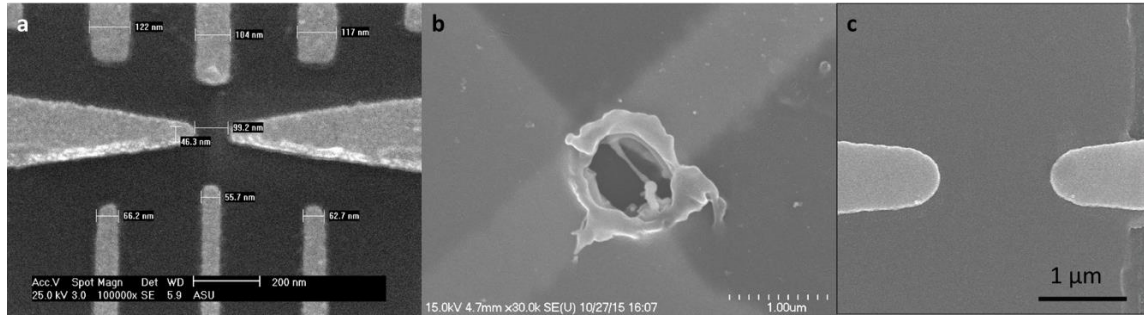to efficiently produce initial electrode tips that meet our requirements.

Figure 3.4.1. Initial Electrode Tips. (a) Electrode tips fabricated using electron beam lithography. Distance between tips is 100 nm. (b) Static damage on insulating substrate. (c) Electrode tips fabricated using photolithography[59]. Distance between tips is 1 µm.

3.4.2 Layer Structure of the Nanochannel

Because the nanochannel plays such an important role in the overall device, it was

important to verify that the thickness of the layers was consistent with the design. Here a

focused ion beam (FIB) tool was used to cut a cross-section slice out of a device which

75

could then be imaged with a transmission electron microscope (TEM). The device shown in Figure 3.4.2 varies in two ways from the current design. First, the passivation layer is 270 nm of SiO_2 deposited by remote plasma chemical vapor deposition (RPCVD) instead of the current 50 nm of HfO_2 deposited by ALD. Second, the electrode tips (here 33 nm thick) were deposited as a separate layer from the rest of the electrode lines (here 70 nm thick).
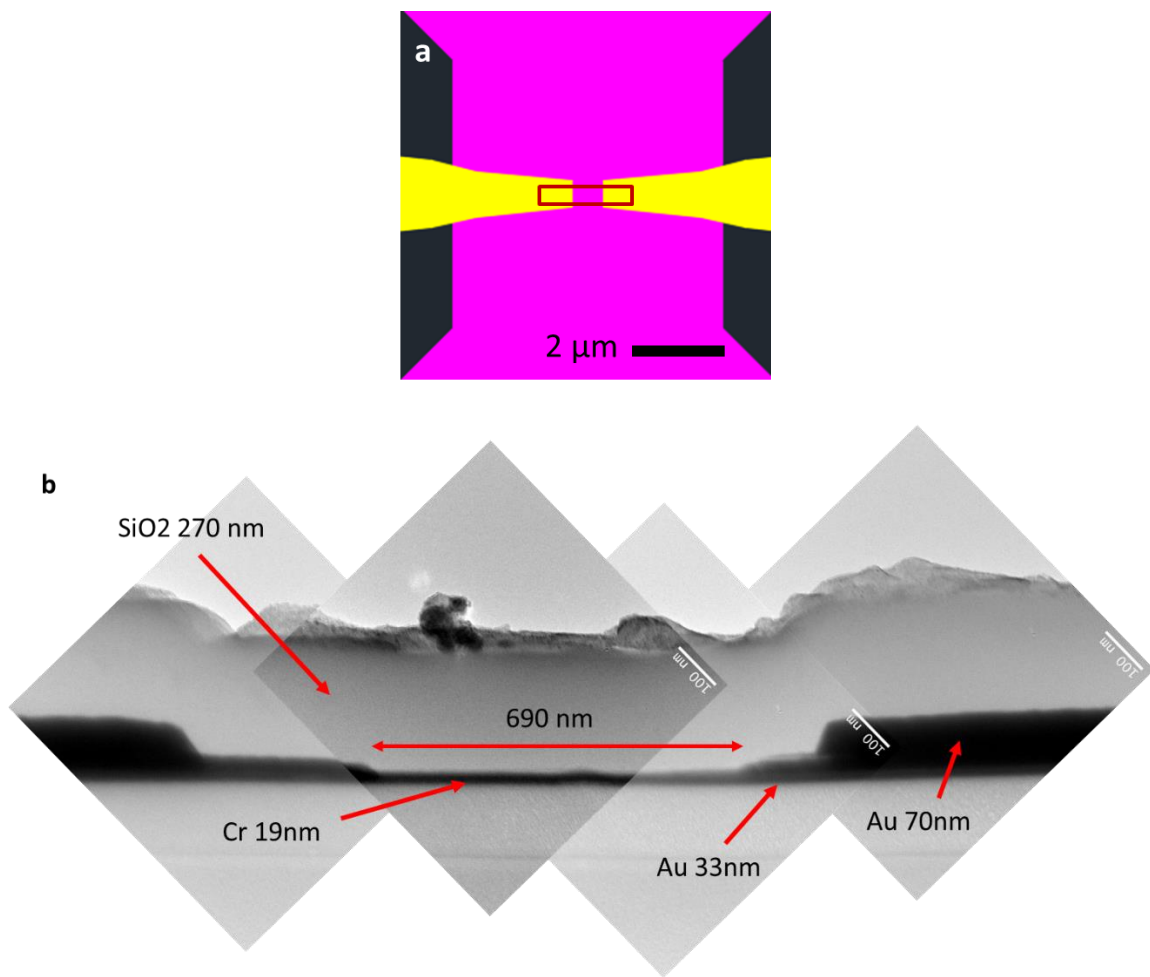

Figure 3.4.2. Device Cross-Section Before Sacrificial Layer Etching. (a) Top view of structure. Red rectangle shows area where cross-section slice was removed by FIB tool. (b) TEM of cross-section slice. Cr sacrificial layer is at center with electrode tips on

76

either side. The entire structure is sealed with a SiO_2 passivation layer.   TEM image taken by Yuan Wang.

3.4.3   Electrode gap after Electrochemical Deposition

Evaluating the electrode gap after electrochemical deposition is essential for

accurately calibrating the deposition feedback system. It is an area where it has to this

point proven very difficult to get data that is both high-resolution enough to accurately

characterize gaps below 10 nm in size and also representative of full experimental

conditions. The simplest way to image the gap is by top-down SEM. This is relatively

straightforward if the electrodes are unconfined in the z-direction. The charging

problems associated with imaging on an insulating substrate can be mostly solved with a

thin sputter coating of gold over the surface, a standard practice in preparing non-metallic

samples for SEM. In Figure 3.4.3(a-b), we see an example of an unconfined nanogap.

The resolution of the image approaches 1 nm, and a gap of 10 nm can be seen. When the

sample is tilted, it can be seen that the final height of the electrode tips is some hundreds

of nanometers due to the isotropic deposition of gold on the electrode surface. Despite

the high quality of the image, the structure is not representative of what we would see for

a deposition confined within a nanochannel. Figure 3.4.3c shows an SEM after

deposition in a confined channel. This image conveys valuable information but also

contains significant limitations. We can immediately see the contrast between the bright

initial electrode tips and the darker electrodeposited metal. Since both the initial and

electrodeposited tips are made of gold, the contrast difference reflects the different

thickness of each layer. The deposited gold is clearly thinner than the 60-nm thick initial

electrodes, despite its lateral growth of about 500 nm. This is a clear demonstration of

77

the success of the passivation layer in confining the new gold in the sacrificial-layer

channel. Unfortunately, the same passivation layer interferes with the imaging of the

metal structures underneath. Resolution is significantly limited such that we can only

estimate the size of the gap as being around 20 nm. In order to get higher-resolution

imagery, we need to be able to remove the passivation layer without disrupting the

underlying gold structure. Either wet etching or RIE could possibly be used, but a

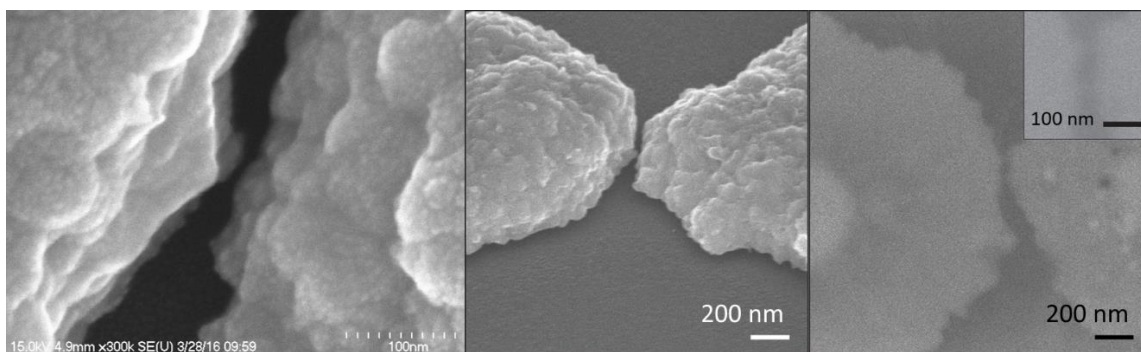systematic effort has not yet been made.

Figure 3.4.3. SEM of Electrode Tips After Electrochemical Deposition[59]. (a) Overhead view after electrochemical deposition without confinement in the z-direction. Gap between electrodes is 10 nm at closest approach. (b) Tilted view of electrode pair from (a). Isotropic deposition results in electrode height of hundreds of nanometers. (c) Overhead view of electrode pair after electrochemical deposition in a 10-nm confined nanochannel. Despite lateral growth of about 500 nm, the deposited gold shows a clear contrast – indicating a thinner layer – with the initial 60-nm thick electrodes. Inset is a close-up showing a roughly 20-nm gap.

3.4.4   *Electrochemical Deposition Feedback Signals*

The counterpart to obtaining direct imaging of the electrode gap is analyzing the

impedance data output from the electrochemical deposition control circuit. Several key

pieces of data are presented in Figure 3.4.4. Figure 3.4.4a shows the achievement of

repeatedly opening and closing a single pore. This demonstrates that the deposition

reaction is fully reversible, and it opens several strategies for controlling the final state of the pore. The simplest strategy is to stop deposition when the impedance drops past a defined threshold. Other strategies could involve fully closing, and then reopening the pore, or cycling between closed and open configurations several times, which may stabilize the pore geometry. Figure 3.4.4b shows the conductance between electrode tips at the end of a deposition in which contact between the tips was made. The measured conductance tends to jump between multiples of 77 µS, the two-channel quantum conductance. These "quantum steps" show the presence of low-integer atomic contacts between the two electrodes. Figure 3.4.4(c-f) show the different behavior of the system when contact between the electrodes is made and broken. Figure 3.4.4c and 3.4.4e show the conductance during connection. In each case, a single point contact is made first. The conductance stays around G_o for a time before rapidly increasing. Figure 3.4.4d and 3.4.4f show the conductance during disconnection. Here, the conductance decreases slowly to about $3G_o$ before suddenly dropping below the quantum conductance. In Figure 3.4.4 (b-f), the oxidizing or reducing potential is applied to the electrode as a series of pulses rather than as a constant potential, as seen in the bottom portion of each graph. By limiting the amount of time spent in an oxidizing or reducing state during each evaluation cycle, the control program can exercise finer control over the deposition process.
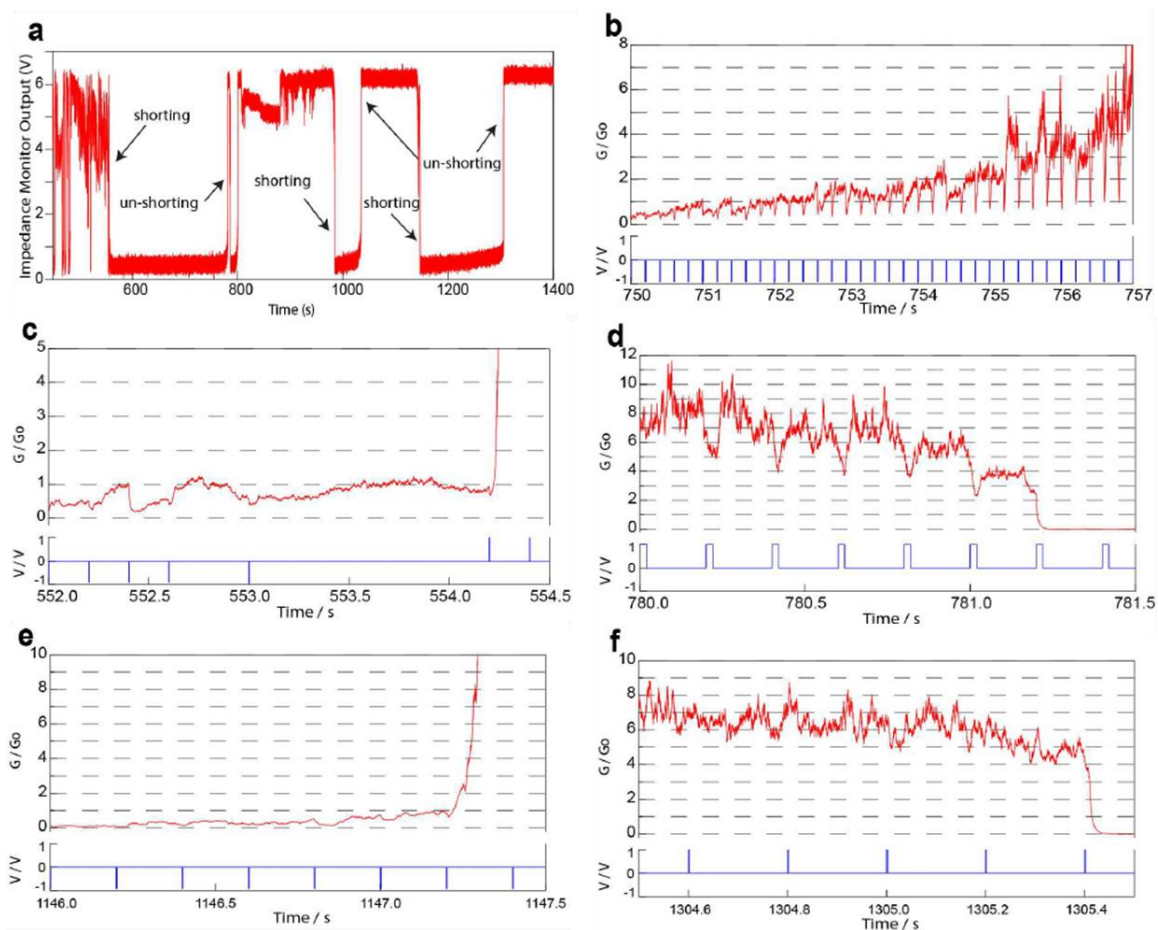
Figure 3.4.4. Feedback Signals from Deposition Control Circuit. (a) Raw data from impedance monitor circuit showing shorting/un-shorting events. When the gap distance is large, an open circuit voltage (here about 6 V) is measured. When the gap is fully shorted, a short-circuit voltage (here about 0.5 V) depending on the total device resistance is measured. (b) Top: Gap conductance during shorting event. As the gap closes, the conductance rises until it reaches the quantum conductance G_o. Afterwards, the conductance jumps between multiples of G_o. Downward spikes may be caused by changes to the electric double layer induced by the reducing pulses. Bottom: Potential of working electrode vs. counter electrode. (c)-(d) Back-to-back shorting and un-shorting events on a single electrode pair, respectively. (c) shows the conductance dwelling around G_o before rapidly increasing, while (d) shows the conductance decreasing to around 3 G_o before dropping abruptly toward zero. (e)-(f) Another pair of shorting and unshorting events on the same electrode pair as (c) and (d), showing the same essential characteristics.

3.4.5 Ion Conductance

It is also possible to track the ion current flowing through the nanochannel. This can be tracked during deposition in parallel with the impedance monitor circuit output to track deposition progress. The ion current is sensitive at much larger distances than the impedance monitor circuit, as it largely depends on the cross-sectional area of the channel. It also decreases more rapidly toward the end of the deposition, which may reflect surface charge gating by the electrodes as the channel closes.
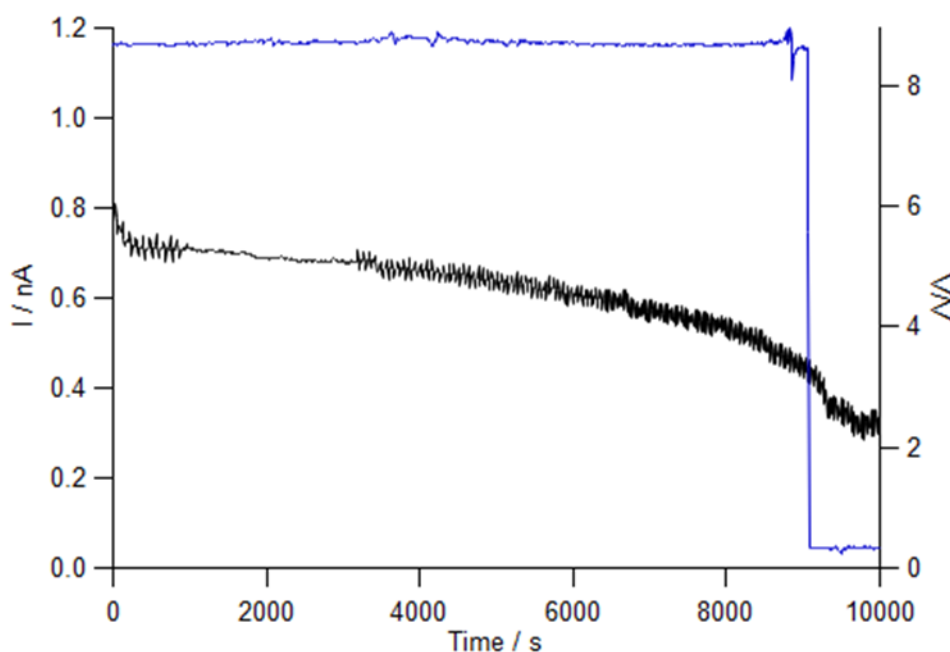

Figure 3.4.5. Ion Current Tracking. The black line shows the ion current over time during electrochemical deposition as the channel is closed (left axis). The blue line shows the output from the impedance monitor circuit (right axis). The electrodes make contact at t = 9060. Experiment jointly conducted with Yuan Wang.

3.5   Translocation and Control Experiments

3.5.1   Dye Translocation

The first experiment was a demonstration of the ability to use fluorescent dyes to track activity in the fluid channels and to drive charged species through the nanochannel.

81

The first step was etching the sacrificial layers of a device to form a nanochannel, but electrochemical deposition was not used in this case to narrow the electrode gap. Sytox Orange dye in 10 mM TE buffer at pH 8.0 was added to the fluid chamber on the *cis* end of the device, with TE buffer in the bulk channel on the *trans* end. This setup allows dye to diffuse from one side of the nanochannel structure (inclusive of both intermediate channels and the central channel) to the other. At this point, recording of the fluorescent intensity in the nanochannel structure began. After 9.5 minutes, a potential bias of -20 V was applied to the *trans* chamber. Because Sytox Orange has a positive charge in solution, it is driven through the nanochannel structure into the *trans* chamber. At 14.5 minutes, the potential bias was reversed to +20 V to drive the dye back into the *cis* chamber. The results of the experiment are summarized in Figure 3.5.1. A key finding (Figure 3.5.1b) is that fluorescent intensity decreases along the channel length for all observed times. This is consistent with a concentration gradient of dye between the *cis* chamber and the *trans* chamber. The presence of dye in the *trans* intermediate channel also shows that the 10-nm central nanochannel is open. The other main finding (Figure 3.5.1c) is that intensity increases for all locations from the time that the bias is switched on, then decreases when the bias is reversed. This shows that it is possible to use an applied bias to drive charged species through the nanochannel, a key requirement for controlled DNA translocation.
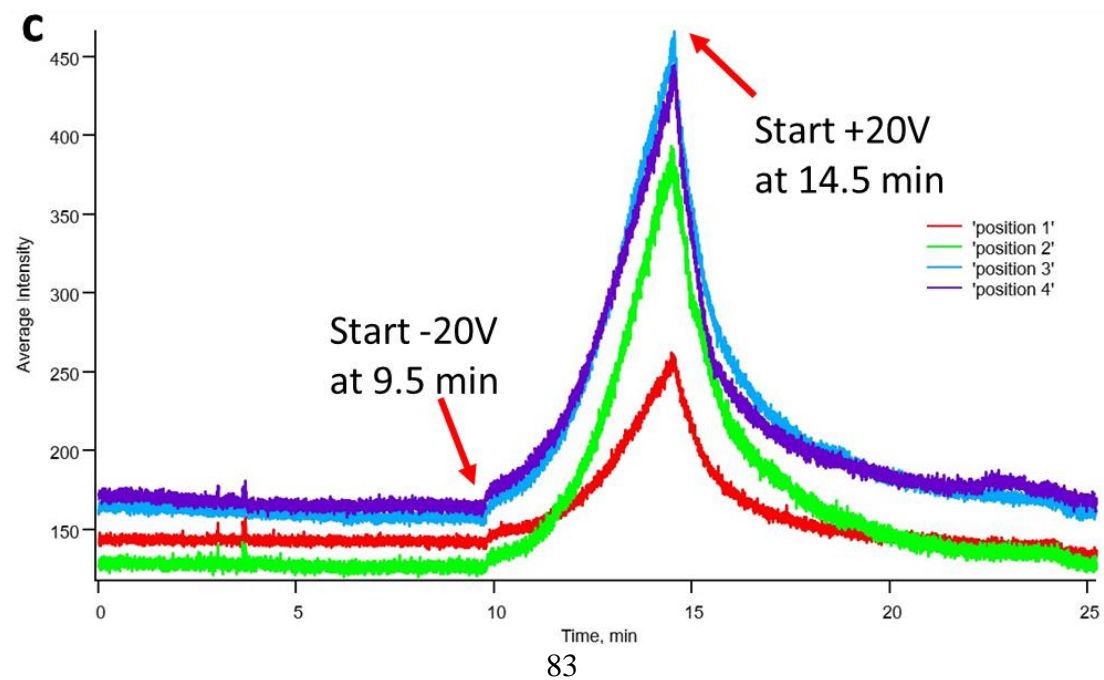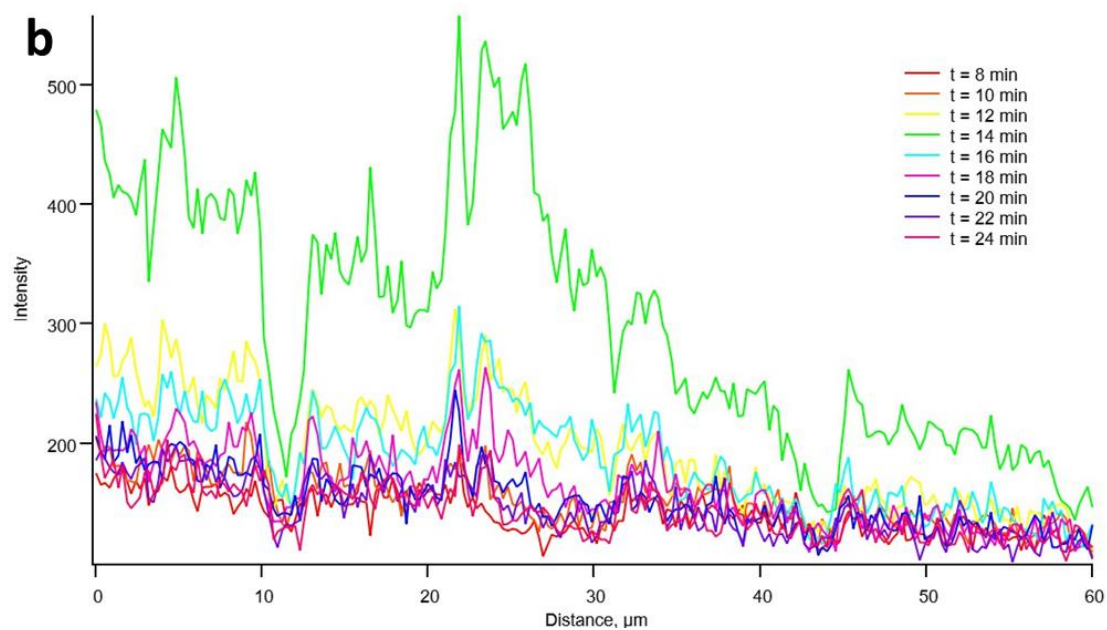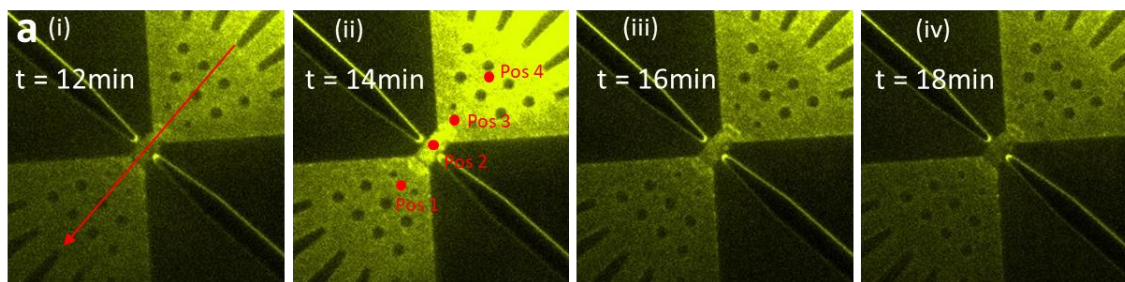
Figure 3.5.1. Translocation of Fluorescent Dye. Dye is introduced into the bulk channel on one side of the nanochannel. At t = 9.5 minutes a 20 V potential is applied to drive the dye through the nanochannel. At t = 14.5, the direction of the potential is reversed (a) Time-delayed images of the central and intermediate channel structures. The red arrow in (i) shows the direction of dye movement and is the line for the intensity profiles in (b). The dots in (ii) mark the positions for the intensity profiles in (c). (b) Fluorescent intensity along the line marked in (a)(i) for different times. Intensity decreases with distance, showing the diffusion of dye into the channel. The dips at 12 µm and 43 µm occur where the line crosses support structures for the channel. (c) Fluorescent intensity over time at the positions marked in (a)(ii). Intensity increases when the voltage is turned on, then decreases when the polarity is reversed. Experiment jointly conducted with Yuan Wang.

3.5.2   DNA Capture, Trapping, and Translocation

The next experiment was attempting to use a bias to translocate DNA through the nanochannel and observe the translocation with fluorescent markers. For this experiment, double-stranded lambda DNA was used, which has a length of 48 kilobases. The DNA was dyed with Sytox Orange, which is an intercalating nucleic acid dye which attaches itself between successive base pairs. Following the protocol of the pure dye translocation, the sacrificial layers were etched but the initial nanogap was not closed in order to create the most favorable environment for translocation. DNA in TE buffer (pH 8.0) was added to the *cis* chamber while TE buffer was added to the *trans* chamber. To drive the negatively charged DNA through the nanochannel, a positive bias was applied to the *trans* chamber. Experimental setup is shown in Figure 3.5.2.
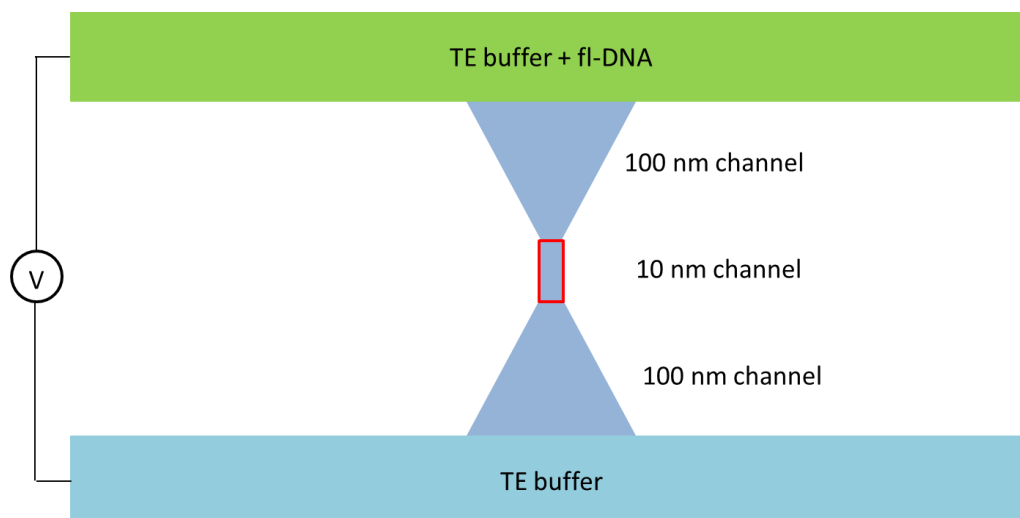
Figure 3.5.2. Schematic of First DNA Translocation Experiment. The *cis* chamber is filled with TE buffer containing lambda DNA dyed with Sytox Orange. The *trans* chamber is filled with TE buffer only. A positive bias is applied to the *trans* chamber in order to drive the negatively-charged DNA through the channel.

When the bias was turned on, DNA molecules were observed moving from the bulk chamber toward the boundary of the intermediate channel. The DNA did not typically move immediately into the channel, but rather moved along the curved surface of the channel boundary, collecting where the boundary intersects with the channel wall (see Figure 3.5.2a). From here, individual DNA molecules would at times enter the intermediate channel. This behavior can be explained by the geometry of the channel. In the bulk chamber, the DNA is free to coil up, with a persistence length of about 50 nm. The channel is narrow enough that the DNA must substantially unwind in order to fit inside (see Figure 3.5.2b). The loss of entropy in unwinding represents a free energy cost for entering the nanochannel. Once inside the intermediate channel, DNA was not observed moving through the central nanochannel during this experiment. Rather, a DNA molecule would move partway through the intermediate channel before eventually stopping. Over the course of about a minute, the fluorescent intensity from the molecule

would fade away. I interpret the stopping of the DNA as reflecting the partial collapse of

the channel ceiling. When a DNA molecule first entered the intermediate channel, it

would preferentially travel along the channel wall rather than in the middle of the

channel. This suggests that the height of the channel was greatest at the edge, where

there was a solid support. The fading of the fluorescence signal may be due to

photobleaching or the dye molecules washing off the DNA. The individual dye

molecules are positively charged, and the electric field in the channel would exert a force

in the opposite direction of that on the DNA. This force would be greatest in the central

nanochannel and possibly render us unable to detect any translocation events.
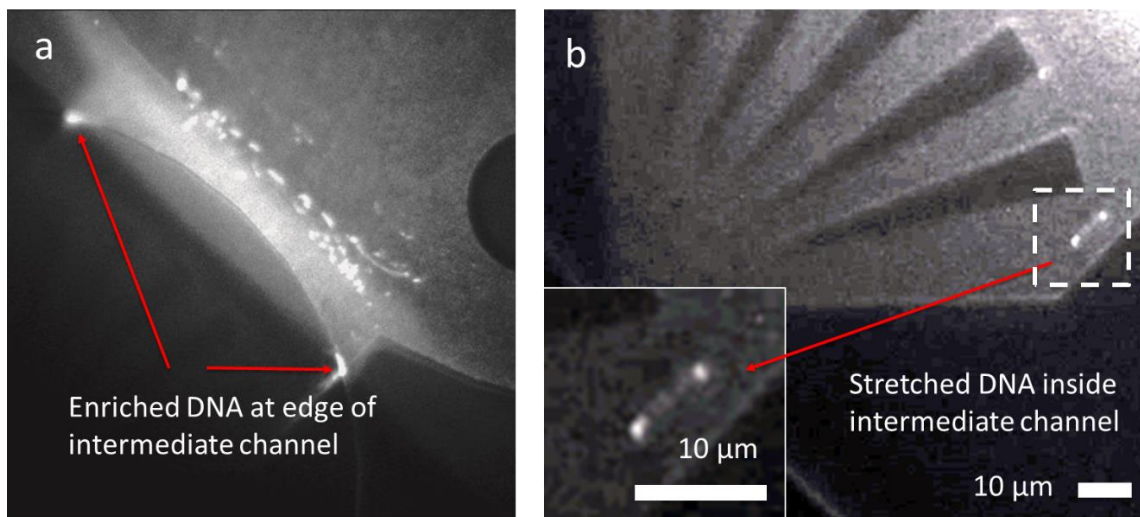
Figure 3.5.3. DNA Capture. (a) In the bulk, DNA motion is dominated by diffusion. Near the edge of the intermediate channel, the electric field becomes strong enough to significantly attract the DNA. There is an energy penalty for the DNA to unwind and enter the height-constricted channel, so DNA clusters near the edge. (b) Inside the intermediate channel, double-stranded DNA is forced to unwind. Experiment jointly conducted with Yuan Wang.

A follow-up experiment took advantage of the differing charges of the DNA and

the dye. In this experiment, one chamber was filled with unlabeled DNA in TE buffer.

The other chamber was filled with Sytox Orange in TE buffer. The application of a

positive bias to the dye chamber would therefore drive both the DNA and the dye into the

channel structure from their respective chambers. In this way, a DNA molecule that

translocated the nanochannel would be likely to encounter dye molecules on the other

side and be stained. Indeed, after the application of the bias, several bright spots were

observed that were likely translocated DNA molecules.
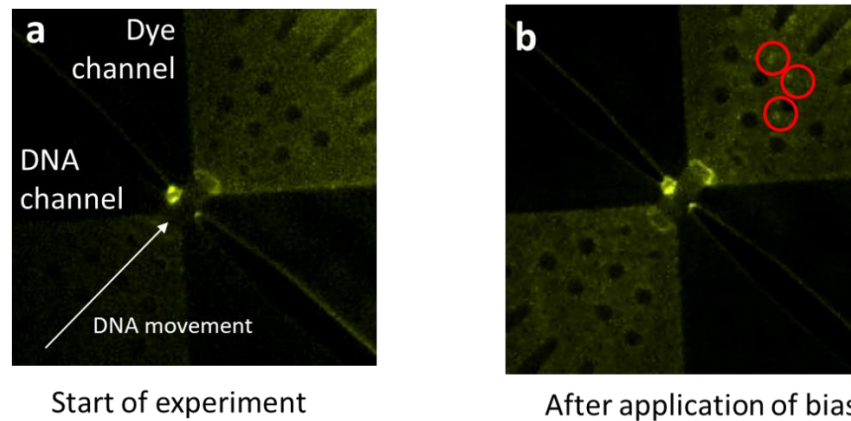
Figure 3.5.4. DNA Translocation. (a) Initial setup of experiment. Unlabeled DNA
was introduced to the bottom left chamber, while Sytox Orange was introduced to the
upper right chamber. The application of a positive bias to the upper right chamber drives
both DNA and dye through the nanochannel. (b) After application of the bias, bright
patches were observed in the dye channel consistent with the appearance of DNA
molecules having translocated the nanochannel. Experiment jointly conducted with Yuan
Wang.

3.5.3   Gating of Ionic Current

One of the features of having electrodes integrated into the nanopore structure is

the ability to use them to affect the translocation speed of DNA through the pore. Since

DNA is charged, the application of an electric potential to the gap electrodes can modulate DNA motion through the nanopore. Interactions with the pore wall can slow, and possibly stop, the motion of DNA through the pore[80-84]. If the electric double layers of the pore wall and DNA molecule overlap, the DNA molecule will experience an electrostatic force from the pore wall. If the pore wall is positive, the negatively charged DNA will be attracted. As a DNA molecule approaches the pore, its translocation speed will first be increased by the attractive force from the wall. Once it passes the midpoint of the pore, the attractive force will reduce translocation speed by pulling the DNA back toward the pore. If the gate potential is high compared to the through-pore bias driving the translocation, the DNA molecule can be trapped[80]. By modulating the strength of the gate potential, DNA could be stepped through the nanopore. As a first demonstration of this capability, the electrodes were used to alter the ionic current flowing through the channel, creating an ionic field-effect transistor (FET)[85-89]. In a solid-state FET, a gate electrode is situated between a source electrode and drain electrode connected by a semiconducting material. The electric field generated by the gate electrode can either enhance or suppress the conducting channel between source and drain. In the device, the gap electrodes can generate an electric field in their vicinity, but the range of the field depends on the Debye length of the solution, the length at which the electric potential drops by a factor of 1/e. The Debye length can be calculated by the formula

$$\lambda_D = \sqrt{\frac{\varepsilon_r \varepsilon_o k_B T}{2 \times 10^3 N_A e^2 I}}$$

where ε_r is the dielectric constant, ε_o is the permittivity of free space, k_B is the Boltzmann constant, T is the temperature in Kelvins, N_A is Avogadro's number, e is the elementary

charge, and *I* is the ionic strength of the electrolyte in mol/L. For a 100 mM solution of KCl, λ_D is approximately 1 nm, while for the gold deposition solution we use (87 mM KAu(CN)$_2$ and 186 mM K$_3$C$_3$H$_5$O(COO)$_3$), λ_D is 2.8 Å. Because of this, the strength of the gating effect will be much greater when the channel is constricted by the electrochemical deposition than in its initial open state. To confirm, the ionic current through the channel under a channel bias of 100 mV was measured for various gate potentials and for different states of the channel – before and after electrochemical deposition. The results are shown in Figure 3.5.5. When the channel is open, the current drops by 5% under a 120 mV gate bias (60 mV relative to ground applied to one gate electrode and -60 mV applied to the other). When the channel is closed, the current drops by 17% under a 120 mV gate bias and 27% under a 200 mV gate bias.
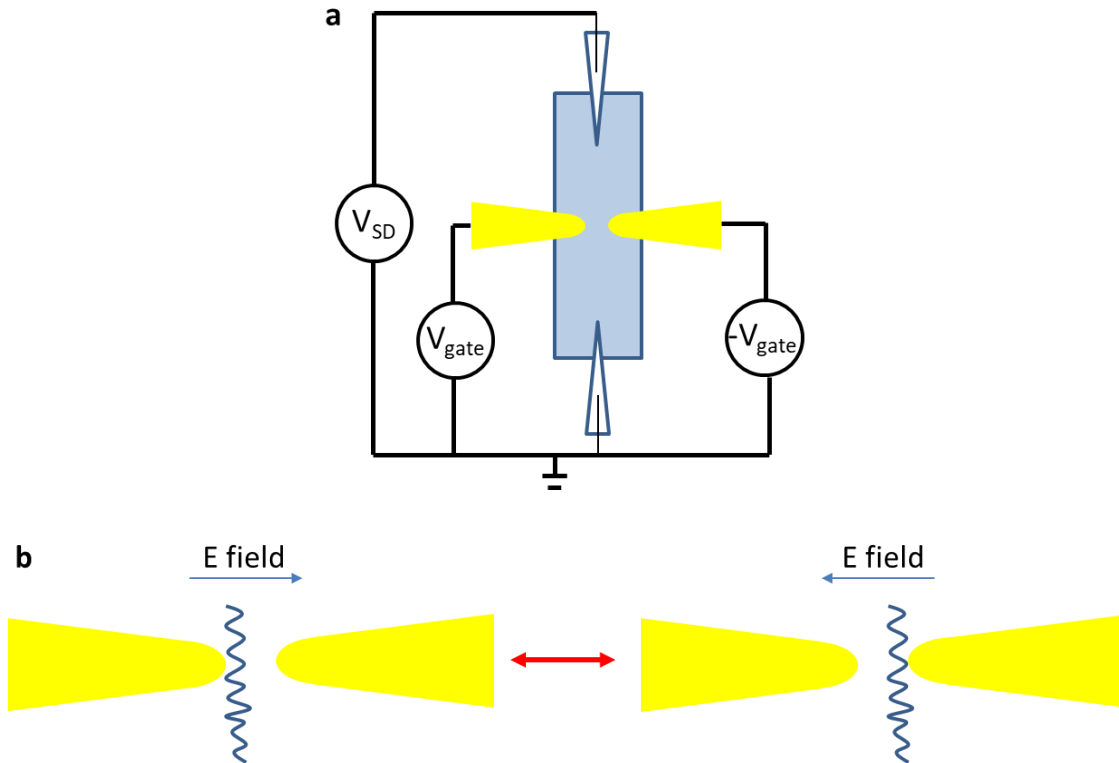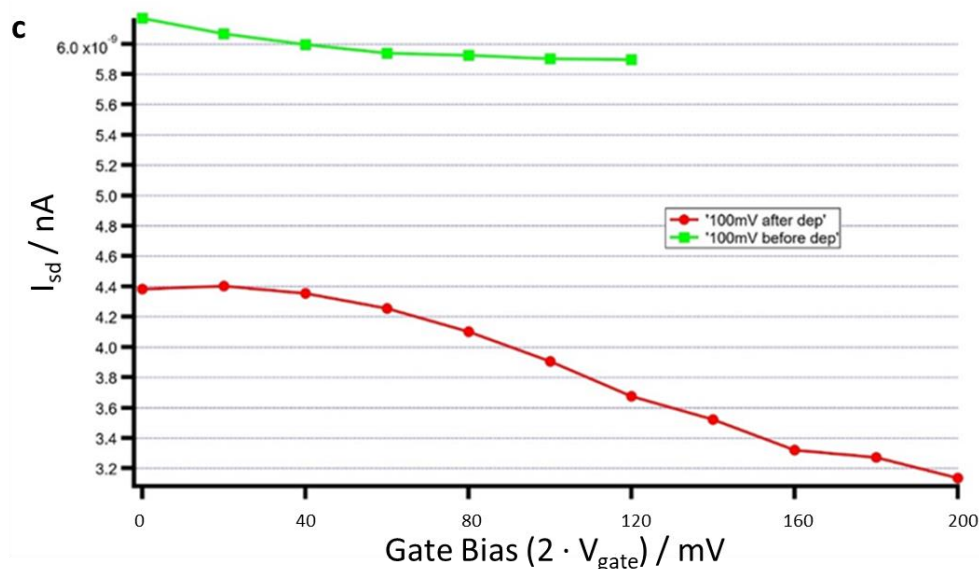
Figure 3.5.5. Gating Effect of Nanopore. (a) Diagram of experimental setup. A bias, V_{SD}, is established between Ag/AgCl electrodes on either side of the nanochannel which generates a through-channel ion current of I_{SD}. A potential of V_{gate} is applied to one gap electrode, while a potential of $-V_{gate}$ is applied to the other. (b) Effect of gate bias on DNA translocation. When a gate bias is applied, DNA will be attracted to one side of the nanopore, and interactions with the pore wall will slow the translocation speed. An alternating bias can ratchet a DNA molecule through the pore. (c) Effect of gate bias on ionic current. The green line shows ionic current through the channel before deposition for various gating potentials applied to the electrodes. The current is reduced by 5% at 60 mV. The red line shows ionic current after deposition. The current is reduced by 17% at 60 mV and 27% at 100 mV. Experiment conducted by Yuan Wang.

3.6   Discussion

The nanopore project has come a long way from when I started, and it is

instructive to take stock of where things stand. In particular, I want to review what has

been accomplished to date, what has yet to be accomplished, the most significant barriers

to further progress, and what can be done to overcome those barriers.

While progress has at times been slow, a considerable amount has been

accomplished. We have managed to design and assemble a complete device,

electrochemical deposition and control system, and microfluidic system, and we have

90

demonstrated the suitability of each of the components. In particular, we have shown that we can use top-down lithography to create electrodes with a sufficiently small gap that the gap can be closed by electrochemical deposition. We have demonstrated the ability to use electrochemical deposition to reversibly close and re-open a gap, and that we can monitor the status of the gap in real time with feedback controls. We have demonstrated the ability to effectively seal the deposition channel to confine the electrode growth to the lateral dimensions. We have figured out how to implement a microfluidic system that can exchange fluids and separate the two ends of the nanochannel. We can use an electric potential bias to drive DNA through a 10-nm high channel. We can image the motion of DNA in confined space. We can detect ion currents through the pore, and we can alter the resistance of the pore by applying potentials to the gate electrodes.

While we have individually demonstrated the structures, instruments, and systems necessary for a functioning nanopore sensor, we have not yet succeeded in getting all the components to work together precisely enough to meet our primary initial goal – the control of DNA molecules translocating the nanopore and detection by transverse tunnel current or ion current. This is the next milestone needed before work can begin on sequence detection. There are several contributing factors, but I believe the largest single barrier that remains is a lack of precise gap calibration. It is one thing to say, "This gap is likely less than 20 nm, but the electrodes have definitely not made contact," and another entirely to say, "This gap is between 3 nm and 5 nm." As mentioned previously, the primary difficulty in obtaining a precise calibration of the gap size comes from the difficulty in obtaining high-resolution imagery of a confined gap structure. In order to confine the deposition in the z-direction, the nanochannel must be sealed on the top. The

passivating material must be insulating, or else the electrodes would be shorted together, and the impedance monitor would fail. Using an insulator to seal the channel distorts top-down SEM imaging to the point that it cannot be used for nm-precise calibration. There are additional difficulties involved in attempting to remove the passivation. The fully-functional chip has a thick SU-8 layer which can only be removed, if at all, by being chipped off by brute mechanical force, an action which would almost certainly destroy the gap structure. A chip with no fluidic system would still need to have its HfO_2 passivation removed. HfO_2 was chosen in large part for its low reactivity, and removing 50 nm of HfO_2 requires a long etch in HF, which could damage other structures. Before any of this could happen, the wire bonds connecting the chip to the deposition control system would have to be severed. From experience, this action runs a significant risk of electrostatic damage to the electrode tips, a risk which increases as the gap size shrinks.

In an effort to avoid these problems, work has begun on indirect calibration by simultaneously monitoring the ionic conductance of the nanochannel along with the impedance between the electrode tips during deposition. This approach has shown some promise –the steady decrease in ionic conductance over the course of the deposition can be seen, but we have not yet seen consistent behavior at the very end of the deposition, which is the most critical portion. In some occasions, a residual ionic conductance has been observed even after the electrode tips have come into contact. This suggests that the deposited gold does not always fill the entire height of the channel, which could be a problem if it allows molecules to translocate without passing through the smallest constriction. In other cases, the ionic current has dropped to zero while the electrode tips

are still out of contact. This provides additional evidence that the electrodes can be used as gates to completely shut down ion transport.

While gap calibration has been perhaps the most difficult individual problem to solve, another significant barrier has been the overall complexity of the system. Because there are so many interacting components, we have often found that solving a problem in one component produces a new problem in a different area. We encountered this most notably while engineering the fluidic system. I have not gone into much detail about this, as the vast majority of the work was done by my colleague Yuan Wang, but the interplay between sacrificial layers, passivation layers, SU-8, PDMS, and various glues, etchants, and heat treatments took far longer than any of us imagined to sort out. Nevertheless, persistent effort has allowed us to make great progress in solving these problems.

Now that many of the discrete and systematic issues have been successfully addressed, it may be time to revisit the calibration problem with a systematic approach. It may be that we need to purpose-build some devices and interfaces to allow for high-resolution imaging of the nanogap. While I do not here propose a specific design or protocol, a few principles would need to be followed: The structure cannot include a full fluidic system with SU-8 walls but must operate in a single open fluid cell with only the passivation layer covering the nanochannel. The use of alternative, more easily etched materials to HfO_2 should be explored, while keeping in mind that the passivation layer must be resistant to the etchant used to open the inner sacrificial layer. Finally, a means to connect and disconnect the chip from the deposition circuit that avoids the risk of static damage must be found. Overall, I think the remaining challenges are well able to be overcome, and I expect the platform to be producing exciting data in the near future.

93

3.7 Future Work

This platform is ready to host a wide variety of applications, several of which are currently already in the beginning stages. The most direct continuation of my work will be the first experiments to demonstrate translocation control. For this, we will observe the translocation of DNA through the pore under different gate potentials. We hope to demonstrate that changing the potential of the gate electrodes affects the average dwell times of DNA within the pore.

A few projects that have just started will explore the use of different metals in the electrochemical deposition step. One project is investigating platinum as a possible replacement for gold in biosensing experiments. There have been some indications that the high surface mobility of gold is causing instability in the electrode tips. Platinum has a lower surface mobility than gold and could produce more stable pores. The other project is looking at nickel deposition. Because nickel is ferromagnetic, a device made from asymmetrically-deposited nickel electrodes could be used for spintronics investigations.

A further project that has recently started is exploring whether we can create a hybrid solid-state/protein nanopore. This would involve forming a lipid bilayer in the nanochannel between the electrode tips and inserting a protein pore. If successful, this might be a way to combine the superior uniformity of protein pore geometry with the gating capabilities of control electrodes.

Last, we are working on outfitting the gate electrodes with recognition molecules that can bind to proteins. Rather than seeking to detect translocation events, this project

will aim to trap proteins between the electrode tips to form molecular junctions that can

be probed to explore the electronic properties of proteins in a manner similar to the fixed-

gap devices which are the subject of the next chapter.

4. FIXED-GAP PROTEIN SENSOR

4.1   Introduction

In general, proteins are considered electronic insulators. They lack electronic conduction bands[76], and theoretical studies suggest that electron transfer takes place via electron tunneling or hopping processes between localized molecular orbitals[77, 78]. Despite this, proteins have been observed to conduct electricity at rates several orders of magnitude greater than that predicted by tunneling models[60,61,79]. Reconciling theory and observation has been somewhat difficult, as studies have been carried out on a wide variety of proteins, using different methods of connecting proteins to electrodes, and involving varying numbers of proteins in a contact – from single molecules to massively-parallel sheets[62-69]. Obtaining accurate measurements of the electronic conductance of proteins is significant on a number of fronts. A device with selective contacts could be used for high-sensitivity pathogen detection. The ability to track the conductance of a single protein over time could provide a new type of probe for studying protein dynamics[71]. Finally, and somewhat controversially, a more precise understanding of the mechanisms involved in protein conductance could give insight into unique properties of biomolecules as compared to nonliving materials[72].

In the past few years, research being done in Stuart Lindsay's group at Arizona State University has been shedding new light on the phenomenon of electronic conductance in proteins. This research illustrates several intriguing features of protein conductance, and it highlights the critical role that the contact between proteins and electrodes plays in the observed conductance[70, 71].

This research has been carried out with two different architectures. One of these involves an earlier iteration of the architecture that I am working with. In this process, top and bottom metal electrodes separated by a thin dielectric layer are fabricated on a silicon nitride membrane. A hole is then milled through the membrane with RIE in order to expose the electrode faces. In one experiment, the exposed electrode area was modified with cyclic RGD peptide, which binds specifically to the $\alpha_v\beta_3$ integrin protein[70]. A bias was applied between the top and bottom electrodes and the current was recorded. With the device in a 1 mM phosphate buffer solution at 7.4 pH, a featureless leakage current was recorded. The addition of an integrin protein, $\alpha_4\beta_1$, that does not bind to RGD did not materially affect the current. When $\alpha_v\beta_3$ was added, however, current jumps were observed clustered around two distinct values.
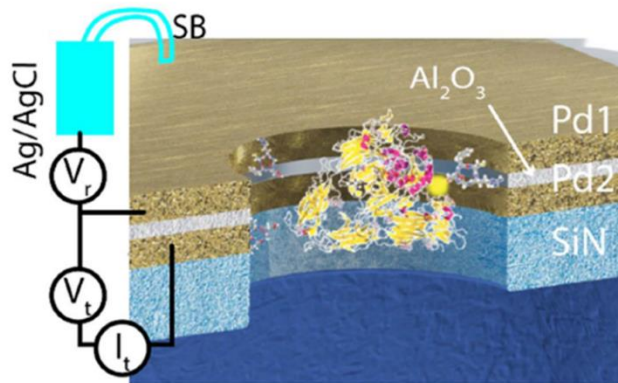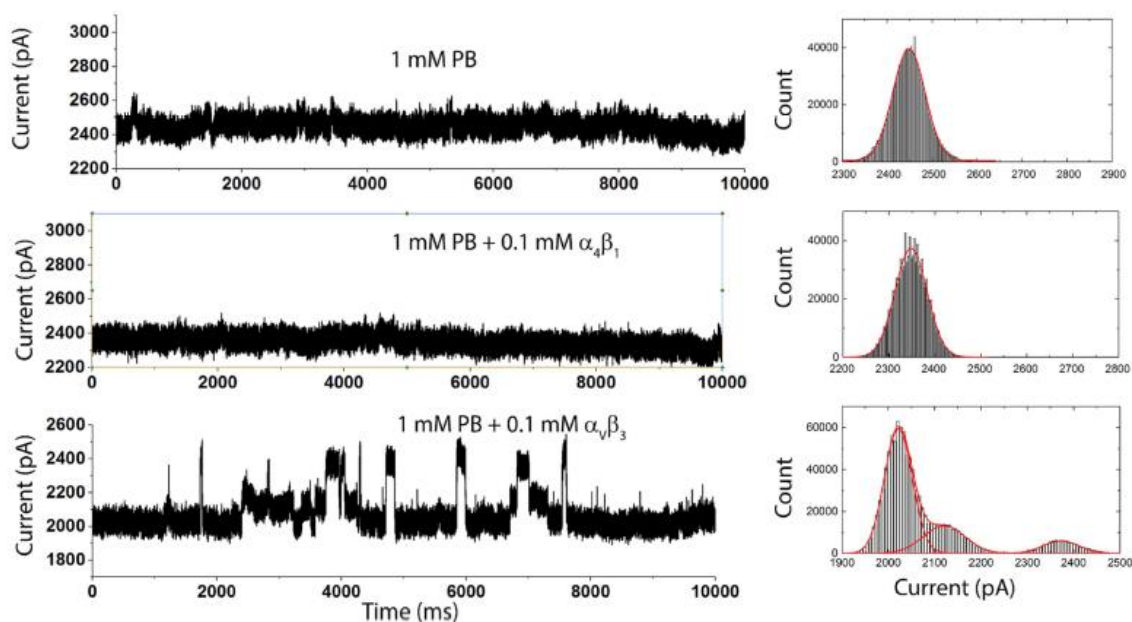
Figure 4.1.1. Protein Detection in Fixed-gap Chip[70]. (Top) Diagram of device construction. (Bottom) Current detected for (from top) buffer, non-binding control, and binding protein.

This result was an early indicator that electrode-protein contacts significantly affect protein conductance. The experiment also showed that the conductance behavior, at least for this protein, changed significantly with the level of applied bias. When less than 100 mV was applied, no current jumps were observed for avb3. At a threshold of 100 mV, the high-current state appeared to switch on, and as the bias increased from 100 mV to 300 mV, the protein spent an increasing percentage of the time in a high-current state.
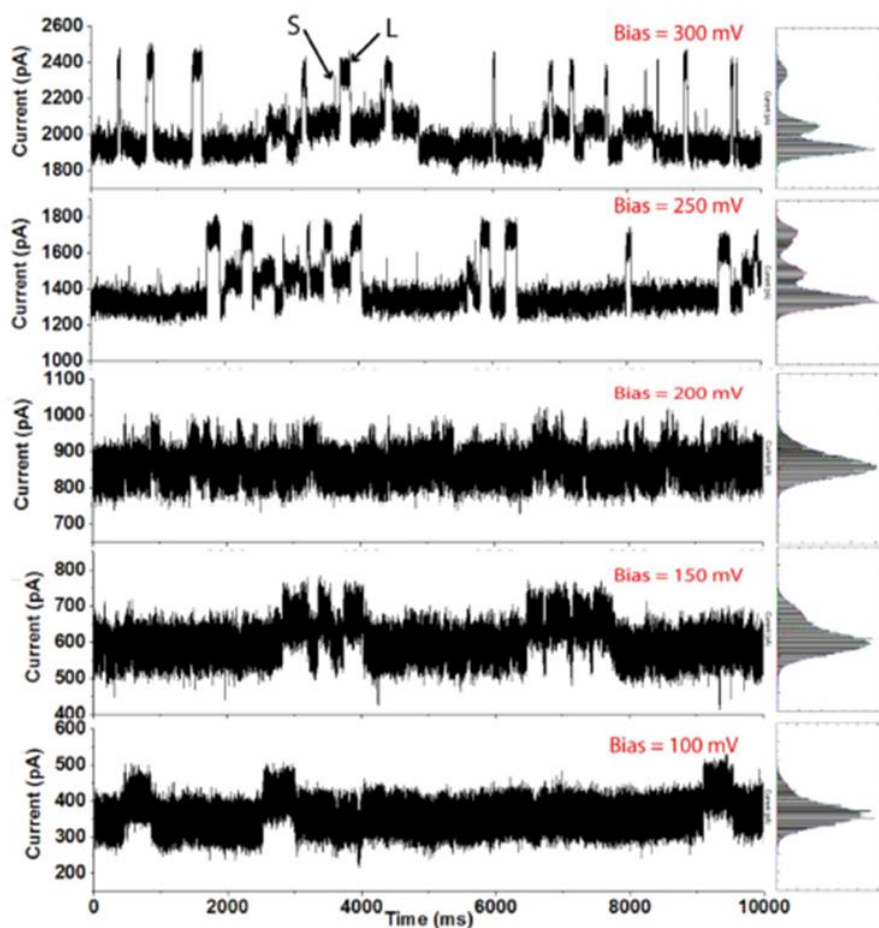
Figure 4.1.2. Effect of Bias on Protein Conductance[70].

The other architecture used for these experiments involves the use of a scanning

tunneling microscope (STM). In these experiments, there is a large, fixed bottom

electrode, and the STM tip serves as the top electrode. Both the substrate and the tip can

be chemically modified. This architecture was used to do a more systematic study of the

effect of contacts on protein conductance. In a recently published study, several different

proteins with different contact methods were examined[71]. In particular, proteins could

make contact with an electrode in three was: specific binding to a particular ligand

attached to the electrode, non-specific binding using hydrogen bonding to a molecule

attached to the electrode, or direct bonding to an electrode by altering the protein to
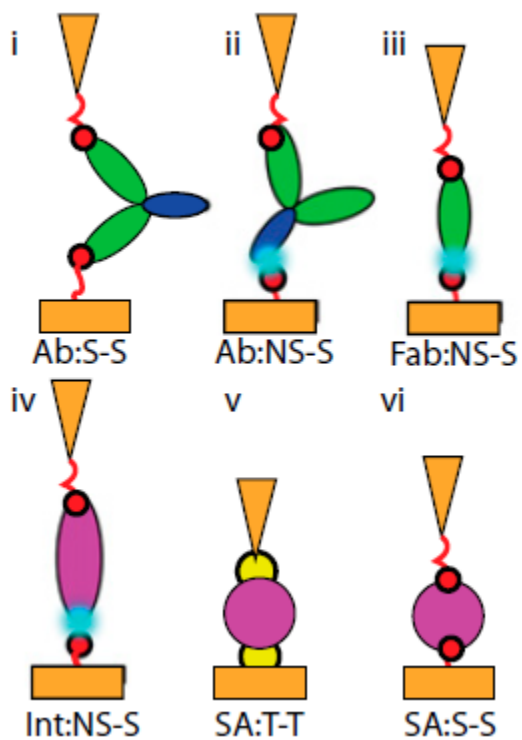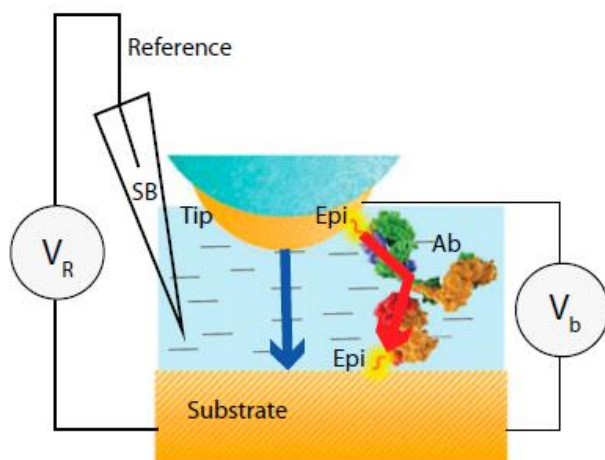
include a thiol group.

Figure 4.1.3. STM Measurements of Single Proteins[71]. (Top) Diagram of device construction. (Bottom) Different bonding schemes.

The results of this study were very illuminating. In general, it was found that the conductance behavior was determined almost entirely by the contact method, with only small differences between proteins. When no specific contacts were used, no signals were observed. Proteins bound by one specific contact and one non-specific contact showed a single conductance peak between 270 pS and 400 pS. Proteins bound by two specific contacts showed two peaks: a low-conductance peak similar to that observed with only one specific contact and one or more high-conductance peaks with a value of multiple nS.
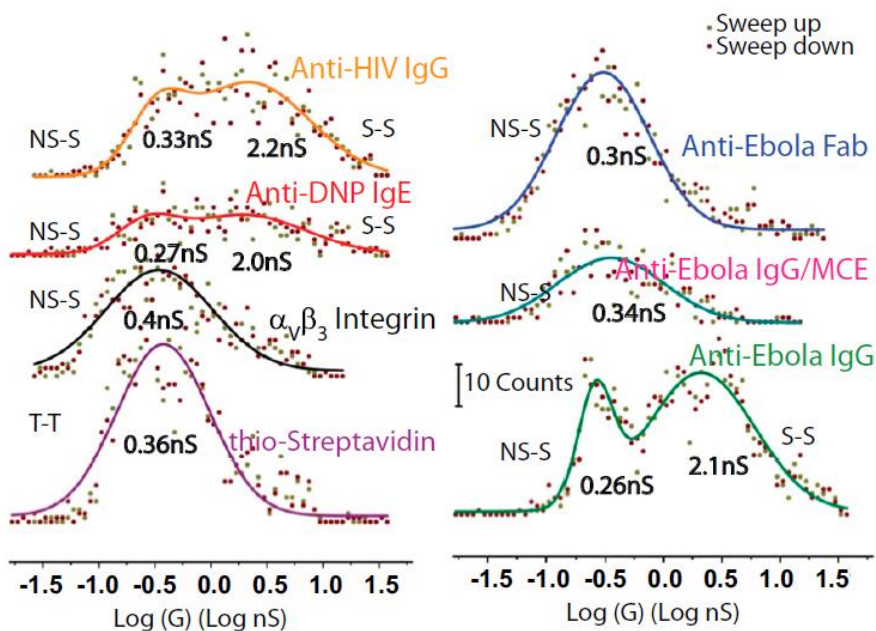

Figure 4.1.4. Conductance Distributions for Various Proteins and Binding Schemes[71].

Two additional observations stood out. One is that the distance between the substrate and the tip affected the number of contacts observed, but not the conductance. This strongly suggests that the electron transport is through the interior of the protein and not along the surface. The second observation is that direct thiol binding of a protein to an electrode yields similar conductance to binding with only one specific contact, despite the fact that the overall conductance path is shorter than when the protein is bound with two specific contacts. Curiously, a junction formed with one thiol bond and one specific bond has similar characteristics to a junction formed with two specific bonds. This is in stark contrast to the junctions formed with one specific contact and one non-specific contact. This again suggests that the key factor is not distance, but the way in which the contact between protein and electrode is mediated.
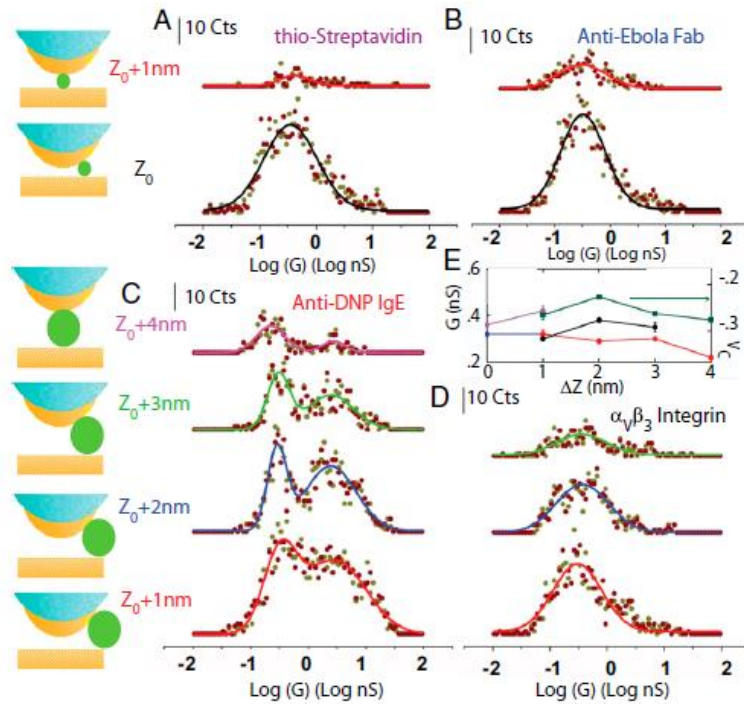
Figure 4.1.5. Conductance Distributions and Signal Yield as a Function of Gap Distance[71].
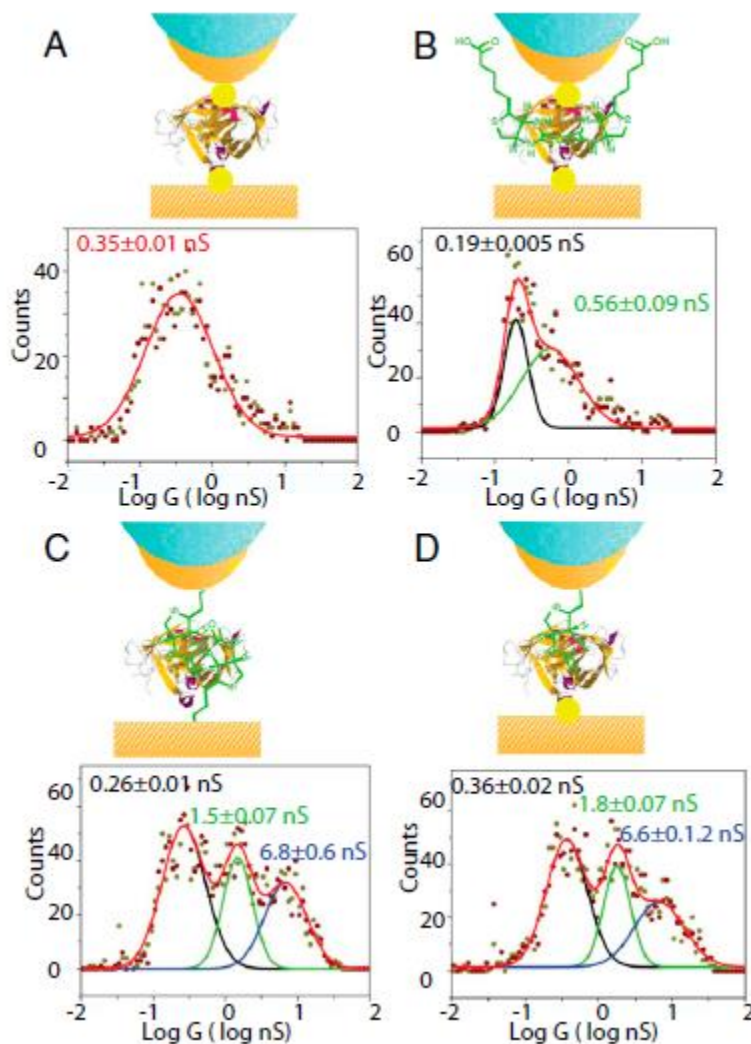
Figure 4.1.6. Direct Thiol Binding Compared to Binding with Specific Contacts[71].

My research is a continuation of these efforts in collaboration with the Lindsay group. In particular, my research focuses on developing a chip-based architecture for forming electronic protein junctions. A chip-based sensor offers superior portability and flexibility, and current readings are more stable than those of an STM, allowing for easier

analysis and reproducibility. Previous efforts at developing protein sensing chips, however, were hampered by several problems. First, fabrication yields were low, with a large percentage of devices being unusable for experiments. Second, signal yields were low, with only a small percentage of usable devices producing signals from protein junctions. Third, fabrication was inefficient, with only a small number of devices produced in each fabrication cycle. Among my objectives are the development of materials and processes to improve production efficiency, fabrication yield, and signal yield in order to meet the primary goal of producing sensor chips that can reliably and reproducibly form electronic protein junctions.

4.2 Chip Design

4.2.1 Essential Requirements

Before looking at the fabrication of the sensor chips, it is good to first examine the criteria that informed the chip design. There are several key requirements for a chip-based protein conductance sensor. One such requirement is that we want uniformity in the contact environment. In other words, we want to make sure that the size and shape of the gap are the same across every device for a given set of fabrication parameters. Second, we want stability in the contact environment. We want to make sure that the gap stays the same over the course of an entire experiment. Ideally, we would like to reuse the same gaps for multiple experiments to show the robustness of the approach. We also would like to see multiplicity of devices across a chip. This requirement is not necessary to obtain reliable data, but it is of strong practical import to mitigate against a shortcoming of the chip-based architecture *vis a vis* STM-based measurements. With an

104

STM setup, if a particular location on the substrate does not yield a signal, the tip can easily be moved to another location until a signal is found. On a chip, there are a discrete number of sites that can be tested, and the electrode area per site is orders of magnitude less than the available area on the STM substrate. To counteract this vulnerability, we would like to fit as many devices as we reasonably can onto each chip. The need is highlighted by the recent experiences of some of my collaborators, who, being provided chips from a vendor with only three devices each, frequently found entire chips that did not yield usable data.

4.2.2   Key Features of the Nanogap

It comes as no surprise that the most critical element of design for a fixed-gap protein-sensing chip is the gap itself, and the required parameters for the gap are what drive the choice of how to construct the gap. The gap needs to be on the order of 5 nm[a], and it should be reproducible throughout the fabrication batch. These requirements are very similar to those of the nanopore sensor, but with one key difference. For this device, we want molecules to bind across the gap, not pass through. This allows us to avoid the complications of engineering a microfluidic system and explore more conventional ways of creating a nanogap through standard semiconductor fabrication processes. Ideally, we would fabricate a lateral gap between adjacent electrodes on a substrate, but we do not have the available tools at ASU for sub-10 nm lithography. We do, however, have the ability to deposit thin films of both metals and dielectrics with sub-nm precision in thickness. In particular, we have an atomic layer deposition (ALD) tool which can deposit high-density, conformal dielectric films at the thickness required for the nanogap

---

[a] The exact size can be tuned based on the size of the target protein.

distance. We can therefore make metal layers which are vertically separated from each other by the appropriate distance, but such a sandwich structure carries with it two additional obstacles. The first is accessing the gap, which will be buried after initial fabrication. We can use RIE to cut anisotropically through the stack and expose the surface (i.e. access the nanogap). The second obstacle inherent to a sandwich structure is leakage currents. At very small gap distances, there will be electron tunneling through the dielectric, which can be significant for very large overlap areas. More important is the potential for pinholes in the dielectric film, which can cause complete shorts of the devices (leakage conductance on the order of 100 µS compared to protein signals around 1 nS). In order to minimize shorts, we therefore want to minimize overlap. This suggests a structure where the bottom and top electrodes cross over each other, with a RIE window designed to cut in the middle of the overlap.

With well-controlled fabrication processes, this design should result in the creation of uniform nanogaps for the experiment. The stability of the gaps is closely related to the choice of materials for the metal and dielectric layers, which is considered in more detail in the next section.
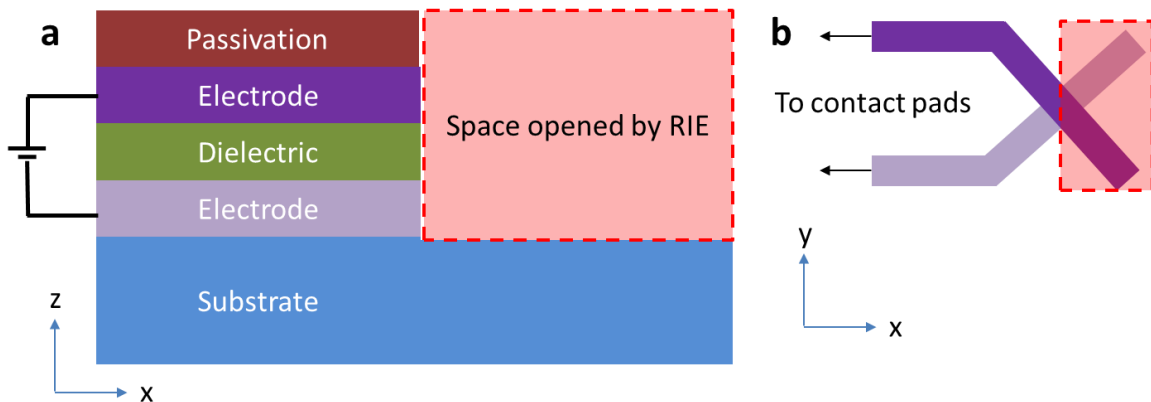
Figure 4.2.1. Basic Fixed-gap Device Structure. (a) Cross-section of device showing essential layers and the space carved away by RIE to expose the junction face. (b) Top view of device showing electrode crossing and RIE window. Dielectric and Passivation layers omitted for clarity.

4.3.3 Additional Design Considerations

While less critical than the nanogap structure itself, there were additional design features that provided practical benefits. The chip layout was designed to fit 32 independent devices on each chip. This provides significant protection against fabrication losses and allows for a higher ratio of experiment time to fabrication time. Additionally, test features were integrated into the devices. Each electrode within a given layer (top or bottom) connects to another electrode on the same layer. This allows us to verify the integrity of the metal lines and detect line breaks. The RIE cut, in addition to exposing the nanogap, severs the connections, making each device independent.
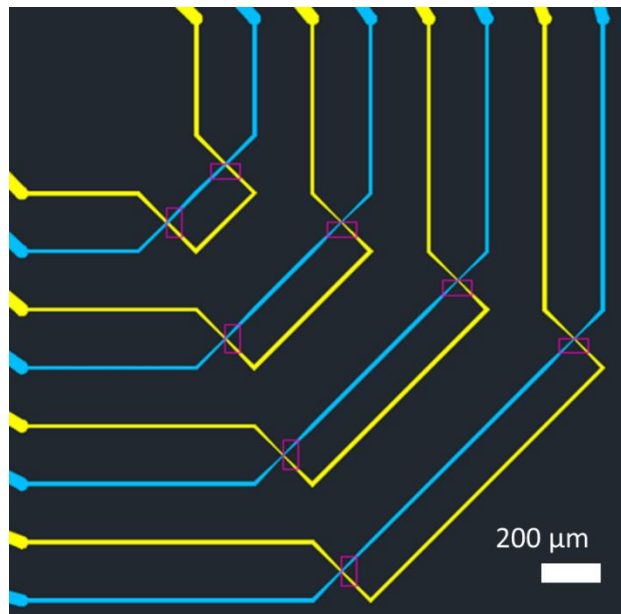

200 μm

Figure 4.2.2. Arrangement of Devices on One Quadrant of a Chip. Schematic shows bottom electrodes (yellow), top electrodes (cyan), and windows for RIE cuts (magenta). Each electrode line on the left is connected with another on the top to allow the continuity of the metal film to be tested. After RIE, these connections are severed, forming junctions composed of adjacent top and bottom electrodes.

4.3   Fabrication of Devices

The fabrication process for the fixed-gap chip has gone through a number of changes of material and procedure. I will first describe the current process before examining some of the areas in which testing determined the need for a change.

4.3.1   Procedure for Representative Device

As with the nanopore chips, fabrication for the fixed-gap chips begins with the deposition of markers to ensure that successive layers are aligned with each other within a tolerance of 700 nm. After the alignment marks are deposited, the bottom inner electrodes composed of Cr/Pt 1/6 nm are deposited by electron-beam evaporation. Next, bottom outer electrodes composed of Cr/Au 2/50 nm are deposited by thermal evaporation. The outer electrodes overlap the inner electrodes and end in large contact pads for connections to external electronics. After this, 1 nm of Cr is deposited by DC sputtering over the entire chip surface and allowed to oxidize in air[b]. Next, ALD is used to deposit 20-40 cycles of HfO_2 over the electrodes, which corresponds to a thickness of about 2-4 nm. This layer sets the nanogap spacing. After this, the top inner electrodes composed of Cr/Pt/Cr 0.5/15/0.5 nm are deposited by electron-beam evaporation. The top inner electrodes overlap with the bottom inner electrodes to create the metal-dielectric-metal structure which will later be cut to expose the nanogap. The top inner

---

[b] Electrical measurements indicate that the Cr oxidizes almost immediately on exposure to air, but future fabrication will introduce an additional oxygen plasma cleaning step as a safeguard.

electrodes are followed by the top outer electrodes consisting of Cr/Au 2/50 nm deposited by thermal evaporation. After the top outer electrodes are complete, an Al ring of 100 nm is deposited by electron-beam evaporation. This ring shorts all of the electrodes together in order to minimize the chances of electrostatic damage from handling and the later RIE process.

After the initial metal structures are complete, the chip is passivated with a 500-cycle ALD coating of HfO_2, with a thickness of about 50 nm. A RIE process is then used to cut through the areas where the top and bottom electrodes overlap. This exposes the face of the metal-dielectric-metal sandwich structure and completes the formation of the nanogap. A UV/ozone process is then done to clean the electrode surface.

In order to carry out experiments, the chip must be mounted onto a larger platform to interface with external electronics. First, the Al ring is removed with a wet etching process to electrically isolate the top and bottom electrodes from each other. Next, the electrode contact pads on the chip are attached to a printed circuit board (PCB) via ultrasonic wire bonding. Finally, a PDMS cell is glued to the chip surface to contain the fluids used in the experiments.

Figure 4.3.1. Complete Fixed-gap Device Cross-section. Schematic of device cross-section at electrode crossing, including (from bottom) SiN_x substrate (blue); bottom Pt electrode (gray), with Cr adhesion layer (orange) below; sputtered Cr layer (brown); HfO_2 dielectric (green); top Pt electrode (purple), with Cr adhesion layers (orange) above and below; and HfO_2 passivation layer (dark red).
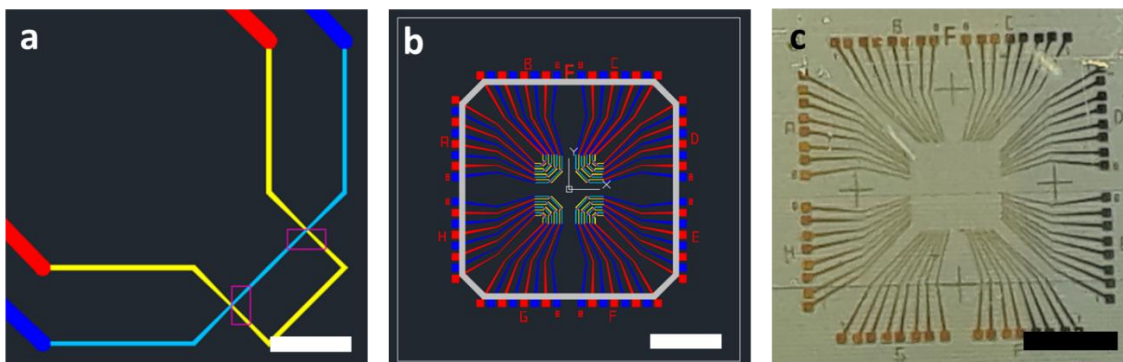
Figure 4.3.2. Top View of Chip Architecture. (a) Electrode crossings, showing bottom inner electrodes (yellow), bottom outer electrodes (red), top inner electrodes (cyan), top outer electrodes (blue), and RIE windows (magenta). Scale bar is 200 µm. (b) Overall chip architecture containing 32 electrode crossings as well as a ring (grey) to short all electrodes together until after the RIE process. Scale bar is 5 mm. (c) Photograph of finished chip after removal of the pre-shorting ring. Scale bar is 5 mm.

Figure 4.3.3. Fixed-gap Chip Assembly. Chip is connected to PCB by wire bonds. PDMS fluid cell is attached to chip with silicone gel and contains ports for fluid inlet and outlet and reference electrode insertion. Fluid cell interior is a single unstructured chamber.
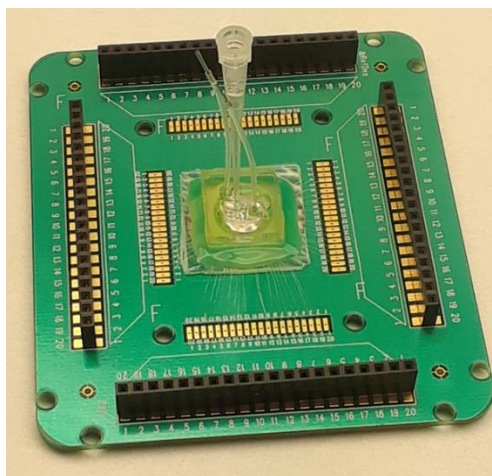
4.3.2 Electrode Material

There are several considerations that went into the choice of material for the nanogap electrodes. One key requirement was electrochemical stability. It is crucial that the electrodes be able to operate over a range of hundreds of mV without reacting with the chemical environment. A second key is the ability to form thiol bonds. As discussed previously, the attachment of proteins to electrodes is critically important to evaluations of protein conductance. Thiol chemistry allows reader molecules to be bound covalently to the electrode surface where they can then bind to the target protein.

When considering these requirements, the noble metals gold, palladium, and platinum are strong candidates. All of them are chemically and electrochemically stable, and all will readily form thiol bonds. The first electrode material to be tried was palladium. Gold has a high surface mobility, which could lead to instability in such a small gap. Platinum had been previously tried in a similar project by members of a

111

collaborating group, but they had encountered difficulties in producing smooth edges in evaporated Pt films. Given the crossed-electrode structure of these devices, rough edges (commonly referred to as "fencing") on the bottom electrode would likely have the effect of causing either a discontinuity in the top electrode or a short between the bottom and top electrodes.

The first batches of devices were fabricated using Pd electrodes, and their performance in initial fabrication was satisfactory. However, most devices did not give signals. Further investigation showed that Pd can be oxidized under conditions that the chip would experience during fabrication – high temperatures for baking photoresists, oxygen plasma for cleaning surfaces prior to metal evaporation, and UV/ozone cleaning of devices after exposing the electrode face. The presence of PdO at the electrode surface would inhibit the thiol modification and therefore the formation of protein bridges. It is possible to reduce PdO by passing a sample through hydrogen flame, but it is impractical for these devices and would introduce further complications as Pd will readily adsorb hydrogen. Avoiding oxygen plasma entirely would introduce risks to the fabrication process, and forgoing the UV/ozone treatment would likely result in contaminated electrodes.

It was decided to investigate the usage of Pt as a replacement for Pd, as Pt is much more difficult to oxidize and can therefore stand up to much more robust cleaning procedures. Initial tests indicated that the use of a lift-off resist and appropriate sample cooling were sufficient to produce thin Pt films without edge fencing. Additional tests verified the compatibility of Pt films with the thiolated recognition molecules, after which device fabrication shifted to use Pt for the electrode material.

4.3.3 Dielectric Material

Initial devices used aluminum oxide as the dielectric material between the electrodes. Alumina is very commonly used in semiconductor fabrication and was also employed in previous related projects. There are, however, certain drawbacks to alumina. Of greatest concern is the fact that common photoresist developers can etch alumina. There is literature that suggests that alumina deposited by ALD is not etched by developer, but even rates lower than 1 nm/min could harm the devices. Indeed, evidence from fabrication runs suggested that in some cases the alumina layers were being destroyed by subsequent development steps. In order to have a more robust process, the decision was made to switch to hafnium oxide for the dielectric layer in addition to the top passivation. Hafnia is not attacked by photoresist developers, and its greater chemical resistance also allows the use of more aggressive cleaning protocols.

4.3.4 Adhesion layers for ALD

The area that has undergone the most change has been the interface between the metal electrodes and the dielectric layer. One drawback to the use of noble metals for the electrode material is that they do not adhere well to dielectrics due to their resistance to oxidation. In order to avoid discontinuities in the dielectric film which would lead to shorted devices, it is necessary to add an extra adhesion layer in between the primary electrode material and the dielectric. The adhesion layer should be composed of an easily oxidized metal such as Ti or Cr that can bond strongly to both the noble metal electrode and the dielectric. Complicating matters is the fact that the portion of the adhesion layer exposed to the air after the RIE cut will be oxidized and contribute to the effective gap size. This limits the thickness that can be used to 1 nm or less.

113

Early batches of devices tended to have a high rate of electrode shorting. Various parameter changes were explored, including dielectric thickness, adhesion layer thickness, dielectric material, and adhesion layer material. While some of these parameters had a minor effect on device yield, a majority of devices measured as short even using the best parameters. Finally, the effect of the method of depositing the adhesion layer was examined. Initial efforts used electron-beam evaporation (deposited at the same time as the bottom electrode). Electron-beam evaporation is anisotropic, and while the adhesion layer would cover the top surface of the electrode, the side of the electrode would still have a noble metal surface. This could result in a failure of the dielectric film to adhere to the side of the bottom electrode and allow the top electrode to directly contact the bottom electrode. It was decided to test a DC magnetron sputter process instead of electron-beam evaporation. Sputtering produces a more conformal film than evaporation, which would result in deposition on the electrode side walls. Electrical connectivity tests showed a dramatic decrease in the percentage of shorted devices after the switch from evaporation to sputtering.
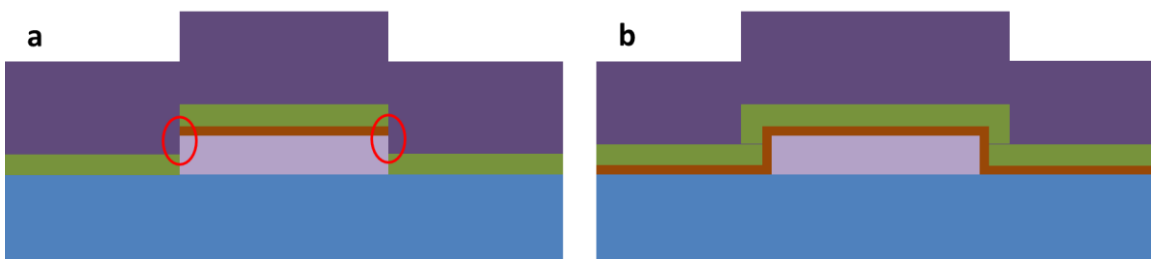
Figure 4.3.4. Adhesion Layer Methods. (a) Cr (brown) is deposited on top of the bottom Pt electrode (grey) by electron beam evaporation. This results in deposition only on the top surface of the electrode. The HfO_2 passivation layer (green) does not adhere well to the side of the bottom electrode, creating vacancies that can make contact with the top Pt electrode (purple) and cause a device short (red ovals). (b) Cr is deposited over the entire surface by magnetron sputtering. This results in a conformal deposition on all

surfaces of the bottom electrode. The passivation layer adheres well to Cr, producing a continuous dielectric film.

4.4   Device Characterization

In order to ensure the best experimental conditions and to assist in understanding the causes of any negative results from experiments, extensive tests have been done to characterize many of the physical and chemical attributes of the devices.

4.4.1   Platinum Edge Smoothness

As previously mentioned, there was concern about switching the electrode material from Pd to Pt due to previous poor performance of Pt thin films. In particular, "fencing" was seen on the edges of Pt features, high aspect ratio residues that result from metal being deposited on the side walls of developed photoresist. In order to evaluate the quality of evaporated Pt films, a nominal film of Cr/Pt 2/6 nm was deposited on a quartz substrate. The edge smoothness was evaluated in two ways. First, a profilometer was used to scan over an electrode edge and generate a cross-sectional height profile. Second, SEM images of the electrode surface were taken to check for any unusually high contrast that might indicate fencing. Both tests showed a smooth edge.
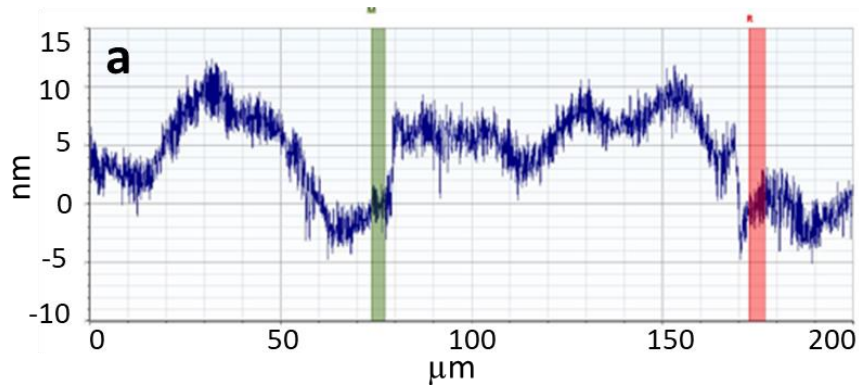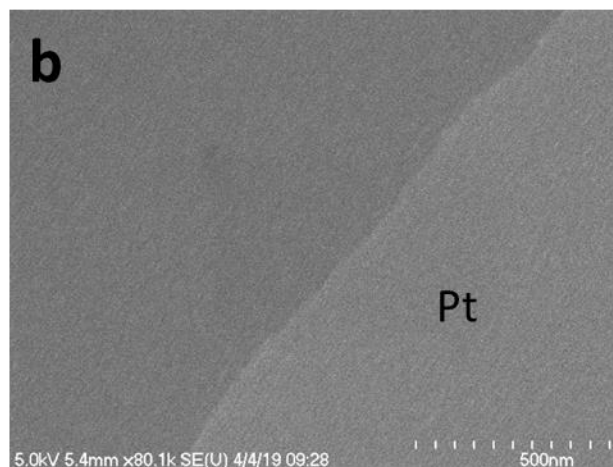
Figure 4.4.1. Platinum Electrode Smoothness. (a) Profilometer scan over a Pt electrode. The electrode edges lie between the green and red lines. The electrode measures 8 nm thick with no edge fencing seen. (b) SEM image of the same sample. The edge appears smooth and no fencing is seen.

4.4.2   Dielectric Thickness

In order to properly interpret the experimental results, it is critical to know the

thickness of the dielectric layer. As a general rule of thumb, the ALD process produces a

film which increases by about 1 Å for every process cycle, but the exact thickness varies

by the material and the particular tool. Complicating matters is the fact that film

thickness tends to be somewhat non-linear at low cycle numbers. In order to accurately

measure the film thickness, it is necessary to do direct imaging with a transmission

electron microscope (TEM). To do this, a cross-sectional slice is cut out of a sample with

a focused ion beam (FIB) tool, and the resulting slice can be imaged with the TEM. In

Figure 4.4.2, we see a TEM image of a sample where 40 cycles of HfO_2 was deposited on

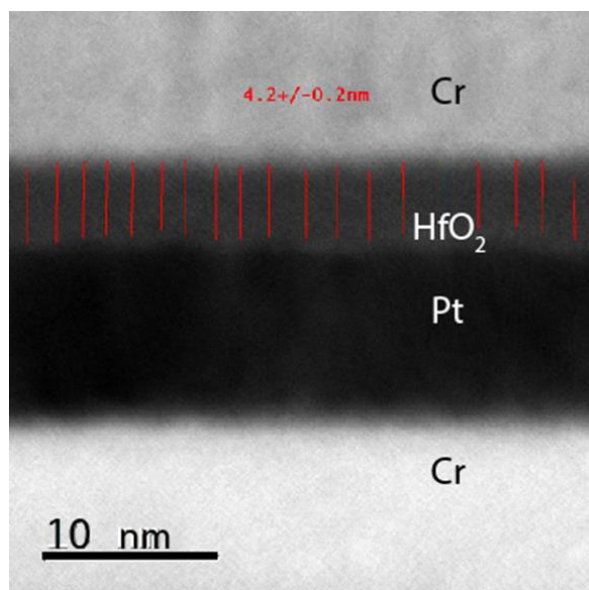a Pt electrode. The HfO_2 layer measured (4.2 ± 0.2) nm.

Figure 4.4.2. TEM of HfO$_2$ ALD Layer. 40 cycles of HfO$_2$ was deposited onto Pt by ALD. A cross-section slice was cut from the sample by FIB, and the slice was imaged by TEM. The thickness of the HfO$_2$ layer is measured as (4.2 ± 0.2) nm. TEM image taken by Weisi Song.

4.4.3 Dielectric Quality

A very important piece of information for evaluating the devices is the quality of the dielectric film. Any thin film deposition technique can leave pinholes when the film is thin enough, and I needed to determine the pinhole density at the relevant thicknesses for my experiments. This would allow me to know the likelihood that a particular electrode junction would have a pinhole. I came up with a test that allows for a simple optical evaluation. First, 18 nm of Cr was deposited on glass substrates. Next, thin films of HfO$_2$ were deposited by ALD. These films were deposited in 10-cycle increments up to 40 cycles. Next, the samples were immersed in chromium etchant for 5 minutes. Chromium etchant does not attack HfO$_2$, so the only way for the etchant to reach the Cr substrate would be through pinholes in the dielectric film. After 5 minutes, samples were rinsed in pure water, dried, and examined in an optical microscope. Any pinholes in the

117

dielectric film were marked by dark spots where the etchant had dissolved the substrate. A representative image for each cycle number was taken, the image was divided into 10-μm x 10-μm regions, and counted the number of pinholes in each region was counted. The mean and standard deviation of the pinhole density were then calculated. For the 10-cycle film, the pinhole density was high enough that the entirety of the Cr substrate was etched through in about 20 seconds, comparable to a control sample of Cr with no dielectric film. For 20-40 cycles, the pinhole density falls by half for each additional 10 cycles, as seen in Table 1. Figure 4.4.3 shows the subdivided images for 20- 30- and 40-cycle HfO_2.

Table 4.4.1

Pinhole Density Test

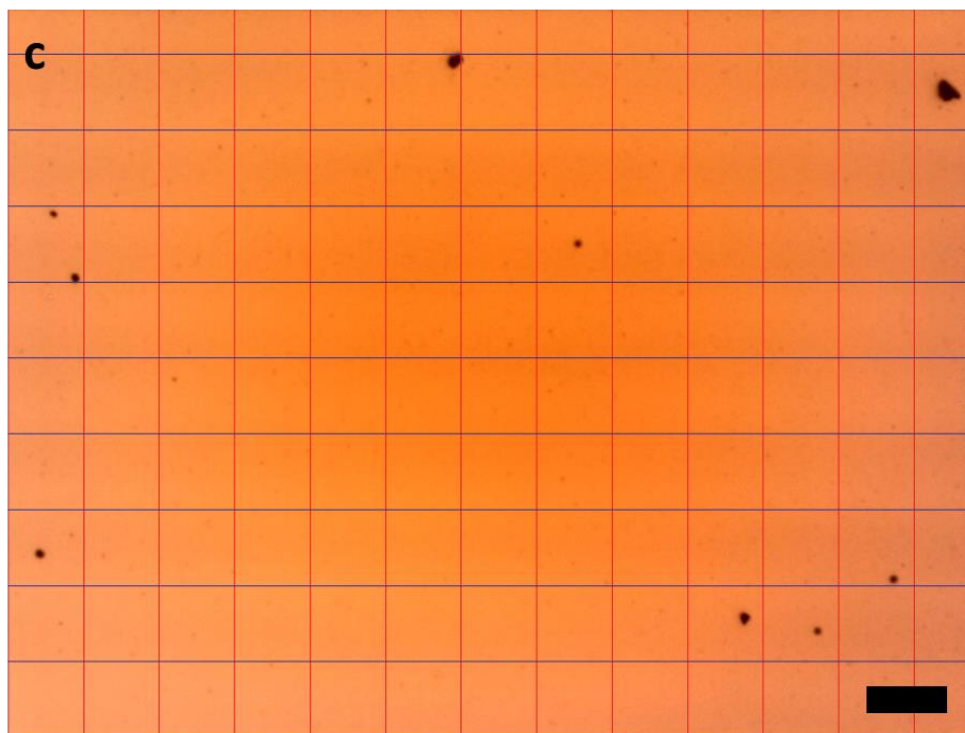| Pinholes observed in 100 μm^2		
Cycles	Average	Standard Deviation
20	1.95	1.48
30	1.1	1.14
40	0.5	0.86
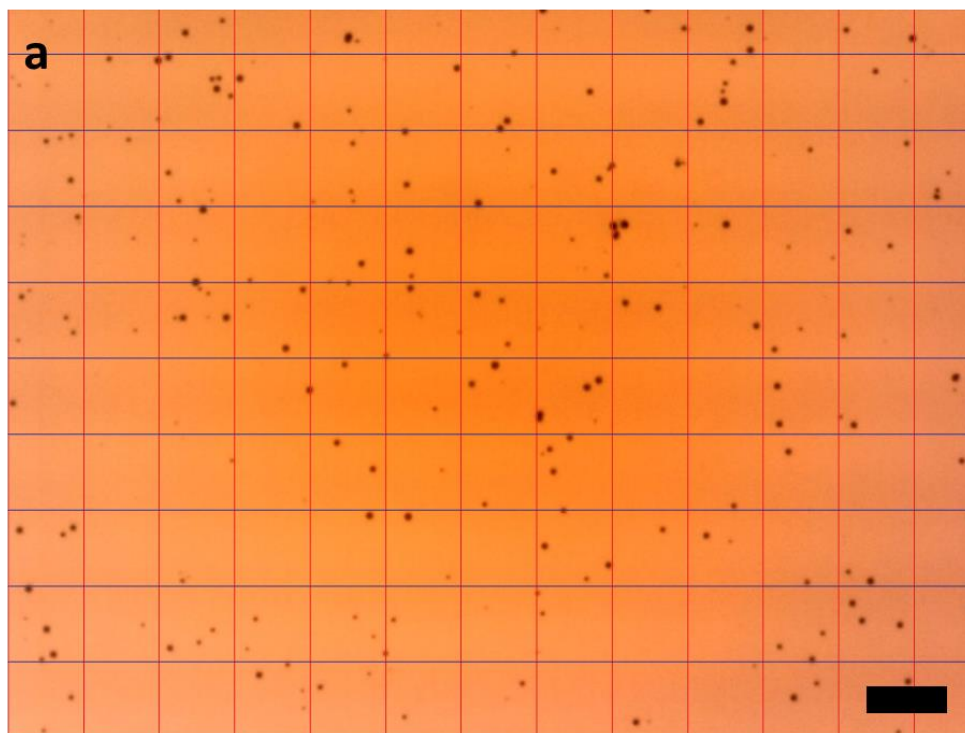
Figure 4.4.3. HfO$_2$ Pinhole Tests. Grid spacing and scale bars are 10 µm. (a) 20-cycle ALD. (b) 30-cycle ALD. (c) 40-cycle ALD. Note that values in Table 4.4.1 above count both dark and faint spots.

4.4.4   *Effect of Parameters on Electrode Shorting Rates*

One of the most significant fabrication issues that I had to overcome was high

rates of shorting between top and bottom electrodes in the device. The intrinsic

conductance of a fully shorted device is on the order of 100 µS, while the conductance of

a single protein is on the order of 1 nS, so any shorted device will be useless for protein

sensing. My initial set of fabrication parameters resulted in chips with device short rates

around 90% or greater. I tested a variety of combinations of materials and layer

thicknesses, and most parameters had a limited effect on short rate[c]. The exception was

---

[c] Increasing the dielectric layer thickness would, of course eventually remove any shorts, but the total gap thickness is constrained by the size of the target protein, in my case to about 5 nm.

transitioning to sputtered Cr for the adhesion layer between the bottom electrode and the

dielectric. This resulted in a dramatic decrease in the percentage of shorted devices.

Results from shorting tests are displayed in Table 2. Data is limited as this is a recent

change to the protocol.

Table 4.4.2

Effect of Adhesion Layer on Device Shorting

	Low Leakage (0 - 100 pS)	Moderate Leakage (100 pS - 10 nS)	High Leakage (10 nS - 1 μS)	Short (> 1 μS)
Pt with evaporated Cr	7/32 (22%)	0/32	0/32	25/32 (78%)
Pt with sputtered Cr	46/61 (75%)	4/61 (7%)	0/61	11/61 (18%)

4.4.5   *Oxidation of Sputtered Cr*

In order to coat the sides of the bottom electrodes, 1 nm Cr is sputtered over the

entire surface. While Cr is known to oxidize readily in air, it needs to be demonstrated

that air-oxidized Cr does not short adjacent bottom electrodes together. To demonstrate

this, a potential of ±10 V was scanned between adjacent bottom electrodes. A

conductance of only 2 pS was observed, far smaller than the conductance of a single

protein and also smaller than the typical leakage conductance between top and bottom

electrodes.

4.4.6   *Alignment Accuracy*

In order to have the nanogap surface exposed, there must be a precise alignment between the bottom electrode, top electrode, and RIE window. The alignment accuracy of the exposure tool will therefore set a lower limit on the size of the electrode crossing area. SEM images of devices shows alignment errors consistently less than 1 um. RIE cuts successfully expose the nanogap junction for all devices with side lengths of 3 µm and 4 µm. The vast majority of devices with side lengths of 2 µm are properly cut, and about half of 1-µm length devices are properly cut.
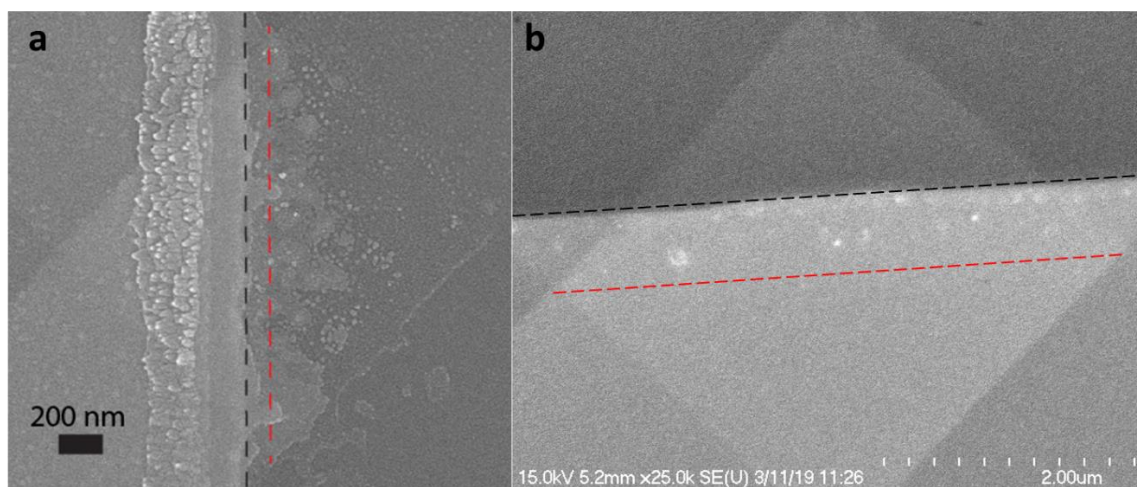
Figure 4.4.4. Alignment Accuracy. (a) Best-case alignment accuracy. Black dashed line is edge of RIE cut, while red dashed line is the center of the electrode crossing. Lines are about 120 nm apart. (b) Worst-case accuracy. Lines are about 670 nm apart, but RIE cut is still within the electrode crossing.

4.4.7 Electrochemical Scans

While running a potential sweep between top and bottom electrodes in a dry state can tell if a device is shorted, a dry scan is unable to determine if the nanogap surface is properly exposed. For this purpose, we can scan electrodes in an electrolyte solution against a Ag/AgCl reference electrode. If the electrode is in contact with the solution, a

current should be generated, but if the electrode is not in contact, no current will be seen.

Figure 4.4.5 shows electrode scans in 100 mM H_2SO_4.
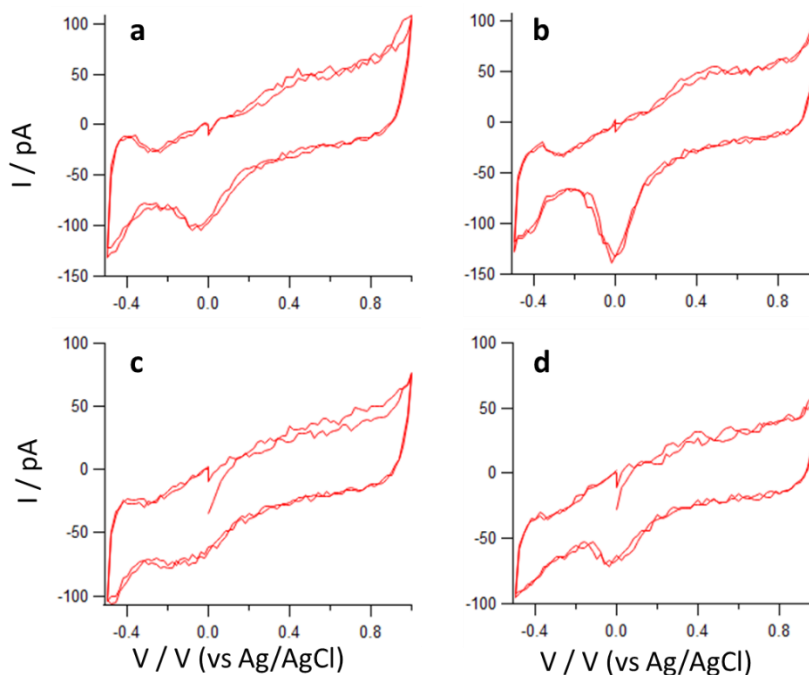
Figure 4.4.5. CV scans of Pt Electrodes. (a-d) CV scans of four different Pt electrodes. All scans conducted in 100 mM H_2SO_4, with an Ag/AgCl reference electrode and Pt wire counter electrode.

4.5   Experimental Results

4.5.1   *Device pre-testing*

Each chip, regardless of the target molecule, undergoes a suite of characterization tests prior to the beginning of the experiment proper. The first test is a linear voltage sweep between top and bottom electrodes in dry state. This test sets the background leakage current level for each device and also identifies any shorted devices. Typically, the sweep range is ±100 mV with a sweep rate of 50 mV/s. Most shorted devices measure

between 100 µS and 200 µS, but we consider any device with a dry conductance above 1 µS to be shorted.

A fairly recent addition to the pre-testing protocol is an additional linear voltage sweep in 100 mM H_2SO_4. This test was not employed for devices with Pd electrodes and Al_2O_3 dielectric layers, due to concerns that the acid would harm the devices, but it has been employed for devices with Pt electrodes and HfO_2 dielectric layers. This scan has two objectives. First, it gives an indication that electrodes are properly contacting the fluid, which cannot be measured by a dry-state scan. Second, the acid scan helps to clean any organic contaminants on the electrode surface. The acid scan is best done by sweeping a single device electrode relative to an Ag/AgCl reference electrode. This allows each electrode to be evaluated for fluid contact independently. Representative scans can be seen in Figure 4.4.5 in Section 4.4.

4.5.2   DNA Polymerase

The first experiment that has been run with this platform investigates the phi29 DNA polymerase and is aimed at developing a novel method of sequencing DNA. In this experiment, a solution of 50 µM $HSCH_2CH_2$-biotin in degassed ethanol is introduced into the fluid chamber and left to incubate overnight. The thiol group of the modified biotin bonds with the platinum of the electrodes, resulting in a biotin surface coating for the electrodes. Next, the chamber is rinsed five times with degassed ethanol to remove any excess biotin. Next, the ethanol is replaced with 1 mM phosphate buffer (PB) at pH 7.4, and a linear voltage sweep is performed to set the baseline wet conductance of each device. Next, a solution of 1 µM streptavidin in 1 mM PB is introduced and allowed to incubate for 30 minutes. The streptavidin will bind to the biotin on the electrodes. Next,

124

the chamber is rinsed five times with 1 mM PB to remove excess streptavidin, and a second linear voltage sweep is performed on each device. Next, a solution of 1 µM biotinylated phi29 DNAP in 1 mM PB is introduced, while in real time, the conductance of one of the devices is monitored under a fixed potential of 10 mV. The two biotin molecules on each polymerase are expected to bind to vacant positions on the streptavidin molecules attached to the electrodes. If the polymerase binds to streptavidin molecules on opposing electrodes, this will create a bridge across the nanogap, and the observed conductance will increase. After 2 hours, the chamber is rinsed 3x with 1 mM PB to remove excess DNAP and a linear voltage sweep is performed on each device. Any device that shows elevated conductance compared to baseline is monitored under fixed potentials ranging from 10 mV to 300 mV. Next, A solution of 200 nM template DNA and 4 mM TCEP is introduced, while in real time, the conductance of one of the devices is monitored under a fixed potential of 10 mV. The template DNA is expected to bind to the polymerase and may alter the conductance of any device with a polymerase bridge. After 30 minutes, a linear voltage sweep is performed on each device, and any device that shows elevated conductance compared to baseline is monitored under fixed potentials ranging from 10 mV to 300 mV. Last, a solution of 1 mM dNTP and 10 mM $MgCl_2$ is introduced, while in real time, the conductance of one of the devices is monitored under a fixed potential of 10 mV. As the polymerase polymerizes the bound DNA, the conformation of the polymerase will change. This is expected to be reflected in a series of rapid changes to the observed conductance. After 15 minutes of monitoring the first device at fixed potential, a linear voltage sweep is performed on each device.

Any device that shows elevated conductance compared to baseline is monitored under fixed potentials ranging from 10 mV to 300 mV.

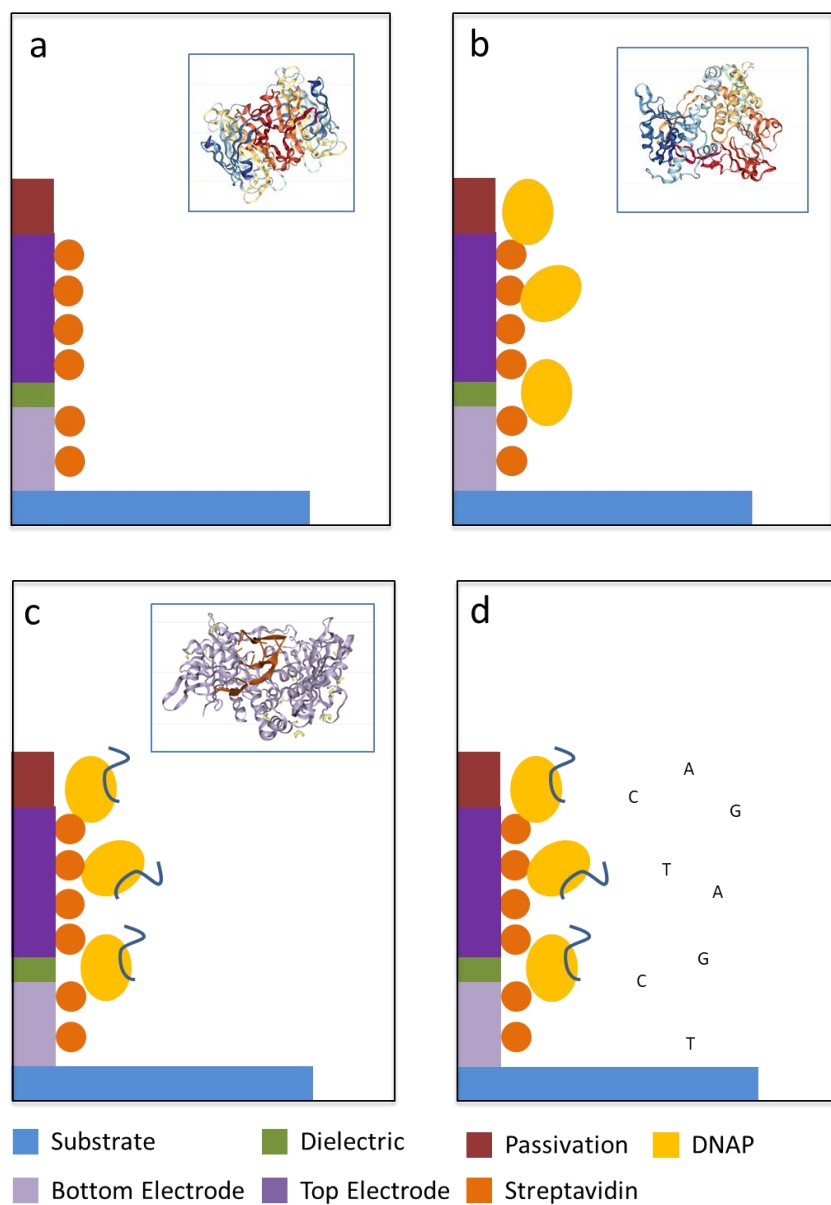Figure 4.5.1. Polymerase Experiment Sequence (a) Electrodes are modified with thiolated biotin and streptavidin. Inset shows structure of streptavidin (credit Protein Data Bank). (b) Phi29 DNA polymerase modified with biotin binds to streptavidin and bridges the nanogap. Inset shows structure of phi29 DNAP (credit Protein Data Bank). (c) Template DNA is captured by the polymerase. Inset shows structure of phi29 DNAP -

DNA complex (credit Protein Data Bank). (d) Free nucleotides are polymerized by the polymerase, generating fluctuations in the junction conductance.

This experiment has yielded some exciting early results, though consistent interpretation of the data has been difficult. The first significant signals came from an experiment performed on November 20, 2018. This was the first recording of signals after adding dNTP. During fixed-potential scans at 10 mV on one of the devices, major conductance peaks were observed at 10 nS and 26 nS, which are significantly higher than conductance values obtained from STM measurements. The large peak centered around 10 nS exhibited several smaller peaks with an average spacing of 2.3 nS, which are comparable to single-molecule peak values obtained from STM measurements. It is possible that the data represents a contact composed of multiple DNAP molecules, but without additional data, this is purely speculative.
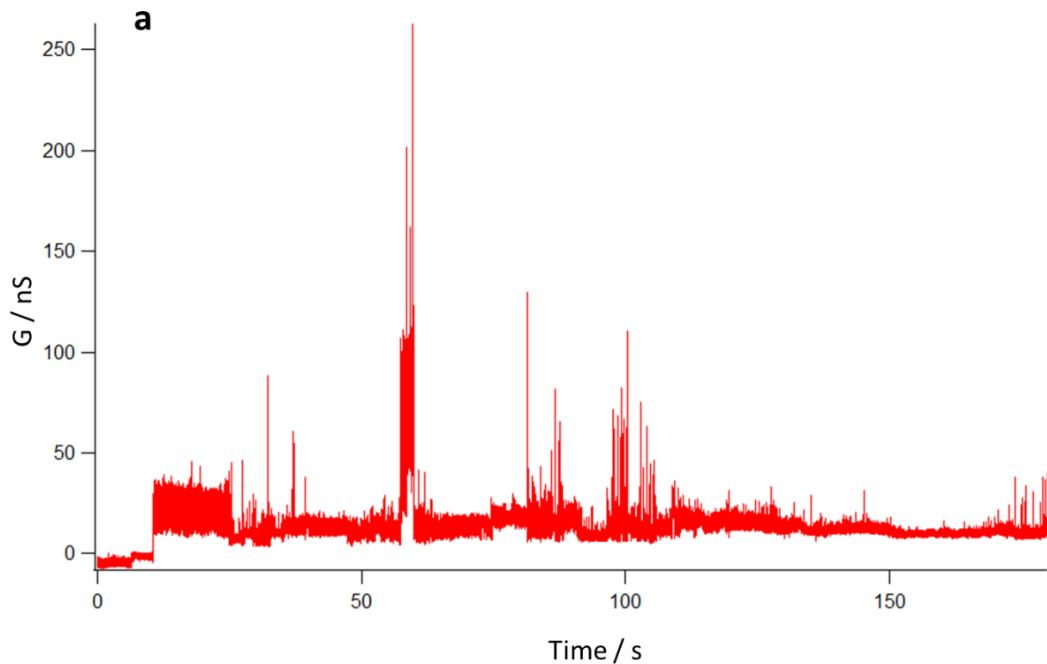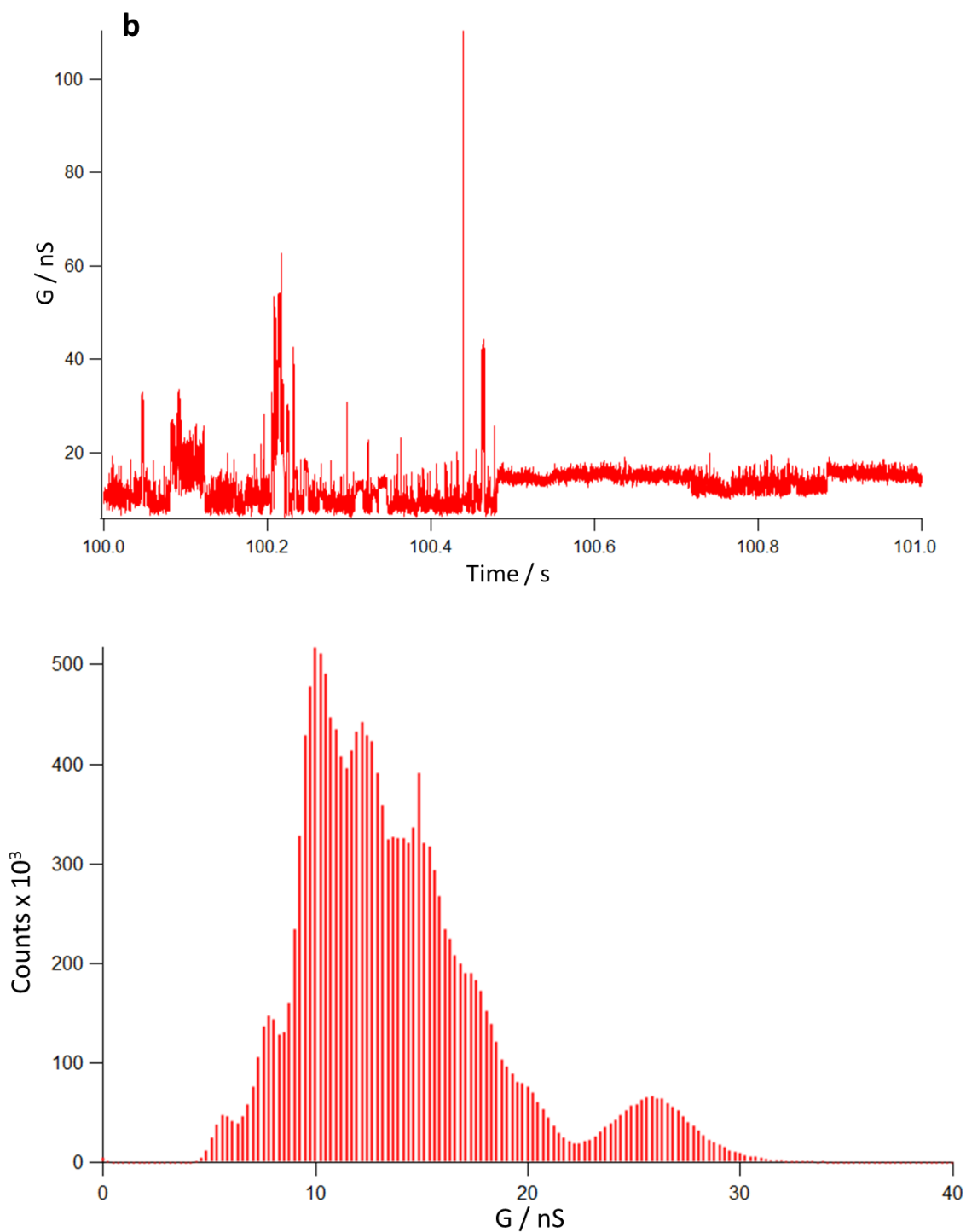
Figure 4.5.2. Polymerase Signals at 10 mV Bias After Adding dNTP. (a) Total conductance trace over 180 s of observation. (b) Close-up of a 1 s interval. Both shifts of the baseline conductance and short-duration conductance spikes can be seen. (c) Distribution of conductance values with 250 pS binning. The presence of distinct peaks

may represent either different configurations of the polymerase or different numbers of polymerase junctions. Experiment jointly conducted with Weisi Song.

The most exciting results came from an experiment performed January 30, 2019. In this experiment, two-level fluctuations from 1-2 nS in the conductance were observed after adding DNAP and persisted after adding A_{10} template DNA. About a minute after the addition of dNTP, larger conductance fluctuations of about 5-10 nS height and 2 ms duration appeared under a driving bias of only 10 mV, while the smaller conductance fluctuations persisted. What makes these results particularly exciting is that the two-level fluctuations match extremely well with STM measurements. STM data shows small fluctuations in DNAP signals prior to the addition of dNTP, and large fluctuations that only appear when dNTP is added. For both sensing platforms the ratio of large fluctuation amplitude to small fluctuation amplitude is similar, about 5:1. Interestingly, the size of the fluctuations in the chip measurement is about 10 times as high as the fluctuations in the STM measurements. As yet, there is no explanation for this discrepancy.
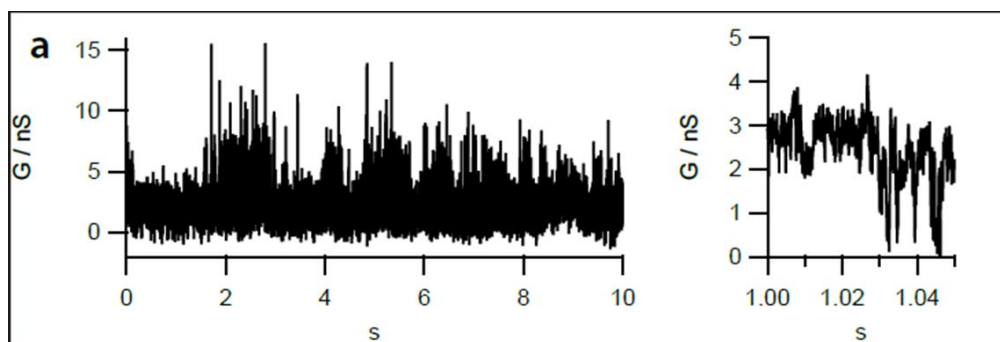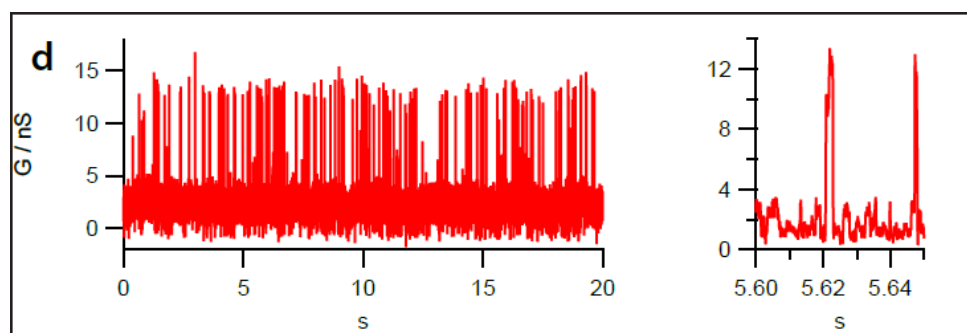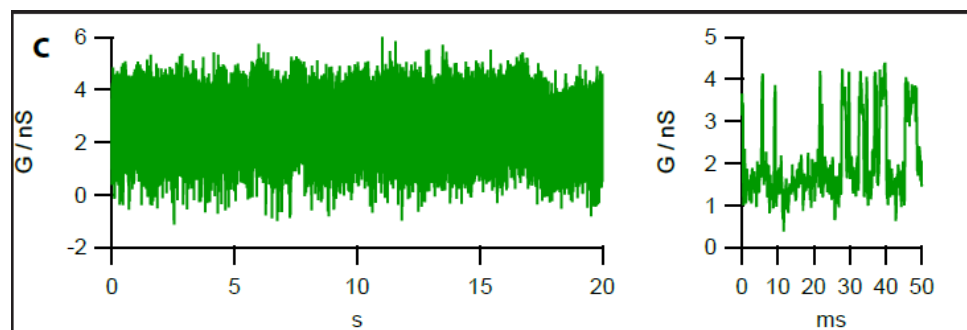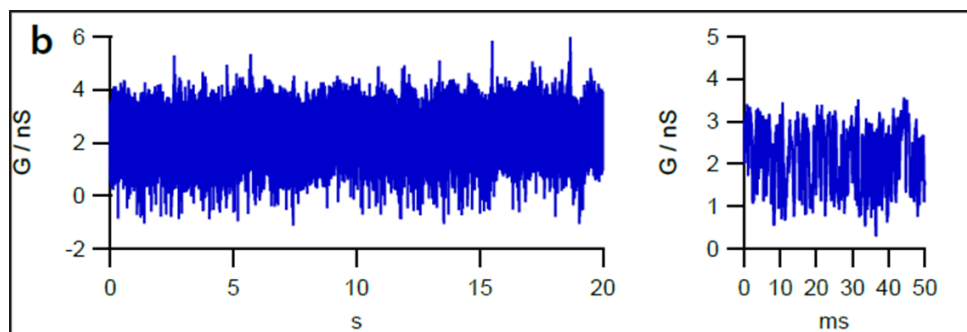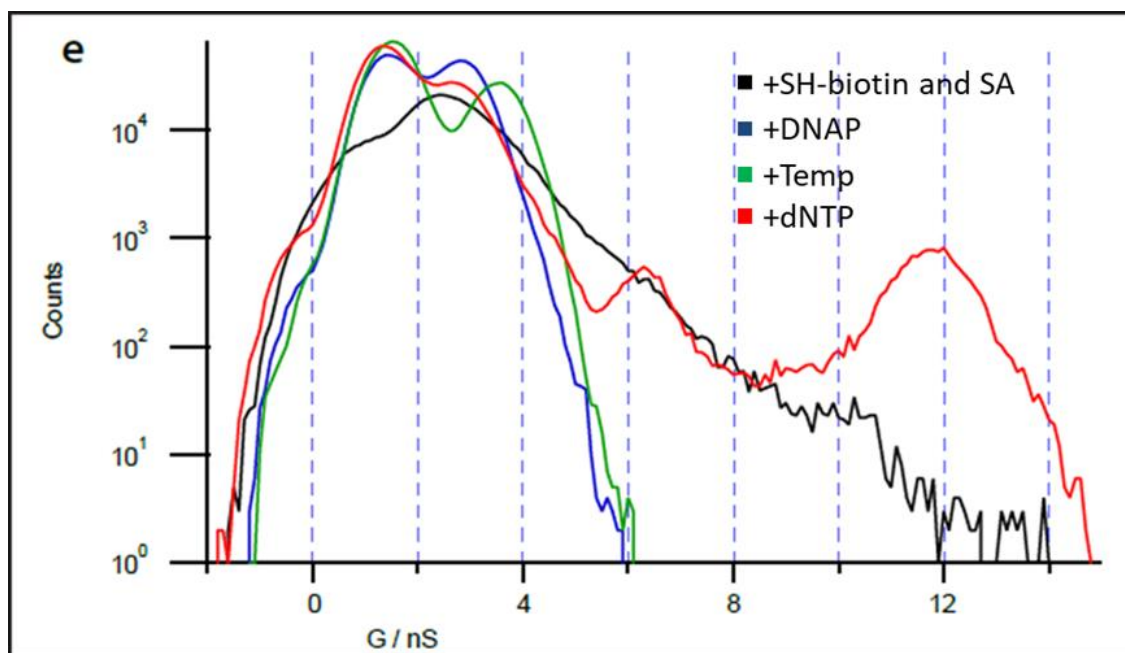
Figure 4.5.3. Conductance Signals from DNAP Experiment Under 50 mV Bias. Expansions to right of (a-d) show signal characteristics over 50 ms intervals. (a) After modifying electrodes with thiolated biotin and streptavidin. (b) After adding biotinylated phi29 DNA polymerase. (c) After adding A10 template DNA. (d) After adding dNTP. (e) Histogram showing conductance distributions for all four stages in their respective colors. Experiment jointly conducted with Weisi Song.

There are some additional features of the data worth note. For the three steps after the introduction of the polymerase, the small fluctuations can be seen in the histogram as well-separated peaks, with the lower conductance peak at around 1.5 nS. Interestingly, the peak separation changes with the step, being about 1.4 nS after the initial introduction of the polymerase, then increasing to 2.0 nS after the introduction of the template DNA before decreasing again to 1.3 nS after the addition of dNTP. The change in small fluctuation level could reflect some change in the configuration of the polymerase when it binds to the template DNA strand, but additional data will need to be collected to see if the variation repeats. The timing of the small fluctuations also seems to change from step to step. After the introduction of DNAP, the ratio between low-

131

conductance population and high-conductance population is almost even at 1.1. After the introduction of template DNA, the ratio between low-conductance population and high-conductance population is 2.4. Interestingly, while the amplitude of small fluctuations after adding dNTP more closely resembles the DNAP-only step, the timing more closely resembles the template step. Here, the low-conductance state is populated 2.2 times as much as the high-conductance state.

4.5.3   Anti-DNP

The second experiment that has been run with this platform investigates the IgE anti-DNP antibody. This is a simpler experiment as it aims merely to establish and measure a protein junction rather than use the junction to probe protein dynamics. The aim of the experiment is to modify the electrodes with a thiolated linker molecule containing 2,4 dinitrophenol (DNP). Anti-DNP, which is a bivalent antibody, can then form a junction between the two electrodes by binding to one DNP on either side of the dielectric gap. In this experiment, first a solution of 1 µM $HSCH_2CH_2$-dinitrophenol in degassed ethanol is introduced into the fluid chamber and left to incubate overnight. The thiol group of the modified DNP bonds with the platinum of the electrodes, resulting in a DNP surface coating for the electrodes. Next, the chamber is rinsed 5x with degassed ethanol to remove excess DNP. Next, the ethanol is replaced with 1 mM phosphate buffer (PB) at pH 7.4. Next, a linear voltage sweep is performed to set the baseline wet conductance of each device. Next, a control sample of 100 nM IgE isotype (nonbinding) in 1 mM PB is introduced, while in real time, the conductance of one of the devices is monitored under a fixed potential of 10 mV. After 30 minutes, another linear voltage sweep is performed on each device, and any device that shows elevated conductance

132

compared to baseline is monitored under fixed potentials ranging from 10 mV to 300

mV. Because the isotype protein cannot make specific bonds to the DNP, no increased

conductance is expected to be observed. Next, the chamber is rinsed 5x with 1 mM PB to

remove the isotype control. Next, a solution of 100 nM anti-DNP Ab in 1 mM PB is

introduced, while in real time, the conductance of one of the devices is monitored under a

fixed potential of 10 mV. After 30 minutes, another linear voltage sweep is performed on

each device, and any device that shows elevated conductance compared to baseline is

monitored under fixed potentials ranging from 10 mV to 300 mV. If an anti-DNP

antibody makes a contact to one DNP molecule on each electrode, an elevated

conductance should be observed.
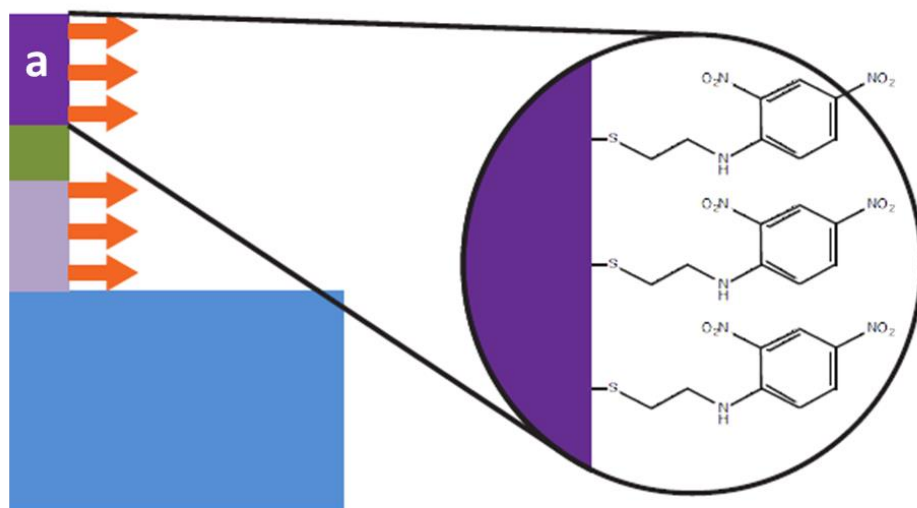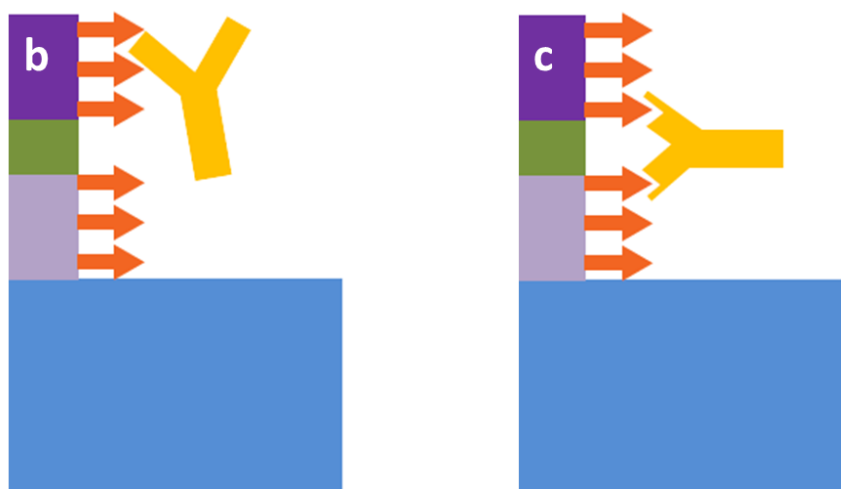
Figure 4.5.4. Anti-DNP Experiment Sequence. (a) Electrodes are modified with thiolated 2,4 dinitrophenol (DNP). Inset shows structure of thio-DNP. (b) A non-binding IgE isotype is added as a control. (c) Anti-DNP IgE is added and bridges the gap.

It is predicted that no increase in conductance should be observed after the addition of the isotype control, due to the fact that it is incapable of forming specific contacts with the electrodes. The addition of anti-DNP should produce a conductance distribution with peaks at roughly 300 pS and 2 nS assuming that it matches the results from the STM experiments. The experiments that have been run on anti-DNP so far have yielded mostly negative results. In one exception, the conductance of a device increased from 0 pS to 35 pS after the addition of the non-binding isotype control. During fixed-bias monitoring at 200 mV immediately after the isotype control was added, conductance spikes up to 300 pS were seen. After 30 minutes of incubation, the current spikes largely subsided. After the addition of anti-DNP, there was an additional minor increase in conductance to 41 pS, but no current spikes were observed.
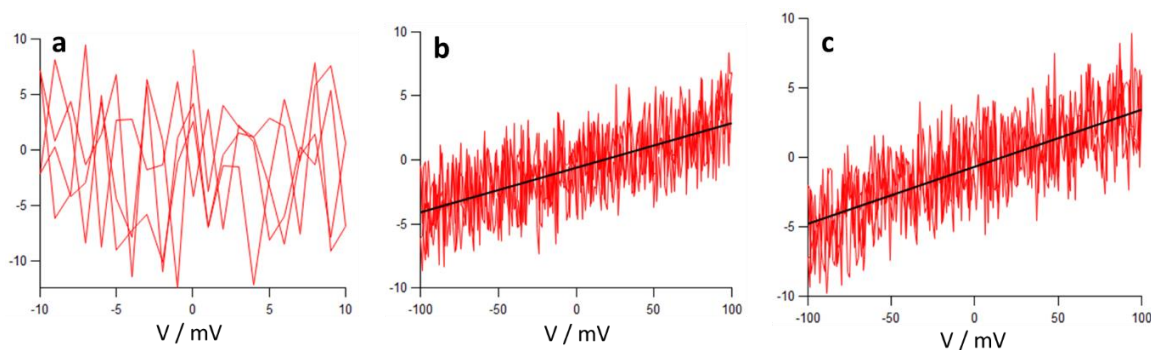
Figure 4.5.5. IV Sweeps from Anti-DNP Experiment. (a) After modification in DNP. (b) After non-binding IgE isotype added. (c) After anti-DNP antibody added. Experiment jointly conducted with Weisi Song.

4.5.4   Electric field-induced denaturation

When interpreting measured conductance data, it is important to consider the possible effects of the applied bias on the structure of the proteins being measured. In particular, there is a possibility that the applied bias will denature the protein. In these experiments, potential differences of about 100 mV are applied over distances of about 10 nm, resulting in an electric field strength on the order of 100 kV/cm. Experiments involving proteins attached to bare metal electrodes have found that denaturation can occur at similar field strength[73]. Denaturation is also observed in experiments involving proteins translocating through solid-state nanopores, where the electric field in the pore is of similar strength, though without the protein being in contact with metal surfaces[74, 75]. On the other hand, experiments where proteins are bound to electrodes with specific contacts strongly suggest that proteins are at least partially folded, since a fully denatured protein would be unable to form a specific bond[70]. The denaturation of proteins at higher biases would be expected to result in a conductance decrease due to the replacement of a specific bond with a non-specific bond. Instead, several proteins exhibit fluctuations to

135

higher-conductance states when the applied bias exceeds a threshold value of approximately 100 mV[70]. In any case, the partial or full denaturation of proteins has not yet been specifically tested with this platform. It may be instructive to perform a series of experiments comparing the conductance properties of proteins under various applied potentials and with or without the addition of chemical denaturants.

4.6   Discussion

There is a lot that can be taken from the results of this project so far, both positive and negative. It is important to take stock of the results and see where practices can be improved for future experiments, in addition to finding ways to leverage the areas of success. For the platform as a whole, the biggest negative has been the low signal yield that has been obtained so far. Because the fabrication is so complicated, there are a number of reasons why this could be, and some of our experimental practices have unfortunately contributed to pinning down sources of failure. As we are building prototype devices, our general practice has been to push forward until we hit an obstacle, then try to figure out how to get around it. The benefit of this approach is that we can move forward more quickly when things are going well and we can react fairly quickly and flexibly when we need to make a change. The drawback is that when we are less systematic in testing parameters it can be harder to narrow down failure modes, and it renders our explanations less robust. This can particularly get us into trouble in situations where we get a great result – such as the initial detection of signals from DNAP – that we fail to replicate. We need to go back through a long chain of potential causes to figure out what went wrong. For the anti-DNP experiment, the failure to get a reliable signal so

far has been particularly frustrating. The system is simpler than the DNAP system, and anti-DNP is large enough that it should be accessible with our current gap spacing. In both cases, it is possible that one factor in the low signal yield compared to the STM experiments is the fixed nature of the gaps. In the STM, the probe has a large area it can search for a contact, whereas with the chips, we are at the mercy of spontaneously formed contacts. The way forward for both experiments will likely involve more careful and systematic controls to make sure our bases are covered. One exciting possibility is that the successful testing of the sputtered Cr adhesion layers will open up the ability to use thinner dielectric films. This should give proteins more opportunity to find available binding sites across the gap. Additionally, the ability to make large electrode junctions without shorting would allow us to increase the size of the electrodes, and therefore the likelihood of forming a contact. To test the effectiveness of our electrode modification, we can make use of data from the STM showing that electrodes are passivated by the modification. In particular, CV scans of modified electrodes show significantly less current than identical scans of unmodified electrodes.

Despite significant frustrations with regard to final results, there have been plenty of successes in this project so far. We have confronted and solved a number of problems and seem to have a solid platform that is just about ready to generate high-quality data. I am very confident in the current material choices – Pt/HfO$_2$ devices are physically and chemically more resilient than Pd/Al$_2$O$_3$, and the change to sputtered Cr has dramatically decreased electrode damage. Our CV cleaning scans show that our electrodes are in contact with solution, and we have protocols in place to evaluate the effectiveness of our electrode modification. Our experiments with DNAP show the most promise so far. We

have captured clear signals from a polymerase, though we do not yet know how to interpret the signal. Of particular interest is the fact that we see two distinct levels of fluctuations in the signal – small fluctuations which appear first, and large fluctuations that appear only when dNTP is introduced into the system. This is a striking confirmation of data from the STM experiments which show the same pattern. Further, the ratio between the size of the large and small fluctuations is very close to the ratio from the STM data. This similarity gives us high confidence in the legitimacy of the signals and gives hope that we are very close to producing data of higher quality and quantity.

4.7   Future Work

The path forward for this project is relatively clear once we are able to consistently get signals from our devices. The advantage of the anti-DNP system is that it is very simple. The junction structure is metal-DNP-Ab-DNP-metal, which is the simplest junction you can make if you want specific binding. This makes the system great for fundamental studies. One type of test that we plan to do is to see the temperature dependence of the conductance. We have access to a cryostat which will allow us to probe temperatures < 50 K. This will help elucidate the conductance mechanism or mechanisms in view. We could also do a verification of the requirements for binding chemistry – somewhat different since both electrodes are modified. Perhaps we can use a Fab fragment of anti-DNP, so there is only one specific attachment possible, though this would require smaller gaps. For the DNAP system, the applications are much more exciting. When we can get consistent signals, we can turn our efforts to analysis in

hopes of decoding the sequence information. Here we will have the advantage of operating two different platforms in parallel, each of which can provide insight into the system. Moving beyond the proteins that we have already studied, the architecture that we have developed can in theory be applied to any protein on the condition that (1) appropriate linking chemistry can be developed, and (2) the minimum gap size is accessible to our fabrication tools. We currently have access to nanofabrication facilities at Oak Ridge National Laboratory, which has a plasma-enhanced ALD system which may allow us to produce even thinner dielectric layers than those that we currently make at ASU. One exciting potential application for this technology is detecting proteins associated with different diseases. The requirement for specific contacts provides an intrinsic ability to avoid false positive signals. Additionally, in an application where single-molecule sensitivity is not required, electrode areas could be scaled up to enhance the signal.

5. CONCLUSIONS

This dissertation has focused on combining top-down and bottom-up fabrication techniques in order to make prototype sensing devices with critical dimensions tailored to particular target biomolecules. In particular, I have worked on a device for DNA sequencing that embeds a pair of closely-spaced electrodes in a sealed microfluidic channel and then uses electrochemical deposition of metal on the electrode tips in order to close the gap distance and create a nanopore constriction. I have also begun work on a device designed to use protein molecules to connect electrode pairs separated by a thin dielectric layer. This is achieved by modifying the electrode surfaces with linker molecules which bind specifically to a target protein.

In Chapter 2, I reviewed existing approaches for sequencing DNA with nanopore devices. While there has been some success, particularly with devices based on protein pores embedded in lipid membranes, I found that there is still considerable work left to be done. I categorized the major challenges that must be successfully met to create an effective nanopore sequencing device: a device must demonstrate specificity of detection, controllability of translocation, and reproducibility and scalability of fabrication.

In Chapter 3, I introduced a new method for fabricating solid-state nanopore devices. While many attempts have been made to integrate control or gating electrodes into a solid state nanopore devices, a consistent barrier has been the high difficulty of aligning the electrodes to the pore with top-down fabrication techniques. The insight of this method is that an electrode pair with a smaller gap can be integrated into a sealed microfluidic channel with height less than 10 nm. The bottom-up technique of

electrochemical deposition can be used to grow the electrodes toward each other, forming a nanopore within the channel. I described the geometric and material decisions that informed the design of the device. I then described the process of electrochemical deposition and characterized the main reaction used to form the nanopore. I introduced a method for using small-amplitude AC signals to detect the electrical impedance between the electrode tips during deposition, and I showed how this information was used as part of a feedback control to stop the deposition when the gap reached a critical distance. I then described the fabrication process for a representative device and showed results from device characterization tests. Next, I examined the results from a variety of experiments showing the ability to use electric potentials to drive charged species, including DNA, through the nanochannel and detect them optically using fluorescent markers. I also showed initial results demonstrating the ability to use the control electrodes as gates in an ionic field-effect transistor to alter the charge-transport properties of the nanochannel. Last, I assessed the remaining barriers that need to be overcome in order to detect DNA translocation events in real time by either ionic current or transverse tunnel current, and I described future projects for the nanopore platform.

In Chapter 4, I introduced a strategy for creating fixed-nanogap sensors with electrodes that can be chemically modified to form electrical junctions with proteins. I briefly reviewed past work exploring the electronic properties of proteins, particularly highlighting recent work indicating that contacts between metal electrodes and proteins play a critical role in determining the mechanism and strength of protein conduction. I explored the design considerations for both individual sensor devices and for constructing sensor arrays on a chip. I described the typical fabrication process for a device and noted

141

steps where testing results prompted changes to the fabrication protocol. I showed results of device characterization experiments that gave insight into the quality of the materials and fabrication processes. I described the experimental process for tests focused on two different proteins, and I showed the results from those tests, highlighting the detection of protein signals from several devices. Last, I evaluated the current state of the project and steps that can be taken to improve the percentage of devices that yield protein signals, and I looked ahead to additional experiments that can be performed once the devices are producing reliable and reproducible data.

Overall, I have sought to show the promise of combining top-down and bottom-up techniques in device design and fabrication. In particular, the use of bottom-up techniques as "finishing steps" has the potential to extend the powerful capabilities of top-down device fabrication to the single-molecule level and open up a new paradigm for the design and creation of biomolecular sensors.

REFERENCES

1. Lu, W. and Lieber, C. "Nanoelectronics from the bottom up." *Nature Materials* 6 (2007): 841-850

2. Cheng, J., Ross, C., et al. "Templated self-assembly of block copolymers: top-down helps bottom-up." *Adv. Mater.* 18 (2006): 2505-2521

3. "Manufacturing at the nanoscale." *Nano.gov.* United States National Nanotechnology Initiative. n.d. Web. Accessed July 18, 2019. < https://www.nano.gov/nanotech-101/what/manufacturing>

4. "Top-down, bottom-up fabrication." *Imgne.com.* Imagine Intelligent Materials. October 28, 2014. Web. Accessed July 18, 2019. < http://imgne.com/2014/10/top-bottom-nanocarbon/>

5. Sanger, F., and Coulson, A. "A rapid method for determining sequences in DNA by primed synthesis with DNA polymerase." *Journal of Molecular Biology* 94: (1975) 441-448

6. Bentley, D., Balasubramanian, S., et al. "Accurate Whole Human Genome Sequencing using Reversible Terminator Chemistry." *Nature* 456 (2008): 53-59

7. Kasianowicz, J., Brandin, E., et al. "Characterization of individual polynucleotide molecules using a membrane channel." *Proc. Natl. Acad. Sci. USA* 93 (1996): 13770-13773

8. Meller, A., Nivon, L., et al. "Rapid nanopore discrimination between single polynucleotide molecules." *Proc. Natl. Acad. Sci. USA* 97 (2000): 1079-1084

9. Meller, A., Nivon, L., et al. "Voltage-Driven DNA Translocations through a Nanopore." *Physical Review Letters* 86 (2001): 3435-3438

10. Akeson, M., Branton, D., et al. "Microsecond time-scale discrimination among polycytidylic acid, polyadenylic acid, and polyuridylic acid as homopolymers or as segments within single RNA molecules." *Biophysical Journal* 77 (1999): 3227-3233

11. Vercoutere, W., Winters-Hilt, S., et al. "Rapid discrimination among individual DNA hairpin molecules at single-nucleotide resolution using an ion channel." *Nature Biotechnology* 19 (2001): 248-252

12. Hornblower, B., Coombs, A., et al. "Single-molecule analysis of DNA-protein complexes using nanopores." *Nature Methods* 4 (2007): 315-317

13. Lieberman, K., Cherf, G., et al. "Processive replication of single DNA molecules in a nanopore catalyzed by phi29 DNA polymerase." *J. Am. Chem. Soc.* 132 (2010): 17961-17972

14. Cherf, G., Lieberman, K., et al. "Automated forward and reverse ratcheting of DNA in a nanopore at 5-Å precision." *Nature Biotechnology* 30 (2012): 344-348

15. Butler, T., Pavlenok, M., et al. "Single-molecule DNA detection with an engineered MspA protein nanopore." *Proc. Natl. Acad. Sci. USA* 105 (2008): 20647-20652

16. Derrington, I., Butler, T., et al. "Nanopore DNA sequencing with MspA." *Proc. Natl. Acad. Sci. USA* 107 (2010): 16060-16065

17. Manrao, E., Derrington, I., et al. "Reading DNA at single-nucleotide resolution with a mutant MspA nanopore and phi29 DNA polymerase." *Nature Biotechnology* 30 (2012): 349-354

18. Song, L., Hobaugh, M., et al. "Structure of staphylococcal α-Hemolysin, a heptameric transmembrane pore." *Science* 274 (1996): 1859-1866

19. Howorka, S., Cheley, S., et al. "Sequence-specific detection of individual DNA strands using engineered nanopores." *Nature Biotechnology* 19 (2001): 636-639

20. Astier, Y., Braha, O., et al. "Toward single molecule DNA sequencing: direct identification of ribonucleoside and deoxyribonucleoside 5'-monophosphates by using an engineered protein nanopore equipped with a molecular adapter." *J. Am. Chem. Soc.* 128 (2006): 1705-1710

21. Wu, H., Astier, Y., et al. "Protein nanopores with covalently attached molecular adapters." *J. Am. Chem. Soc.* 129 (2007): 16142-16148

22. Clarke, J., Wu, H., et al. "Continuous base identification for single-molecule nanopore DNA sequencing." *Nature Nanotechnology* 4 (2009): 265-270

23. Stoddart, D., Heron, A., et al. "Single-nucleotide discrimination in immobilized DNA oligonucleotides with a biological nanopore." *Proc. Natl. Acad. Sci. USA* 106 (2009): 7702-7707

24. Mikheyev, A. and Tin, M. "A first look at the Oxford Nanopore MinION sequencer." *Molec. Ecol. Resources* 14 (2014): 1097-1102

25. Jain, M., Fiddes, I., et al. "Improved data analysis for the MinION nanopore sequencer." *Nature Methods* 12 (2015): 351-359

26. Ip, C., Loose, M., et al. "MinION Analysis and Reference Consortium: Phase 1 data release and analysis." *F1000Research 4* (2015): 1075

27. Li, J., Stein D., et al. "Ion-beam sculpting at nanometer length scales." *Nature* 412 (2001): 166-169

28. Li, J., Gershow, M., et al. "DNA molecules and configurations in a solid-state nanopore microscope." *Nature Materials* 2 (2003): 611-615

29. Storm, A., Chen, J., et al. "Fabrication of solid-state nanopores with single-nanometre precision." *Nature Materials* 2 (2003): 537-540

30. Storm, A., Storm, C., et al. "Fast DNA translocation through a solid-state nanopore." *Nano Letters* 5 (2005): 1193-1197

31. Zandbergen, H., van Duuren, R., et al. "Sculpting nanoelectrodes with a transmission electron beam for electrical and geometrical characterization of nanoparticles." *Nano Letters* 5 (2005): 549-553

32. Smeets, R., Keyser, U., et al. "Salt dependence of ion transport and DNA translocation through solid-state nanopores." *Nano Letters* 6 (2006): 89-95

33. Keyser, U., Koeleman, B., et al. "Direct force measurements on DNA in a solid-state nanopore." *Nature Physics* 2 (2006): 473-477

34. Stein, D., Deurvorst, Z., et al. "Electrokinetic concentration of DNA polymers in nanofluidic channels." *Nano Letters* 10 (2010): 765-772

35. Kowalczyk, S., Hall, A., et al. "Detection of local protein structures along DNA using solid-state nanopores." *Nano Letters* 10 (2010): 324-328

36. Kowalczyk, S., Wells, D., et al. "Slowing down DNA Translocation through a Nanopore in Lithium Chloride." *Nano Letters* 12 (2012): 1038-1044

37. Kim, M., Wanunu, M., et al. "Rapid fabrication of uniformly sized nanopores and nanopore arrays for parallel DNA analysis." *Advanced Materials* 18 (2006): 3149-3153

38. Wanunu, M., Sutin, J., et al. "DNA translocation governed by interactions with solid-state nanopores." *Biophysical Journal* 95 (2008): 4716-4725

39. Wanunu, M., Morrison, W., et al. "Electrostatic focusing of unlabelled DNA into nanoscale pores using a salt gradient." *Nature Nanotechnology* 5 (2010): 160-165

40. McNally, B., Singer, A., et al. "Optical Recognition of Converted DNA Nucleotides for Single-Molecule DNA Sequencing Using Nanopore Arrays." *Nano Letters* 10 (2010): 2237-2244

41. van den Hout, M., Hall A., et al. "Controlling nanopore size, shape and stability." *Nanotechnology* 21 (2010): 115304

42. Hall, A., Scott, A., et al. "Hybrid pore formation by directed insertion of α-haemolysin into solid-state nanopores." *Nature Nanotechnology* 5 (2010): 874-877

43. Yang, J., Ferranti, D., et al. "Rapid and precise scanning helium ion microscope milling of solid-state nanopores for biomolecule detection." *Nanotechnology* 22 (2011) 285310

44. Lo, C., Aref, T., et al. "Fabrication of symmetric sub-5 nm nanopores using focused ion and electron beams." *Nanotechnology* 17 (2006): 3264-3267

45. Gierak, J., Madouri, A., et al. "Sub-5 nm FIB direct patterning of nanodevices." *Microelectronic Engineering* 84 (2007): 779-783

46. Marshall, M., Yang, J., et al. "Direct and transmission milling of suspended silicon nitride membranes with a focused helium ion beam." *Scanning* 34 (2012): 101-106

47. Hall, A. "In situ thickness assessment during ion milling of a free-standing membrane using transmission helium ion microscopy." *Microscopy and Microanalysis* 19 (2013): 740-744

48. Polonsky, S., Rossnagel, S., et al. "Nanopore in metal-dielectric sandwich for DNA position control." *Appl. Phys. Lett.* 91 (2007): 153103

49. Luan, B., Peng, H., et al. "Base-by-base ratcheting of single stranded DNA through a solid-state nanopore." *Phys. Rev. Lett.* 104 (2010): 238103

50. Harrer, S., Ahmed, S., et al. "Electrochemical characterization of thin film electrodes toward developing a DNA transistor." *Langmuir* 26 (2010): 19191-19198

51. Harrer, S., Waggoner, P., et al. "Electrochemical protection of thin film electrodes in solid state nanopores." *Nanotechnology* 22 (2011): 275304

52. Fischbein, M., and Drndic, M. "Sub-10 nm Device Fabrication in a Transmission Electron Microscope." *Nano Letters.* 7 (2007): 1329-1337

53. Healy, K., Ray, V., et al. "Fabrication and characterization of nanopores with insulated transverse nanoelectrodes for DNA sensing in salt solution." *Electrophoresis.* 33 (2012): 3488-3496

54. Ivanov, A., Instuli, E., et al. "DNA Tunneling Detector Embedded in a Nanopore." *Nano Letters* 11 (2011): 279-285

55. He, J., Lin, L., et al. "Identification of DNA basepairing via tunnel-current decay." *Nano Letters* 7 (2007): 3854-3858

56. Chang, S., He, J., et al. "Tunnelling readout of hydrogen-bonding-based recognition." *Nature Nanotechnology* 4 (2009): 297-301

57. Chang, S., Huang, S., et al. "Electronic signatures of all four DNA nucleosides in a tunneling gap." *Nano Letters* 10 (2010): 1070-1075

58. Krishnakumar, P., Gyarfas, B., et al. "Slowing DNA translocation through a nanopore using a functionalized electrode." *ACS Nano* 7 (2013): 10319-10326

59. Sadar, J., Wang, Y., and Qing, Q. "Confined electrochemical deposition in sub-15 nm space for preparing nanogap electrodes." *ECS Transactions* 77 (2017): 65-72

60. Xiao, X., Xu, B., and Tao, N. 2004 "Conductance titration of single peptide molecules." *J. Am. Chem. Soc.* 126 (2004): 5370–5371

61. Artes, J., et al. "Conductance switching in single wired redox proteins." *Small* 10 (2014): 2537–2541

62. Bostick, C., Mukhopadhyay, S., et al. "Protein bioelectronics: a review of what we do and do not know." *Rep Prog Phys* 81 (2018): 026601

63. Amdursky, N., Marchak, D., et al. "Electronic transport via proteins." *Advanced Materials* 26 (2014): 7142-7161

64. Artés, J., Díez-Pérez, I., and Gorostiza, P. "Transistor-like behavior of single metalloprotein junctions." *Nano Letters* 12 (2012): 2679–2684

65. Yoo, S., Lee, T., et al. "Fabrication of biofilm in nanoscale consisting of cytochrome f/2-MAA bilayer on Au surface for bioelectronic devices by self-assembly technique." *J Nanosci Nanotechnol* 11 (2011): 7069–7072

66. Korpany, K., et al. "Conductance switching in the photoswitchable protein Dronpa." *J Am Chem Soc* 134 (2012): 16119–16122

67. Sepunaru, L., Pecht I., et al. "Solid-state electron transport across azurin: From a temperature-independent to a temperature-activated mechanism." *J Am Chem Soc* 133 (2011): 2421–2423

68. Adhikari, R., Malvankar, N., et al. "Conductivity of individual Geobacter pili." *RSC Adv* 6 (2016): 8354–8357

69. Malvankar, N., et al. "Tunable metallic-like conductivity in microbial nanowire networks." *Nat Nanotechnol* 6 (2011): 573–579

70. Zhang, B., Song, W., et al. "Observation of giant conductance fluctuations in a protein." *Nano Futures* 1 (2017): 035002

71. Zhang, B., Song, W., et al. "Role of contacts in long-range protein conductance." *PNAS* 116 (2019): 5886-5891

72. Vattay, G., Kauffman, S., et al. "Quantum biology on the edge of quantum chaos." *PLoS One* 9 (2014): e89017

73. Palecek, E., et al. "Electrochemistry of nonconjugated proteins and glycoproteins. Toward sensors for biomedicine and glycomics." *Chem. Rev.* 115 (2015): 2045–108

74. Talago, D., and Li, J. "Single-molecule protein unfolding in solid state nanopores." *J Am Chem Soc* 131 (2009): 9287-9297

75. Freedman, K., Jurgens, M., et al. "Chemical, thermal, and electric field induced unfolding of single protein molecules studied using nanopores." *Analytical Chemistry* 83 (2011): 5137-5144

76. Nitzan, A. *Chemical Dynamics in Condensed Phases.* Oxford: Oxford University Press, 2006.

77. Onuchic, J., et al. "Pathway analysis of protein electron-transfer reactions." *Annu. Rev. Biophys. Biomol. Struct.* 21 (1992): 349–377

78. Polizzi, N., Skourtis, S., and Beratan, D. "Physical constraints on charge transport through bacterial nanowires." *Faraday Discuss.* 153 (2012): 43–62

79. Beratan, D., et al. "Charge transfer in dynamical biosystems, or the treachery of (static) images." *Acc. Chem. Res.* 48 (2015): 474–481

80. Ai, Y., Liu, J., et al. "Field effect regulation of DNA translocation through a nanopore." *Anal. Chem.* 82 (2010): 8217-8225

81. Schoch, R. "Transport phenomena in nanofluidics." *Rev. Mod. Phys.* 80 (2008): 839-883

82. Tsutsui, M., Taniguchi, M., et al. "Transverse field effects on DNA-sized particle dynamics." *Nano Lett.* 9 (2009): 1659–1662

83. Krems, M., Pershin, Y., et al. "Ionic memcapacitive effects in nanopores." *Nano Lett.* 10 (2010): 2674–2678

84. Feng, J., Liu, J., et al. "Impedance characteristics of amine modified single glass nanopores." *Anal. Chem.* 82 (2010): 4520–4528

85. Karnik, R., Fan, R., et al. "Electrostatic control of ions and molecules in nanofluidic transistors." *Nano Lett.* 5 (2005): 943–948

86. Kalman, E., Sudre, O., et al. "Control of ionic transport through gated single conical nanopores." *Anal. Bioanal. Chem.* 394 (2009): 413–419

87. Nam, S., Rooks, M., et al. "Ionic field effect transistors with sub-10 nm multiple nanopores." *Nano Lett.* 9 (2009): 2044–2048

88. Taniguchi, M., Tsutsui, M., et al. "Fabrication of the gating nanopore device." *Appl. Phys. Lett.* 95 (2009): 123701

89. Joshi, P., Smolyanitsky, A., et al. "Field effect modulation of ionic conductance of cylindrical silicon-on-insulator nanopore array." *J. Appl. Phys.* 107 (2010): 054701

APPENDIX A

CO-AUTHORS AGREEMENT ON USING PUBLISHED WORK

Part of Chapter 3 in this dissertation was published as "Confined Electrochemical Deposition in Sub-15 nm Space for Preparing Nanogap Electrodes" in ECS Transactions (Sadar et al., 2017). All co-authors have granted their permission to use the published article in this dissertation.